UNIVERSITY OF CALIFORNIA

Santa Barbara

Tuning the surface hydrophobicity of SBA-15 type materials for controlled molecular adsorption, hydration dynamics, and heterogeneous catalysis

A dissertation submitted in partial satisfaction of the

requirements for the degree Doctor of Philosophy

in Chemical Engineering

by

Hyunjin Moon

Committee in charge:

Professor Susannah L. Scott, Chair

Professor Songi Han

Professor Mahdi M. Abu-Omar

Professor Baron G. Peters

September 2021

The dissertation of Hyunjin Moon is approved.

Songi Han

Mahdi M. Abu-Omar

Baron G. Peters

Susannah L. Scott, Committee Chair

August 2021

Tuning the surface hydrophobicity of SBA-15 type materials for controlled molecular adsorption, hydration dynamics, and heterogeneous catalysis

by

Hyunjin Moon

ACKNOWLEDGEMENTS

The past five years spent doing my PhD have been essential in my growth as a student and a researcher, and gifted me various experiences. First of all, I would like to thank the Chemical Engineering department professors at UCSB. Thank you for giving me the opportunity to do research in a supportive, engaging, and motivating environment.

I cannot thank my advisor, Professor Susannah L. Scott, enough for her support. In the course of doing my research with you, I was able to learn the importance of having a more rigorous process in analyzing scientific results. Thanks to you I was able to get the opportunity to learn the attitude that a scholar should have. I conducted interesting research with Professor Songi Han. Thank you for helping me in expending my research scope and giving me valuable advice. Also, thank Professor Scott and Professor Han for giving me the opportunity to experience a new research environment and culture while being in Germany. I would like to extend my appreciation to my committee members, Professor Baron Peters and Professor Mahdi Abu-Omar, for giving me critical feedback over the years. I received a lot of help from the group members in conducting the experiments while doing research at Scott group. I would especially like to thank Ali Chamas, Tarnuma Tabassum, and Jason Chalmers. I would also like to express my gratitude to Salman Khan and Eunjae Shim for having discussions about my research any time during my Ph.D. course, whether we were having dinner or just resting. I also thank Yannik Louven, Sonja Mürtz and Professor Palkovits' group members during my time doing research in Germany. Also thank you to Ryan Collaton, Jacob Monroe, Thomas Casey, and Ryan Barnes for helping me in conducting the water dynamics research. I would

also like to acknowledge the scientists at MRL and CNSI. Without the assistance from people who I met the last 5 years, this work would not have been possible.

My master's degree research experience helped me a lot in adjusting to the doctoral program. I would like to thank my master's degree advisor, Professor Seung Hwan Ko who supported my research ideas and helped me prepared for my doctoral studies abroad, and Dr. Habeom Lee, Dr. Sukjoon Hong, Dr. Young D. Suh, Dr. Jinhwan Lee, Dr. Jinhyeong Kwon, and Dr. Junyeob Yeo, who gave me the opportunity to learn the attitude that a researcher should have and how to conduct research while doing research together. Also, I would like to acknowledge to my seniors and junior in the master's lab who encouraged me while I was in the USA.

None of this would have been possible without the support I received from my friends and family. I would like to thank friends in UCSB Korean community and old friends, Dr. Taehyung Kim, Dr. Keunhwan Pack, and Dr. Inchang Choi, who are studying and working in U.S and consistently supporting each other. Also, I would like to thank my girlfriend, Youngshin who I share enjoyable times and makes me smile. Lastly, I thank my loving family in Busan, South Korea and Boston for their unwavering support.

VITA OF Hyunjin Moon
September 2021

Education

University of California, Santa Barbara (UCSB): 2016-present

Ph.D. Chemical Engineering

Seoul National University: 2014-2016

M.S. Mechanical Engineering

Korea Advanced Institute of Science and Technology (KAIST): 2005-2013

B.S., Mechanical Engineering, *Magna Cum Laude*

Research Experience

Graduate student researcher | Dr. Susannah L. Scott Group, UCSB

(September 2016 – August 2021)

- Designed mesoporous catalysts with gradually changing surface polarity. Investigated physical properties of catalyst surfaces and solvent effects to enhance the rate and selectivity of hydrogenation reactions. Interpreted heterogeneous reaction kinetics. based on microkinetic models and reaction engineering.
- Worked with a cross-displinary team, including DNP-NMR and simulation research groups to unravel surface water dynamics on silica/organosilica materials, and to correlate water properties with heterogeneous catalysis.
- Conducted research on lifetimes and degradation rates of plastics in various environments, and worked closely with experts in Environmental Science and Chemistry.

Visiting researcher at RWTH Aachen University, Germany (June – August 2019)

- Investigated surface polarity effect on reactivity in hydrogenation of aromatic molecules and reductive amination of levulinic acid. Tested the use of high-pressure NMR for heterogeneous catalysis.

General researcher at Seoul National University **(**March – July 2016)

- Developed a nanomaterial-based microfluidic reactor for quantum dot synthesis to enable low-temperature synthesis.
- Trained new graduate researchers on nanomaterial synthesis and flexible device characterization.

Graduate researcher at KAIST & Seoul National University
(March 2013 – February 2016)

- Developed a polymer/metal nanowire-based supercapacitor to improve energy storage of wearable devices. Investigated the interrelationship among the reaction parameters of Ag nanowire synthesis to reduce haze in transparent and conducting films.
- Contributed to the publications of 12 co-authored papers and filing of 2 patents regarding nanomaterial-based flexible electronics.

Awards and Fellowships

- UC-RWTH IRES Fellowship, June – August 2019
- Mellichamp Sustainability Fellowship, June – September 2018
- UCSB Crossroads Fellowship in Green Chemistry, September 2017 – June 2018
- Global Ph.D. Fellowship from National Research Foundation of Korea, March 2014 – February 2016
- Korean National Natural Science and Engineering Scholarship, March 2005 – February 2013 (4 years)

Presentations

- **H. Moon**, S. Murtz, S. Han, S. L. Scott, Virtual *American Institute of Chemical Engineers (AIChe)*, November 2020
- **H. Moon**, S. Han, S. L. Scott, *American Institute of Chemical Engineers (AIChe)*, Orlando, Florida, November 2019
- **H. Moon**, S. D. Mürtz, S. Han, S. L. Scott, *EuropaCat*, Aachen, Germany, August 2019
- **H. Moon**, S. Han, S. L. Scott, *American Institute of Chemical Engineers (AIChe)*, Pittsburgh, Pennsylvania, October 2018

Publications

- **H. Moon**, S. Han,* S. L. Scott.* "Tuning molecular adsorption in SBA-15-type periodic mesoporous organosilicas by systematic variation of their surface polarity", *Chemical Science,* 2020, 11, 3702-3712
- A. Chamas, **H. Moon**, J. Zheng, Y. Qiu, T. Tabassum, J. H. Jang, M. Abu-Omar, S. L. Scott,* S. Suh.* "Assessing degradation rates of plastics in the environment", *ACS Sustainable Chemistry & Engineering,* 2020, 8, 9, 3494-3511
- **H. Moon**, H. Lee, J. Kwon, Y. D. Suh, D. K. Kim, I. Ha, J. Yeo,* S. Hong,* and S. H. Ko.* "Ag/Au/polypyrrole core-shell nanowire network for transparent, stretchable and flexible supercapacitor in wearable energy devices", *Scientific Reports*, 2017, 7, 41981
- **H. Moon**, P. Won, J. Lee,* and S. H. Ko.* "Low-haze, annealing-free, very long Ag nanowire synthesis and its application in a flexible transparent touch panel", *Nanotechnology*, 2016, 27, 295201

Publications (In Preparation)

- **H. Moon**, C. Ryan, J. I. Monroe, T. M. Casey, M. S. Shell, S. Han*, S. L. Scott,* "Controlled hydrophobic hydration on mesoporous organosilica surfaces"
- **H. Moon**, J. Chalmers, A. Chamas, S. L. Scott,* "*Operando* observation of the molecular adsorption effect on the activity and selectivity in phenol hydrogenation over hydrophilic and hydrophobic Pd catalysts"

ABSTRACT

Tuning the surface polarity of SBA-15 type materials for controlled molecular adsorption, hydration dynamics, and heterogeneous catalysis

by

Hyunjin Moon

Surface polarity may impact the rate and selectivity of heterogeneous catalytic reactions because of the different affinities of the surface for reactants, products, and spectator molecules (e.g., solvent), and may affect the stability of the catalyst under operating conditions. Surface polarity must be varied systematically in order to construct structure-activity correlations. In addition, the lack of methods to assess surface polarity and solid-liquid interfaces makes it difficult to construct such a correlation in heterogeneous catalysis.

To explore the effect of surface polarity, a series of ordered mesoporous organosilica materials with similar surface textural properties but a wide range of surface polarities was prepared via the incorporation of oxo, phenylene, and biphenylene bridging groups in various ratios. The SBA-15-type materials were synthesized through co-condensation and were characterized using TGA, powder XRD, and ^{13}C CP/MAS NMR. The surface polarity was probed by measuring the fluorescence of a solvatochromic dye, Prodan, adsorbed onto the organosilica surfaces from water. By comparing the emission maxima of the fluorescence from the dry materials to that of the dye dissolved in various solvents, the surface polarities were observed to range from values similar to methanol for the pure silica material, to DMSO

for biphenylene-bridged organosilicas. Surface functionalization with TEMPO allowed us to probe surface polarity using electron paramagnetic resonance (EPR) spectroscopy, since the line broadening of the EPR signal increases with decreasing surface polarity.

In order to study the role of silica surface chemistry and polarity on the properties of near-surface water, the translational dynamics of surface water were investigated using Overhauser dynamic nuclear polarization. In pure silicas, condensation of polar silanols to give moderately nonpolar siloxane groups leads to an increase in translational water diffusivity due to the weak interactions between the surface and water. In contrast, increasingly nonpolar surfaces achieved by incorporating organic groups, such as phenylene, biphenylene and ethylene bridges, lead to a gradual decrease in surface water diffusivity. The opposite trend for water diffusivity observed for the nonpolar, organic surfaces is likely due to the formation of a strong hydrogen-bonding network at the organic-water interface.

Hydrophilic catalysts with surface silanol groups and hydrophobic catalysts with biphenylene linkers were synthesized by incorporating Pd into the ordered mesoporous silicas. Phenol hydrogenation was studied using *operando* NMR spectroscopy. In addition to the signals for solution-phase molecules, additional peaks representing each of the key molecules (phenol, cyclohexanone, and cyclohexanol) interacting with the catalyst surface were observed. The latter peaks shifted during the reaction due to the changing composition of the adsorbed layer the surface. Quantitative analysis of the NMR arrays and measurements of adsorption suggest that an increased local phenol concentration on the surface leads to an increase in Pd active site-phenol interactions, accelerating the rate of phenol hydrogenation while suppressing the rate of cyclohexanone hydrogenation despite increased cyclohexanone adsorption onto the support.

The effect of solvent polarity on phenol adsorption and hydrogenation was also investigated as a function of surface type. Solvents that do not solvate phenol well and therefore allow appreciable phenol adsorption, such as cyclohexane and water, lead to significantly faster phenol conversion compared to organic solvents that solvate phenol well, such as acetonitrile, THF, and *p*-dioxane. The use of hydrophobic catalysts in cyclohexane and water further improved the rate of phenol conversion (by a factor of ca. 2) and selectivity to cyclohexanone (by ca. 20 %), due to the increased interaction between phenol and the surface compared with the hydrophilic catalyst.

Overall, this research demonstrates how different methods can be used to assess surface properties such as polarity and hydration dynamics at the molecular level, and shows that tuning surface polarity is an effective strategy to modulate molecular adsorption and activity/selectivity in heterogeneous catalysis.

TABLE OF CONTENTS

Chapter 1. Introduction

1.1 Background

The manufacturing of chemical building blocks from renewable feedstocks, including lignocellulosic biomass, as well as from discarded synthetic polymers, is an important long-term goal in building a sustainable domestic chemical industry. Co-production of higher value chemicals can also help to make the manufacturing of renewable fuels more economical. For example, the hydrogenolysis/hydrogenation of biomass-derived alcohols represents an important route to supplying drop-in replacements for petroleum- and natural gas-derived olefins. The efficient and selective conversion of non-volatile molecules to value-added chemicals is an important challenge for distributed manufacturing. Conducting reactions in semi-aqueous solvent systems and under mild reaction conditions (relatively low temperatures) requires highly active and hydrothermally stable catalysts. These properties can be enhanced by selecting an appropriate solvent type and tuning the catalyst support to modulate the partitioning of dissolved molecules between the bulk solution phase and the catalytically active solid-liquid interface.

1.2 Objectives

This thesis investigated the interdependent support-solvent-solute interactions that control activity and selectivity in reactions of biomass-relevant alcohols. The coupled roles of solvent and catalyst in these liquid-phase reactions were explored in order to enable the design of more effective heterogeneous catalysts. The study contributes to the molecularly-precise

characterization of catalyst supports and active sites, the dynamics of adsorbed reactants and products, as well as solvent dynamics and partitioning to the surface relative to the bulk. Surface structure-property-function relationships are established to understand and direct the selectivity of heterogeneous catalysts. Changing the surface hydrophilicity may allow us to control the rates and selectivities of heterogeneous catalytic reactions by varying the affinity of the surface for reactants, products, and spectator molecules (e.g., solvent). It may also affect the stability of the catalyst under its operating conditions. Thus, this thesis aimed to answer the following key questions: (1) Can catalytic activity and selectivity be controlled systematically by varying the solvation barrier that modulates solute approach to the catalyst surface and its adsorption? (2) Can the solvation barrier for solute approach and adsorption be modulated systematically by tuning the hydrophobicity of the catalyst surface and the solvent types?

1.3 Organization of dissertation

The remainder of Chapter 1 describes some of the key techniques and analysis used in the rest of the dissertation. Chapter 2 describes how mesoporous materials with gradually varying surface polarity were synthesized using silica precursors and how the difference in surface polarity of mesoporous materials was assessed using a solvatochromic dye, Prodan, and electron paramagnetic resonance (EPR) spectroscopy. After that, the effect of surface polarity and solvent types on the extent of molecular adsorption was described. Chapter 3 focuses on the effect of surface polarity and chemistry on water dynamics, and thermodynamic properties of interfacial hydration. Chapter 4 describes the effect of molecular adsorption on activity and selectivity in phenol hydrogenation reaction, mainly relying on *operando* NMR

experiments. Chapter 5 discusses the effect of solvent types on molecular adsorption and activity. Furthermore, the effect of the interplay between surface and solvent types on activity and selectivity in phenol hydrogenation is discussed. Chapter 6 summarizes the key findings in this thesis and suggests future research to further advance heterogeneous catalysis in the biomass conversion area.

1.4 Experimental methods

1.4.1 Synthesis and properties of Periodic Mesoporous Organosilicas (PMO) with varying surface polarity

In synthetic catalysts, surface hydrophilicity has generally not been varied over a wide range, and it is usually convoluted with changes in macro/microstructure that make it difficult to relate changes in reaction efficiency to the changes in surface hydrophilicity. In order to obtain quantitative information about solid/liquid interfaces, the surface hydrophilicity of catalytic materials must be varied systematically while without altering the basic textural properties.

Thus, in this study, SBA-15 type materials with systematically controlled hydrophilicity were synthesized through co-condensation with organosilica sources. Research regarding synthesis of organosilica was actively conducted in the late 1990s and 2000s. The purpose of that research was to modify surface properties and to form mesostructured materials with diverse functional groups.[1–3] According to the results, most of the mesoporous materials were synthesized using surfactants with short chain lengths, such as cetrimonium bromide and Brij-76, thus yielding materials with small pore diameters less than 4 nm. In many cases, the resulting mesoporous organosilicas showed non-ordered structures.[4,5] These

materials are susceptible to fouling and show lower structural stability. Investigations of adsorption efficiency based on surface properties without fouling effects requires the synthesis of SBA-15 materials with ordered mesostructures, similar macrostructures, large pore diameters and surface areas.

Thus, a series of ordered mesoporous organosilica materials with similar surface textural properties but a wide range of surface polarities was prepared via the incorporation of oxo, phenylene, and biphenylene bridging groups. The surface polarity was further controlled by co-condensation, a method in which two different silica precursors are injected in a pre-determined ratio to modulate the surface density of aromatic groups. Among various organosilicas, 1,4-bis(triethoxysilyl)benzene and 4,4'-bis(triethoxysilyl)-1,1'-biphenyl were used, since PMOs synthesized with aromatic surface functional groups have high thermal stability (up to ca. 500 °C in air), which is a desirable property in heterogeneous catalysis.

1.4.2 Surface polarity measurements

The fluorescence of organic dyes is sensitive to the polarity of the environment. Fluorescent probes have been used to study biologically relevant systems, such as membranes and proteins. Prodan dye undergoes intramolecular charge transfer upon photoexcitation (Fig. 1.1a). The electronic energy level is affected by the dipole-dipole and H-bonding interactions in its surroundings.[6] Thus, increasing solvent polarity leads to a red shift in the fluorescence emission, Fig. 1.2b. For example, Prodan fluoresces at wavelengths of 527, 484 and 447 nm when it is dissolved in water, 1-butanol and acetone, respectively.[6] In this study, Prodan was adsorbed on the surface of SBA-15 materials from aqueous solution. Prodan-modified materials were obtained after removing the solution phase, and fluorescence spectra were

collected using an excitation wavelength of 360 nm. The obtained λ_{max} values were used as an indicator of surface polarity, by comparing the values with those obtained in typical solvents.

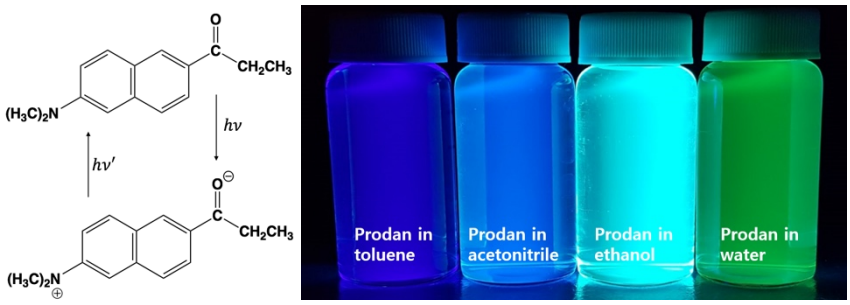

Fig. 1.1. (a) The ground and excited states of Prodan dye. (b) Photograph showing the fluorescence of Prodan dissolved in various solvents.

1.4.3 Overhauser Dynamic Nuclear Polarization (ODNP) relaxometry

The diffusivity of near-surface water depends on the surface polarity. For example, lower water diffusivity is expected for polar silica with a higher silanol density, owing to the formation of more hydrogen bonds between water and surface hydroxyl groups, relative to less polar silica whose surface is dominated by siloxanes. In addition, the surface water diffusivity can provide insight into the molecular behavior of water in mesopores.

Measurements of surface water diffusivity were conducted using Overhauser dynamic nuclear polarization (ODNP).[7] In contrast to other methods for measuring diffusivity, such as T_1 relaxation measurements, pulsed-field gradient NMR, and quasi-elastic neutron scattering, the ODNP method is surface-sensitive, because it excludes the contributions of bulk translational motion by water molecules. Surface sensitivity is achieved by measuring translational diffusivity within ~1 nm of a tethered spin label, such as a nitroxide radical.[8] To

incorporate the spin label onto the surface of a mesoporous silica, the silanol groups were first functionalized by reaction with aminopropyltriethoxysilane. The resulting grafted propylamine groups were then modified by reaction with 4-carboxy-TEMPO. When a sample containing TEMPO is irradiated with microwaves at a specific frequency (the electron Larmor frequency), polarization is transferred from the unpaired electron spin to the nuclear spins of nearby water molecules through the dipolar interaction, thus increasing the intensity of the proton NMR signal from those water molecules. The magnitude of enhancement is a known function of the mobility of this nearby water, thus allowing one to obtain local water diffusivity by measuring NMR signals under microwave irradiation.

An important parameter is the cross-relaxivity, k_σ, which reflects the rate of water ^{1}H nuclear spin flips driven by dipolar couplings to electron spins that lead to hyperpolarization. The physical processes that affect the value of k_σ occur on time scales of tens of picoseconds. This time scale includes relatively rapid diffusion of water molecules near the spin probes. The lifetime of the interaction between the electron spin and water is the correlation time, τ_{corr}. To assess the retardation of hydration dynamics from τ_{corr}, the ratio to the known value corresponding to unhindered diffusion of water near an untethered spin probe in bulk water solution is measured (eq. 1.1)

$$\tau_{corr} \text{ retardation} = \tau_{corr,local} / \tau_{corr,bulk} \quad (1.1)$$

Typically, τ_{corr} is converted to D_{local} using a simple model that assumes the act of tethering a spin probe does not alter the distance or dimensionality of closest approach of a diffusing water molecule, relative to an untethered spin probe diffusing in bulk solution. With

this assumption, the inverse of τ_{corr} retardation can be used to find D_{local} by simply scaling the sum of the diffusivities of water (D_{water}) and spin probe (D_{SL}) diffusing together in the bulk solution:

$$D_{local} = (D_{water} + D_{SL})\, \tau_{corr,bulk} / \tau_{corr,local} \quad (1.2)$$

A previous study showed that the relationship between the two measures of retardation, ($\tau_{corr,local}/\tau_{corr,bulk}$) and ($k_{\sigma,\mathrm{bulk}}/k_{\sigma,\mathrm{local}}$), is approximately linearly up to a retardation factor of ~6, and after this continues to increase monotonically. However, as noted above, eq. (1.2) assumes isotropic water motion and 3-dimensional access to the spin probe, which does not hold for surfaces, meaning the absolute magnitudes of retardations measured in terms of k_σ and τ_{corr} will differ. Nevertheless, the linear relationship between k_σ and τ_{corr} retardation means that, although different in magnitude, trends in hydration water retardation will be the same. Thus, in this thesis, we rely solely on k_σ retardation to obtain D_{local} values.

1.4.4 *Operando* ^{13}C MAS NMR spectroscopy

The drawbacks of ex situ methods are that each data point represents a perturbation of the system, and curvefits of a small number of data points can miss subtle features in the kinetic profile. In contrast, *operando* measurements (in which spectra and kinetics are observed concurrently) provide information without sampling and generally give much more data regarding temperature- and time-dependent changes in chemical species. To make *operando* NMR measurements of solid catalysts, a new MAS NMR rotor, named a WHiMS rotor after its inventors, was used.[9] This rotor allows observations at high pressures and

temperatures (e.g., 400 bar at 20 °C, or 225 bar at 250 °C). This range includes many reactions of interest.

Scheme 1 shows the design of a WHiMS MAS rotor. Catalyst and solvent are loaded into a rotor and a bushing with two O-rings is installed. Next, the rotor is sealed with a screw and placed inside a pressure vessel. When the pressure is increased, gas flows into the rotor and equalizes with the pressure in the vessel by causing the O-rings to flex. Upon depressurizing the pressure vessel, the pressurized rotor is sealed. ^{13}C-enrichment is helpful in order to obtain ^{13}C NMR kinetic profiles in a short period of time. Peak areas are readily converted to concentration for each chemical species.

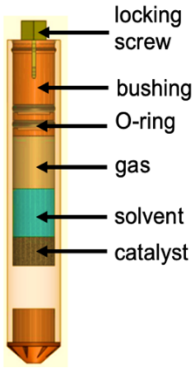

Scheme 1.1. Design of the WHiMS MAS rotor used for *operando* NMR experiments.[9]

1.5 References

(1) Stein, A.; Melde, B. J.; Schroden, R. C. Hybrid Inorganic-Organic Mesoporous Silicates—Nanoscopic Reactors Coming of Age. *Adv. Mater.* **2000**, *12* (19), 1403–1419.

(2) Wang, X.; Du, X.; Li, C.; Cao, X. Direct Synthesis and Characterization of Phenyl-Functionalized SBA-15. *Appl. Surf. Sci.* **2008**, *254* (13), 3753–3757.

(3) Inagaki, S.; Guan, S.; Ohsuna, T.; Terasaki, O. An Ordered Mesoporous Organosilica Hybrid Material with a Crystal-like Wall Structure. *Nature* **2002**, *416* (6878), 304–307.

(4) Yoshina-Ishii, C.; Asefa, T.; Coombs, N.; MacLachlan, M. J.; Ozin, G. A. Periodic Mesoporous Organosilicas, PMOs: Fusion of Organic and Inorganic Chemistry 'inside' the Channel Walls of Hexagonal Mesoporous Silica. *ChemComm* **1999**, No. 24, 2539–2540.

(5) Olkhovyk, O.; Pikus, S.; Jaroniec, M. Bifunctional Periodic Mesoporous Organosilica with Large Heterocyclic Bridging Groups and Mercaptopropyl Ligands. *J. Mater. Chem.* **2005**, *15* (15), 1517.

(6) Catalan, J.; Perez, P.; Laynez, J.; Blanco, F. G. Analysis of the Solvent Effect on the Photophysics Properties of 6-Propionyl-2-(Dimethylamino)Naphthalene (PRODAN). *J. Fluoresc.* **1991**, *1* (4), 215–223.

(7) Franck, J. M.; Pavlova, A.; Scott, J. A.; Han, S. Quantitative Cw Overhauser Effect Dynamic Nuclear Polarization for the Analysis of Local Water Dynamics. *Prog. Nucl. Magn. Reson. Spectrosc.* **2013**, *74*, 33–56.

(8) Ottaviani, M. F.; Garcia-Garibay, M.; Turro, N. J. TEMPO Radicals as EPR Probes to Monitor the Adsorption of Different Species into X Zeolite. *Colloids Surf., A* **1993**, *72*, 321–332.

(9) Walter, E. D.; Qi, L.; Chamas, A.; Mehta, H. S.; Sears, J. A.; Scott, S. L.; Hoyt, D. W. *Operando* MAS NMR Reaction Studies at High Temperatures and Pressures. *J. Phys. Chem. C* **2018**, *122* (15), 8209–8215.

Chapter 2. Tuning molecular adsorption in SBA-15-type periodic mesoporous organosilicas by systematic variation of their surface polarity

2.1 Abstract

Surface polarity plays a key role in controlling molecular adsorption, with major implications for reactions and separations both separately and in combination. In this study, the polarity of periodic mesoporous organosilicas (PMOs) was varied by co-condensing $Si(OEt)_4$ with various organodisilanes, to create a homologous series of materials with similar surface areas, pore volumes, and hydroxyl contents, but different chemical compositions. Their relative surface polarities cover a wide range, established by measuring the fluorescence of a solvatochromic dye, Prodan, adsorbed onto each organosilica surface. The EPR spectra of materials modified with tethered nitroxide radicals reveal monotonically decreasing mobility as more of the radicals interact strongly with the increasingly non-polar surface. The surface properties of the PMOs are correlated with their affinities for organic molecules dissolved in various solvents. The most polar material has negligible affinity for the organic molecules phenol, *p*-cresol, or furfural dissolved in water. However, adsorption becomes increasingly favorable as the surface polarity decreases, due to stronger solute-surface interactions. Interestingly, the trend is reversed for furfural when this solute was dissolved in benzene, resulting in much greater adsorption on more polar surfaces due to weaker solvent-surface interactions. Thus, the polarity of the surface relative to the solvent is critical for systematic tuning of molecular adsorption equilibria. These findings demonstrate that

adsorption/desorption can be significantly altered by the rational choice of solvent and surface, and that improved catalytic processes can be designed using this information.

2.2 Introduction

Modulating the polarity of the condensed phase reaction environment by changing the solvent is a promising strategy to improve the efficiency of emerging energy technologies like the valorization of biomass, by increasing the activity and selectivity of catalysts.[1–3] For example, levulinic acid yields from acid-catalyzed dehydration of mono- and oligosaccharides are highest in water compared to THF or toluene, since oligomerization side-reactions are suppressed by better solvation of sugars and their dehydration products in the aqueous solution.[4] The polarity of the reaction medium can also be modified by including a co-solvent, or by adding a salt.[5,6]

In the case of heterogeneous catalysts, surface polarity can influence catalytic activity by altering the adsorption of molecules at or near the active sites, as well as the activation barriers for reactions at those sites. Thus, Pd supported on a hydrophilic zeolite showed higher furfural conversion and selectivity to furan to Pd on a hydrophobic zeolite, due to the higher affinity of the former catalyst for furfural relative to furan.[7] The surface polarity depends on the chemical composition of the catalyst,[1,2,8] but modifying this composition often changes other influential characteristics such as textural properties, the extent of confinement, the number of active sites, and even their identity. The resulting complexity hinders the investigation of correlations between surface polarity and catalytic activity/selectivity. For example, the surface polarities of zeolites and ZrO_2 increase in parallel with increasing

numbers of strong Brønsted acid sites.[9,10] To achieve a desired reactivity, the polarity of both the catalyst and the solvent system must be tuned precisely and independently.

Some catalyst support materials, such as silicas and carbons, are readily modified post-synthesis with varying types and concentrations of chemically distinct components that alter their surface polarity.[7,11,12] For example, the pore surfaces of ordered mesoporous silicas (e.g., MCM-41, SBA-15) can be functionalized by anchoring hydrocarbon chains and/or other functional groups to change the interfacial polarity.[13,14] However, other synthesis methods do not allow independent control of polarity and textural properties.[7,14,15] Co-condensation is a powerful strategy to separate these effects, since two or more different types of (organo)silica precursors can be incorporated in varying amounts, while controlling the morphology through the use of a templating agent.[16] Nevertheless, differences in condensation rates can cause significant changes in surface area and/or pore volume, and increase variability in the series of target materials.[17,18] In this work, we synthesized a family of periodic mesoporous organosilicas (PMOs) with similar meso- and macrostructures, surface areas and pore volumes, by co-condensing an inorganic silica source with varying amounts of two organodisilanes to create hybrid materials with gradually increasing organic content (Scheme 2.1).

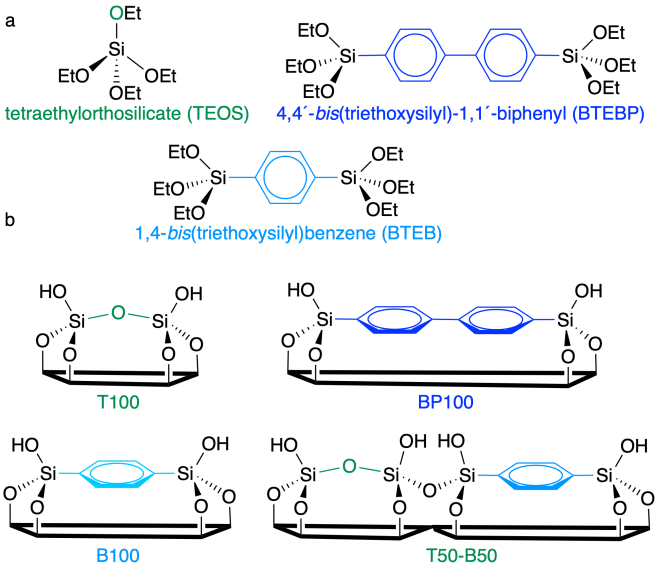

Scheme 2.1. (a) Chemical structures of the three silica precursors used in this work, and (b) the surface compositions of some of the resulting SBA-15-type materials.

An assessment of surface polarity is required to describe the effect of compositional changes on adsorption. Contact-angle measurements and water vapor adsorption isotherms correlate with surface polarity,[7,19,20] but their interpretation can be complicated for rough heterogeneous surfaces and porosity. Instead, the polarity of each PMO was determined by comparing the fluorescence of an adsorbed solvatochromic dye, Prodan, with the fluorescence of the same dye in various solvents of known polarity. This technique was used in a previous study to estimate the interfacial polarity of MCM-41-type materials whose pore surfaces were functionalized with diverse organic groups such as methoxypropyl, cyanoethyl, etc.[13] In addition, EPR lineshape analysis was used to assess changes in mobility of TEMPO (2,2,6,6,-tetramethylpiperidinyloxy) spin labels covalently attached to and interacting with PMO surfaces.[21,22] Finally, we explored how surface and solvent polarity together controlling the extent of adsorption of representative organic molecules relevant to the conversion of

lignocellulosic biomass.

2.3 Materials and methods

2.3.1 Chemicals

Tetraethylorthosilicate (TEOS, 98%), 1,4-bis(triethoxysilyl)benzene (BTEB, 96%), 4,4′-bis(triethoxysilyl)1-1′-biphenyl (BTEBP, 95%), Pluronic 123, *p*-cresol (99%), phenol (99%), furfural (99%), anisole (>99%), vanadium oxytrichloride (99%) and *N*-(3-dimethylaminopropyl)-*N*- ethylcarbodiimide hydrochloride, and *N,N*-dimethyl-6-propionyl-2-naphthylamine (Prodan) were purchased from Sigma Aldrich. 4-Carboxy-TEMPO and 3-aminopropyldimethylethoxysilane were purchased from Santa Cruz Biotechnology and Gelest, Inc., respectively. Deuterium oxide (99.9%), dimethylsulfoxide-d_6 (99.9%) and benzene-d_6 (99.5%) were obtained from Cambridge Isotope Laboratories, Inc. All chemicals were used as-received.

2.3.2 Synthesis of PMOs based on TEOS, BTEB, and their mixtures

Following a literature procedure for the synthesis of SBA-15,[23] Pluronic P123 (3.0 g) was dissolved with a stirring in 0.2 M aqueous HCl (106 mL) overnight in a tightly sealed glass flask. The solution temperature was lowered to ~2 °C with an ice bath and TEOS (30 mmol, 6.68 mL) was added dropwise at a rate of ca. 1 mL/min while stirring at 150 rpm. After 1 h, the solution was heated to 40 °C in a water bath and stirred for 23 h. The reaction mixture was transferred to a Parr pressure reactor equipped with a Teflon liner (125 mL) and placed in an oven at 100 °C for 48 h. The resulting suspension was filtered and washed with ~500 mL water, then dried overnight in air at 100 °C. Residual P123 was removed by ethanol

Soxhlet extraction at 110 °C in an oil bath for 24 h. Finally, the material was dried at 70 °C in air for 12 h to remove ethanol and the remaining P123 was eliminated by calcination at 250 °C in air for 3 h. At this temperature, residual P123 decomposes, while organic groups in the framework are preserved.[24]

The synthesis procedure was adjusted to prepare the material based on BTEB. In general, fully siliceous SBA-15 is best synthesized under acidic conditions, with HCl concentrations in the range 1.5-2.0 M (corresponding to a HCl:H_2O molar ratio of ca. 0.03). However, when BTEB is injected in this pH range, the hydrolysis of the organodisilane is much faster than that of TEOS.[25–27] Consequently, the organosilane condenses rapidly without sufficient interacting with P123, resulting in a poorly ordered structure. Thus, hydrothermal reaction at 40 °C for 24 h gave a dense white precipitate and a semi-transparent gel. The XRD pattern of the powder recovered from the white precipitate lacks the (110) and (220) reflections characteristic of long-range mesopore ordering. A lower HCl:H_2O molar ratio (between 10^{-3} and 10^{-4}) retards the hydrolysis/condensation of the organosilane, although mesoscale ordering is not greatly affected until the isoelectric point (pH ~2) is reached.[26,27] Therefore a ten-fold smaller HCl concentration, 0.2 M, was used.

PMOs containing various fractions of phenylene bridging groups in the framework were synthesized using mixtures of TEOS and BTEB, whose relative amounts were adjusted as shown in Table A2.1 to ensure mesostructure formation. For co-condensed materials, the appropriate ratio of precursors is determined by the strengths of their interactions with P123. Here, the same amount of P123 was used in all syntheses, but the relative amounts of TEOS and BTEB were adjusted (see Table A2.1). Each material is named according to the type of

silane precursor (T: TEOS; B: BTEB; BP: BTEBP) and their relative proportions. For example, T50-B50 was synthesized using 50 % TEOS and 50 % BTEB as silica precursors.

2.3.3 Synthesis of BTEBP-containing PMOs

Well-ordered B75-BP25 was made following the procedure described above, by co-condensing 5.5 mmol BTEB with 1.8 mmol BTEBP. However, the same reaction conditions did not lead to mesophase formation in the fully biphenylene-bridged PMO (BP100). Therefore, BP100 was synthesized using 1-butanol[28,29] as a co-surfactant with P123, following the method described by Yang et al.[30] P123 was dissolved in acidic aqueous solution (0.5 M HCl, 106 mL), then 1-butanol (11 mmol) was added at room temperature. After stirring for 1 h, BTEBP (6.5 mmol) was added and the solution temperature was increased to 40 °C. After 24 h, the reaction mixture was transferred to a Parr pressure reactor (125 mL), where it was aged at 100 °C for 48 h. The surfactant was removed following the procedure described above.

2.3.4 Materials characterization

Powder X-ray diffraction patterns were acquired from 0.5 to 3° [2θ], and from 5 to 50° [2θ], using a Rigaku X-ray diffractometer with Cu Kα radiation. N_2 sorption isotherms were measured at 77 K using 3Flex Micrometrics equipment. Before measurement, each material was outgassed at 423 K for 8 h in flowing N_2 to remove physically adsorbed water. The apparent surface area was calculated using the Brunauer-Emmett-Teller (B.E.T.) equation, assuming a molecular area for adsorbed N_2 of 0.135 nm^2.[31] The total pore volume was obtained from the amount of N_2 adsorbed at P/P_0 = 0.99. The average pore diameter was calculated by analyzing the adsorption branch of the N_2 isotherm, using the Barret-Joyner-

Halenda (B.J.H.) method. ^{13}C CP-MAS NMR spectra were acquired at room temperature on a 500 MHz WB Bruker Avance NMR Spectrometer, in an 11.7 T magnetic field.

2.3.5 Silanol group quantification

The number of accessible surface silanol groups was determined via reaction with $VOCl_3$.[32] A PMO sample (ca. 40 mg) was placed in a Schlenk flask and evacuated at 0.1 mTorr and 170 °C for 7 h to remove physisorbed water. Its absence from the dry PMO was confirmed by IR. Excess $VOCl_3$ vapor (ca. 1 mmol) was transferred under reduced pressure at room temperature and allowed to react for 30 min. The chemisorbed vanadium was extracted from a precisely weighed sample (approx. 10 mg) by stirring in 5 mL of 1 M H_2SO_4 solution containing H_2O_2 (0.26 M).[32] The resulting solution contains a mixture of red-brown *mono*- and *bis*(peroxo)vanadium(V) complexes. The absorbance, measured at 448 nm using a Shimadzu UV-2401 UV-vis spectrophotometer, was compared to a calibration curve prepared using ammonium vanadate under same experimental conditions. The calculation of vanadium content was corrected for the change in PMO mass caused by modification with $VOCl_3$ as follows: for x mg V-modified PMO, and a measured vanadium concentration in the solution of y mmol/mL, the amount z of unmodified PMO present in the analysis solution (mg/mL) is $z = (x/5) - 136.8y$, where 136.8 mg/mmol is the difference in molecular between [$VOCl_2$] and the proton it replaces. Since the vanadium content is equal to the number of accessible silanols,[32] the SiOH surface density (α_{OH}) is y/z mmol/mg.

2.3.6 Fluorescence measurements

An aqueous solution of Prodan (15 μM) was prepared by vigorous stirring at room temperature for 6 h. Each PMO (20 mg) was stirred with 15 mL Prodan solution for 10 h, then centrifuged at 3000 rpm for 15 min. The supernatant liquid was decanted and the solid was dried at 100 °C for 6 h in air. Emission spectra for the dry powders were recorded with a Horiba FluoroMax 4 spectrometer, using an excitation wavelength of 365 nm. The peak maximum λ_{max} was obtained from the zero-crossing of the first-derivative. Spectra were also acquired for each PMO powder dispersed in water. Relative polarity values were interpolated using the solvent correlation between relative polarity[33] and λ_{max} recorded for dissolved Prodan,[34] fitted using a second-order polynomial function.

2.3.7 EPR spectroscopy

For selected PMOs, a small fraction (ca. 1 %) of surface silanols were modified with TEMPO (referred to as the spin label), using the coupling reaction between tethered propylamine and carboxy-substituted TEMPO, following a slightly modified literature procedure.[35,36] Each PMO (20 mg) was suspended in phosphate buffered saline solution (pH 7.4, 2 mL), then 3-aminopropyldimethylethoxysilane (APDMES, 16 μL) was added and the mixture was stirred for 18 h at room temperature. The solid was separated by centrifugation and combined with 4-carboxy-TEMPO (0.5 mL, 10 mM in 2-morpholin-4-ylethanesulfonic (MES) acid buffer, pH 4.5) and *N*-(3-dimethylaminopropyl)-*N*-ethylcarbodiimide hydrochloride (1.2 mL, 50 mM in pH 4.5 MES buffer).

After 48 h incubation at room temperature, the mixture was centrifuged at 3000 rpm for 4 min. (A much shorter reaction time, 30 min, was previously reported for TEMPO functionalization of amine-modified non-porous silicas,[36] but resulted here in subsequent

partial peptide bond cleavage, possibly catalyzed by residual unreacted propylamine groups. To prevent contamination by untethered radicals during EPR measurements, the reaction time was extended.) The supernatant liquid was removed and the solid was resuspended in DI water. This step was repeated 10 times to remove unreacted 4-carboxy-TEMPO completely, as judged by the absence of EPR signals for the untethered radical. The resulting tethered TEMPO radicals appeared to be stable for the duration of the EPR measurement (ca. 6 h); no signals for untethered radicals reappeared during this time.

The spin-labeled material (ca. 4 μL of a PMO slurry, 40 mg/mL) was placed in a quartz capillary (0.60 mm I.D., 0.84 mm O.D.). X-band continuous-wave (CW) EPR spectra were recorded on a Bruker EMSplus EPR spectrometer, using a Bruker ER 4119HS-LC high sensitivity resonator at a microwave frequency of ca. 9.3 GHz, with 1 mW irradiation power and 0.4 G modulation width. The spectra were simulated by lineshape fitting using the SimLabel software,[37] which relies on the same functions as EasySpin.[38]

2.3.8 Quantitative adsorption measurements

Each silica (20 mg) was mixed with a solution containing *p*-cresol, phenol, or furfural (dissolved in 1.5 mL of the specified deuterated solvent) in a 2 mL centrifuge tube. The slurry was agitated in an IKA Vortex 4 digital mixer at 3000 rpm for 10 h, then centrifuged at 3000 rpm for 8 min to separate the solid. The supernatant was decanted, for quantitative analysis by solution-state ^{1}H NMR (Varian Unity, 500 MHz) with DMSO as an internal standard. When DMSO-d_6 was used as the solvent, the residual solvent peak was used as the standard instead.

2.4 Results and discussion

2.4.1 Synthesis and characterization of Periodic Mesoporous Organosilicas (PMOs)

In order to obtain materials with uniform morphologies and a range of surface polarities, a series of SBA-15-type PMOs were synthesized. Three different silanes: tetraethylorthosilicate (TEOS), 1,4-bis(triethoxysilyl)benzene (BTEB), and 4,4′-bis(triethoxysilyl)-1,1′-biphenyl (BTEBP), were chosen as (organo)silica precursors (Scheme 2.1a), for incorporation in various ratios into the ordered mesoporous SBA-15 framework. The TEOS-based material (T100) is expected to have the most polar surface, while the BTEBP-based PMO (BP100) should be the least polar due to its bridging biphenylene groups, Scheme 2.1b. Intermediate surface polarities are expected for the BTEB-based material (B100), and for co-condensed mixtures of TEOS/BTEB, or BTEB/BTEBP.

Representative SEM images for the PMOs show elongated fibers with diameters of 0.3-0.6 μm and lengths of 2-10 μm (Fig. A2.1), consistent with previous studies.[23,24] However, BP100 has a distinctive, particulate structure. The incorporation of phenylene and/or biphenylene-bridged groups into the organosilica framework was confirmed by ^{13}C solid-state CP/MAS NMR (Fig. A2.2). Low- and wide- angle XRD patterns ($0.6 \leq 2\theta \leq 3$ °) for the various SBA-15s were recorded after surfactant removal (Fig. A2.3 and A2.4). The appearance of clear d_{110} and d_{220} reflections in the low-angle region is evidence for mesopores with a high degree of long-range order for all materials except BP100. The d_{100} reflections are similar except for T100, whose lowest angle peak is displaced indicating a slightly larger unit-cell size (from ca. 120 to 130 Å). Assuming similar wall thicknesses, this finding implies a slight increase in pore size. The XRD pattern of BP100, whose synthesis requires the use of a 1-butanol as co-surfactant to ensure mesophase formation, does not contain clear low-angle

peaks, implying the pores are less uniform. Its average pore size was obtained by N_2 physisorption instead, and is similar to that of the other materials, Table 2.1.

The physicochemical properties of the PMOs are compared in Table 2.1. Their B.E.T. surface areas vary over a relatively small range, from 668 to 728 m^2/g, as do their B.J.H. pore sizes (6.3 to 7.4 nm) and pore volumes (0.99 to 1.12 m^3/g). However, T100 has a slightly higher pore size (9.6 nm), consistent with its lower angle d_{100} peak position, while BP100 has a slightly higher pore volume (1.52 cm^3/g) consistent with a slightly different pore morphology. Nevertheless, the variability is small compared to families of materials used in previous comparative studies of surface polarity effects on catalysis (in which reported surface areas, pore sizes or pore volumes varied by factors of 2-4).[9,15,39] Thus, the PMOs in this work are well-suited for investigating the effect of surface polarity on adsorption capacity, while keeping structural factors constant.

Table 2.1. Physicochemical properties of PMO materials

PMO	B.E.T. surface area [a] (m^2/g)	pore volume (cm^3/g)	pore size [b] (nm)	Silanol surface density, α_{OH} (mmol/g) [c]	(OH/nm^2) [d]
T100	709	1.12	9.6	2.1	1.8
T75-B25	668	0.99	7.4	1.7	1.5
T50-B50	694	1.00	7.5	1.7	1.5
T25-B75	708	1.08	7.4	2.1	1.8
B100	721	1.08	7.4	1.5	1.3
B75-BP25	719	1.01	6.3	2.1	1.8
BP100	728	1.52	7.4	1.9	1.6

[a] Calculated using the Brunauer-Emmett-Teller (B.E.T.) method. The generally accepted measurement error in B.E.T. surface areas is ± 10 %.[40] The calculations assume an area for adsorbed N_2 of 0.135 nm^2/molecule, which is the value appropriate for perpendicular adsorption on oxide surfaces.[31] Since N_2 adsorbs parallel to the surface on organic materials, occupying a larger area (0.162 nm^2), the actual surface areas of the organosilicas may be higher. However, the fractions of parallel vs. perpendicularly adsorbed N_2 are not known. Finally, B.E.T surface areas normalized by mass do not reflect differences in skeletal densities for silicas with different organic fractions. [b] Calculated using the Barrett-Joyner-Halenda (B.J.H.) method, using the adsorption branch of the isotherm, and reported as the average pore size. [c] The measurement error associated with these values is estimated to be ± 0.1 mmol/g. [d] The error generated due to the experimental uncertainty in the surface area measurements is ± 0.3 nm^{-2}.

2.4.2 Surface hydroxyl content

Condensation of TEOS and/or organodisilanes leaves dangling alkoxy groups at the surface which do not undergo further condensation. Upon hydrolysis, these groups are converted to surface hydroxyls, some of which resist dehydration even at high temperatures.[41] Surface polarity is affected by the surface density of these silanols, as well as by the nature and extent of organic content at the interface. The surface silanols present in each PMO were quantified by their reaction with $VOCl_3$.[32] The number of $VOCl_3$-accessible surface OH groups is fairly constant, ranging from 1.5 to 2.1 mmol/g (1.3-1.8 OH/nm^2, Table 2.1). However, the surface silanol content of T100 is 2-3 times smaller than previously reported values for SBA-15 (3.5 mmol/g)[42] and MCM-41 (3.6 to 5.3 mmol/g).[42,43] Conventional measurement methods count both accessible surface OH groups and inaccessible sub-surface OH groups. Notably, a study of the number of OH sites that react with trimethylsilyl chloride reported much lower OH contents for SBA-15 and MCM-41 (1.8 and 2.2 mmol/g, respectively).[42] These values are much closer to the number of surface OH groups measured here. Thus, SBA-15 type materials using TEOS, BTEB, and BTEBP precursors have similar numbers of accessible silanol groups, and differ significantly only in the type and amount of framework organic groups.

2.4.3 Solvatochromic assessment of gradually varying surface polarity

Water affinity can assess surface polarity indirectly, i.e., by measuring hydrophilicity.[7,44] For example, water vapor adsorption isotherms were used to obtain qualitative information about surface wettability via comparison of the onset pressures for pore condensation.[19,20] However, hydrophilicity and polarity are distinct physical properties. Polarity can be probed more

directly using fluorescent organic dyes such as Prodan, whose electronic energy levels are affected by non-covalent interactions with its surroundings. The maximum fluorescence wavelength therefore depends on the polarity of the solvent in which the dye is dissolved (Fig. 2.1a). Increasing solvent polarity is associated with a gradual shift in its emission spectrum.[11,13,34]

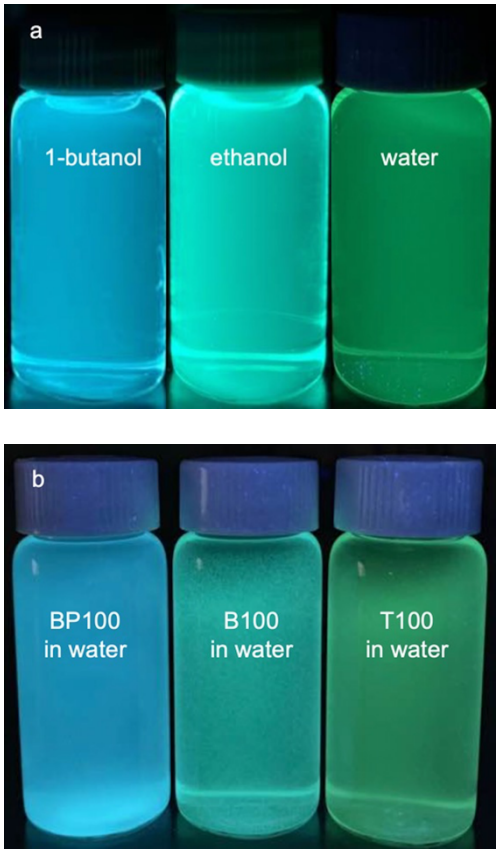

Fig. 2.1. Comparison of Prodan fluorescence: (a) dissolved in various solvents as indicated; and (b) adsorbed on three different PMO materials, all suspended in water.

Adsorbed Prodan can thus report on the polarity of PMO surfaces influenced by the presence of surface organic groups. Fig. 2.1b shows the range of emission colors for Prodan adsorbed on three representative PMO powders, each suspended in water. The blue

fluorescence of BP100 reflects a less polar surface than that of either turquoise-fluorescing B100 or green-fluorescing T100. The fluorescence spectra remained unchanged for at least an hour at room temperature, demonstrating that the dye is strongly adsorbed and does not leach into the water.

Emission spectra for Prodan adsorbed on the various dry PMO powders are shown in Fig. 2.2a. The shortest fluorescence emission wavelength, for BP100 (λ_{max} 473 nm), is consistent with its lower polarity compared to B100 (λ_{max} 489 nm) and T100 (λ_{max} 509 nm, Table A2.2). The gradual shift of λ_{max} for intermediate PMO compositions shows that the surface polarity of these materials can be finely tuned.

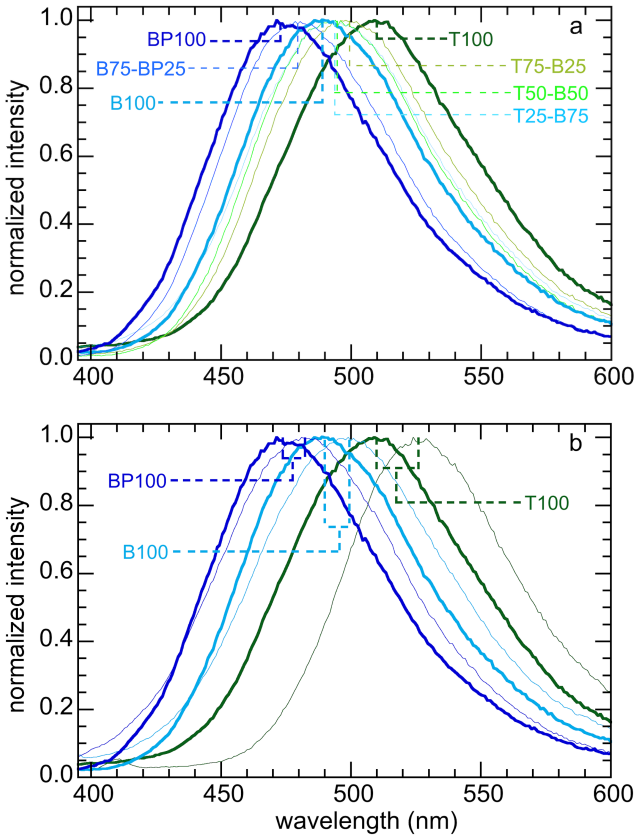

Fig. 2.2. Normalized emission spectra of Prodan: (a) adsorbed on various dry (organo)silica powders; and (b) comparison of selected dry powders (heavier lines) with the same powders suspended in water (lighter lines).

Fluorescence spectra were also recorded for aqueous suspensions of each PMO, following a previously described method.[11,13] Fig. 2.2b compares the spectra for selected materials with those for Prodan adsorbed on the corresponding dry powders. Dispersion of a PMO in water results in a red-shift in the corresponding emission spectrum, consistent with greater surface hydration and hence increased interfacial polarity. However, the magnitude of the shift in λ_{max} is not constant. It is largest (17 nm) for the most polar material, T100, and smallest (9 nm) for the least polar material (BP100). This finding is consistent with a greater extent of hydration for the more polar surfaces.

Relative surface polarity values for each PMO were obtained using λ_{max} values for the adsorbed Prodan and interpolating λ_{max} values measured in various solvents of known polarity (Table A2.3).[34] The results are shown for both dry and wet PMO materials in Fig. 2.3 and Table A2.4. The dry PMO powders have *relative surface polarities* from 0.50 to 0.81. All values are higher when the powders are suspended in water, due to surface hydration. The relative polarity of dry T100 is similar to that of methanol, while hydrated T100 has a polarity close to that of water. Dry BP100 is less polar than 1-octanol, but wet BP100 has a surface polarity closer to that of 1-butanol. The relationship between pairs of λ_{max} values is linear, but the slope is not unity (Fig. 2.3c). Thus hydration is more extensive for more polar materials.

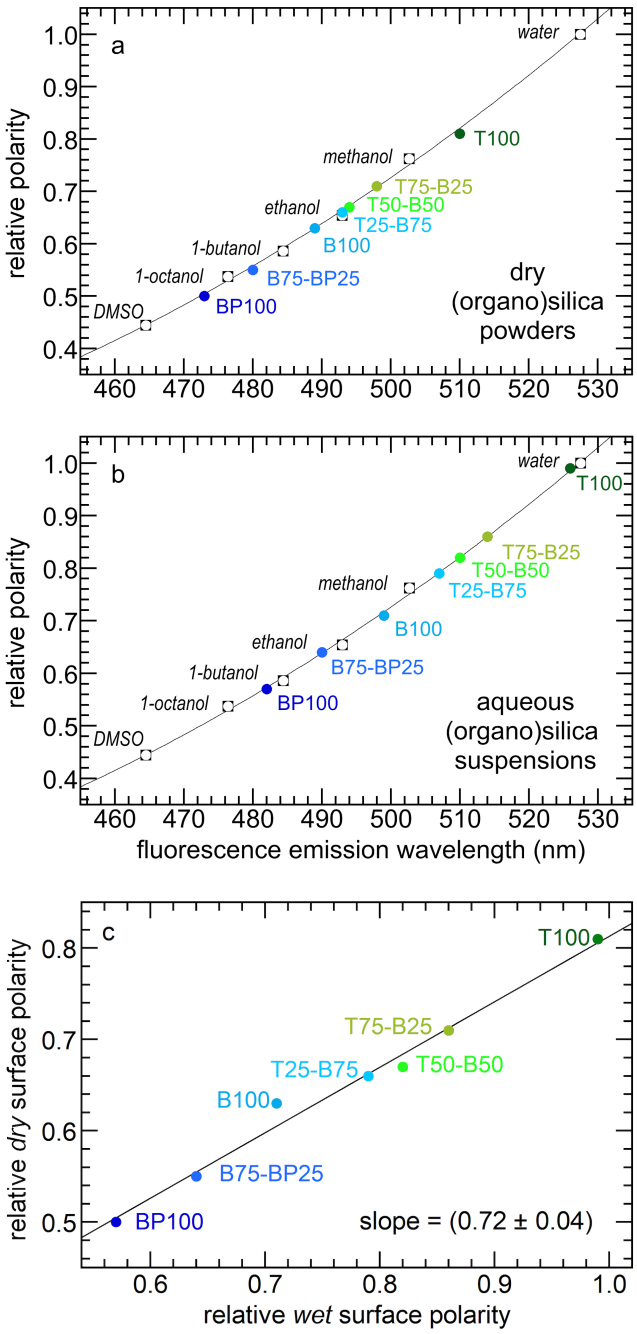

Fig. 2.3. Correlations between the relative polarities of various solvents[33] and Prodan fluorescence emission maxima for (a) dry PMO powders, or (b) PMOs suspended in water; and (c) relationship between the relative surface polarities of the dry PMO powders and their aqueous suspensions.

2.4.4 Mobility of adsorbed species

Molecular mobility is inversely correlated with adsorption strength. EPR line-shape analysis can provide information about the relative mobility of surface-confined spin labels.[45–47] We acquired EPR spectra of TEMPO radicals attached to aminopropylsilane-modified PMOs (Scheme A2.1). Low spin concentrations minimize EPR line-broadening effects caused by strong dipolar interactions between neighboring spin labels,[45] therefore only a small fraction (ca. 1 %) of surface silanols were functionalized with nitroxide radicals. X-band EPR spectra recorded at room temperature for the spin-labeled PMOs suspended in water are shown in Fig. 2.4. Variations reflect differences in the average local dynamics of the tethered spin-labeled moieties due to the strength of their interactions with the surface, Scheme 2.2.

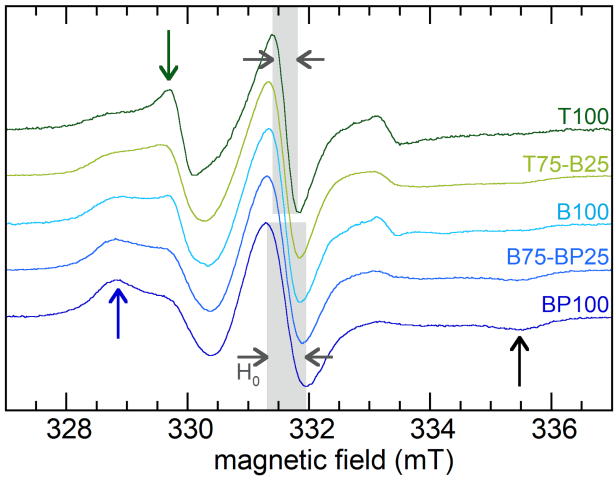

Fig. 2.4. Continuous-wave EPR spectra, recorded at room temperature, for various 4-carboxy-TEMPO-functionalized PMOs suspended in water. Blue and green arrows indicate peaks associated with slower- and faster-moving radicals, respectively. The emergence of a weak peak at high field (black arrow) is also characteristic of an increased fraction of slow-moving radicals.

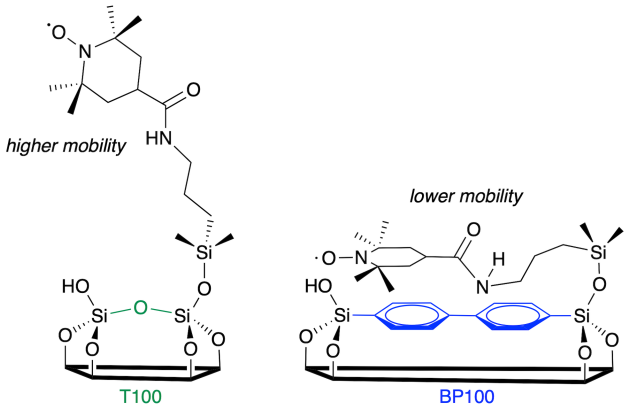

Scheme 2.2. Two possible orientations of tethered TEMPO spin labels, with different mobilities depending on the extent of their interaction with the PMO surface.

Restricted spin motion caused by greater proximity of the tethered radical to the surface results in incomplete averaging of anisotropic terms of the magnetic Hamiltonian. This effect is manifested qualitatively in various types of line broadening and appearance of distinct spectral features.[48,49] First, the line width (H_0) of the central peak increases gradually,[21,50] from 0.47 to 0.67 mT (grey-shaded region) as the surface polarity decreases from T100 to BP100. The eventual appearance of an outer extremum at 335.5 mT (black arrow) is also a well-established indicator of diminished rotational motion.[21,49] In addition, the gradually changing intensities of two partially resolved peaks at 328.8 mT (blue arrow) and 329.7 mT (green arrow) represent varying populations of slow and fast components, respectively. Further line broadening is caused by the increasing fraction of the slow component.

The A_{zz} component of the nitrogen hyperfine tensor element parallel to B_0 (i.e., aligned with the *z*-direction) also varies with local polarity, due to changes in localization of the unpaired electron along the N-O bond axis (perpendicular to the *z*-axis) modulated by changes in the local electric field.[22] In spin-labeled membrane proteins, A_{zz} values increase from 3.43

to 3.65 mT with the polarity of the membrane and the protein micro-environment.[22] X-band EPR spectra of suspensions of BP100, B100 and T100, acquired at 120 K, are shown in Fig. A2.5. They show that A_{zz} increases gradually with increasing polarity, from 3.76 to 3.93 mT (Table 2.2).

In order to quantify changes in the relative mobilities of tethered TEMPO radicals, the room temperature EPR spectra of T100, B100 and BP100 were deconvoluted into two components. These components represent faster- and slower-moving populations of the spin label, corresponding to radicals experiencing weaker and stronger interactions, respectively, with the PMO surface. Simulations were performed with the appropriate A_{zz} value for each PMO (measured at low temperature) and a reported value of the *g*-tensor of the TEMPO radical[51] (precise determination of the *g*-tensor requires EPR lineshape analysis at higher field.)[52] The simulated EPR spectra and their deconvoluted components are shown in Fig. 2.5. For the most polar material (T100), the correlation times (τ_D) for the faster- and slower-moving components are 2.6 and 7.1 ns, respectively, with fractional contributions of 61 and 39 % (Table 2.2). For the least polar material (BP100), both correlation times are higher (3.5 and 8.6 ns), as is the fractional contribution of the slower component (86 %). These changes are consistent with enhanced interaction (and therefore lower mobility) with the less polar surface for a higher fraction of the tethered spin labels.

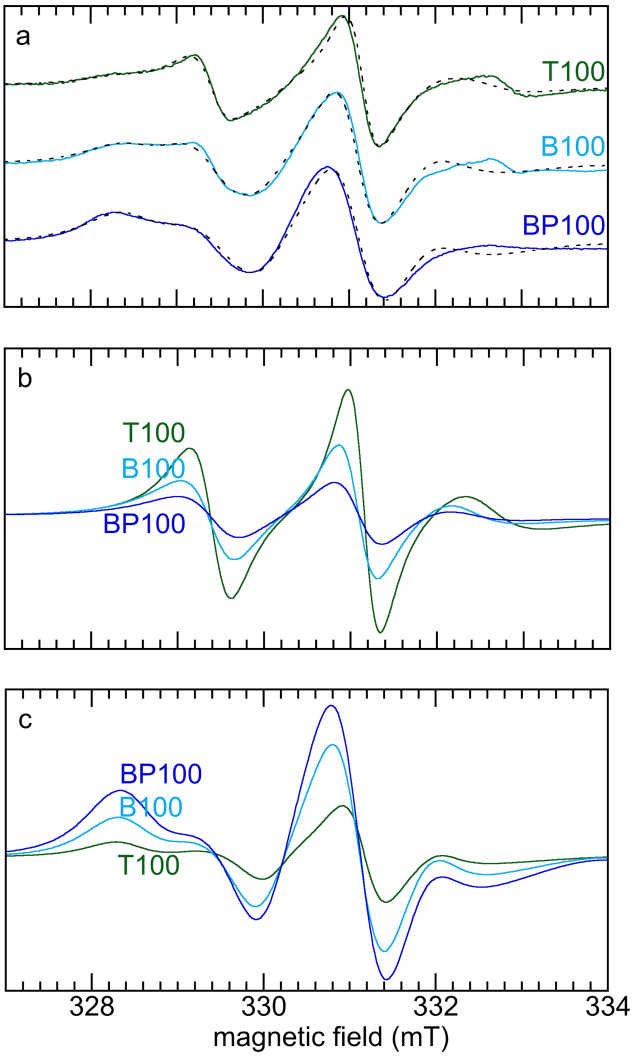

Fig. 2.5. (a) Comparison of experimental (solid color lines) and simulated (dashed black lines) EPR spectra for three PMOs functionalized with TEMPO, and deconvolution of each EPR spectrum into (b) faster, and (c) slower components. Simulations were performed using g = [2.0097, 2.0064, 2.0025],[51] and measured A_{zz} values (Table 2.2). Values for A_{xx} and A_{yy} (0.7 and 0.8 mT, respectively) were obtained as global curvefit parameters. The fraction of each component and its correlation time were refined for each fit.

Table 2.2. Characteristics of deconvoluted EPR spectra of TEMPO-modified PMOs

Material	A_{zz} (mT)[a]	τ_D (ns)[b]	
		Faster	Slower
T100	3.93	2.6 (0.61)	7.1 (0.39)
B100	3.83	3.3 (0.31)	7.4 (0.69)
BP100	3.76	3.5 (0.14)	8.6 (0.86)

[a] Measured at 120 K. [b] Values in parentheses represent fractional contributions for each component at room temperature.

2.4.5 Effect of surface polarity on molecular partitioning at solid-liquid interfaces

Adsorption of three different molecules (phenol, *p*-cresol, furfural) representative of common types of functional groups present in lignocellulosic biomass was studied across the range of PMO surface polarities. Fig. 2.6a shows adsorption isotherms measured at 296 K for three PMOs (T100, B100, and BP100) in contact with aqueous phenol solutions (with initial phenol concentrations from 10 to 85 mM). Although phenol can interact with surface hydroxyl groups via hydrogen-bonding, its affinity for T100 is very low. Furthermore, even though the surface hydroxyl densities are similar for all three silicas (Table 2.1), the extent of phenol adsorption increases dramatically as the surface becomes less polar. Thus, phenol is much more strongly adsorbed onto B100 and BP100 (ca. 0.6 and 1.2 mmol/g, respectively, at equilibrium).

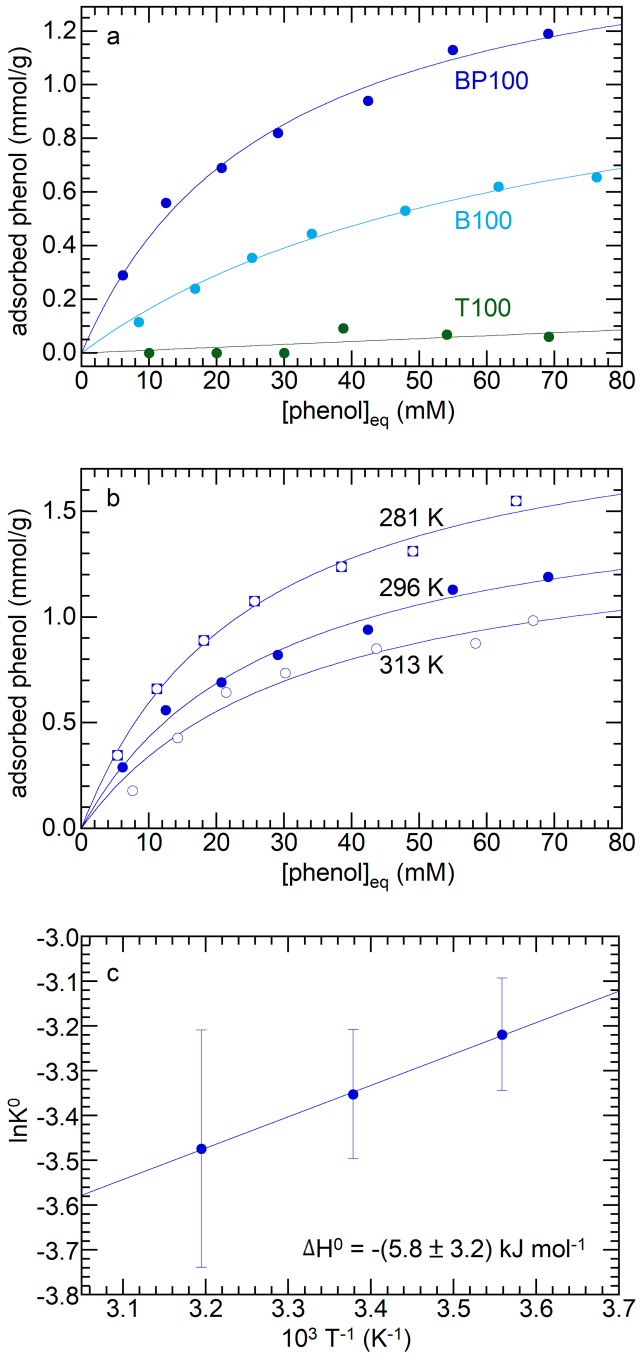

Fig. 2.6. Adsorption of phenol from water, onto: (a) T100, B100 and BP100, all at 296 K, and (b) BP100 at 281, 296, and 313 K. The isotherms (solid lines) represent non-linear curvefits using the Langmuir model (eq 1). (c) Van't Hoff plot for determination of adsorption enthalpy.

The adsorption isotherms for B100 and BP100 were analyzed with the Langmuir model (eq. 2.1), which assumes monolayer coverage of adsorbate on a surface with a fixed number of uniform adsorption sites. The equation relates q (the uptake of the adsorbate, in mmol/g adsorbent) to C_e (the equilibrium concentration in solution).

$$q = \frac{Q_L K_L C_e}{1+K_L C_e} \tag{2.1}$$

Q_L is the maximum adsorption capacity, and the Langmuir constant K_L represents the affinity of the adsorption sites. Curvefit parameters are shown in Table 2.3. The larger values of Q_L and K_L for BP100 compared to B100 confirm that phenol has a higher affinity for biphenylene relative to phenylene. For neutral adsorbates or adsorbates with small charges, K_L is essentially equal to the thermodynamic equilibrium constant $K°$.[53] The temperature dependence of $K°$ is described by the Van't Hoff equation (eq 2.2).

$$lnK^\circ = \frac{\Delta S^\circ}{R} - \frac{\Delta H^\circ}{RT} \tag{2.2}$$

The enthalpy of phenol adsorption, $\Delta H°$, was obtained by extracting K_L from adsorption isotherms recorded at different temperatures (Fig. 2.6b). According to Fig. 2.6c, the value of $\Delta H°$ for phenol adsorption from water onto BP100 is -(5.8 ± 3.2) kJ/mol, similar to a previously reported value for bentonite clay with intercalated hexadecyltrimethylammonium ions (-10.4 kJ/mol).[54] The small values represent the difference between phenol and water adsorption, including phenol desolvation.[55]

Table 2.3. Langmuir analyses of phenol adsorption from water onto PMO

Material	T (K)	Q_L (mmol/g)	K_L (L/mmol)
B100	296	1.26 ± 0.11	0.015 ± 0.002
BP100	313	1.45 ± 0.17	0.031 ± 0.008
	296	1.66 ± 0.10	0.035 ± 0.005
	281	2.07 ± 0.10	0.040 ± 0.005

To investigate how more systematic changes in surface polarity affect molecular adsorption, the affinities of the entire PMO series for phenol and the slightly less polar *p*-cresol were explored. Aqueous solutions of phenol show monotonically increasing adsorption as the polarity of the PMO decreases (Fig. 2.7a, Table A2.5). Water solvates the more polar surfaces effectively, suppressing phenol adsorption. Using a Born-Haber cycle for phenol adsorption at an aqueous-solid interface, we express the heat of adsorption as the sum of the energy costs to disrupt water-surface and water-phenol interactions, as well as the energy gains via new water-water and phenol-surface interactions.[55] The water-phenol and water-water contributions are the same for all materials, therefore the higher adsorption of phenol from water onto the less polar PMOs is driven by a combination of weaker water-surface and stronger phenol-surface interactions. Interactions unique to surface aromatic groups (phenylene and biphenylene), such as H-π and π–π, may also contribute to their higher affinities for phenol.[56] The effect is more pronounced for *p*-cresol (relative polarity 0.697) compared to phenol (relative polarity 0.701).[33] B100 and BP100 adsorb 48 and 38 % more *p*-cresol, respectively, than phenol. Since the water-surface interactions are the same, these

differences can be attributed solely to stronger solute-surface interactions which appear to be the dominant contributor to the overall adsorption enthalpy.

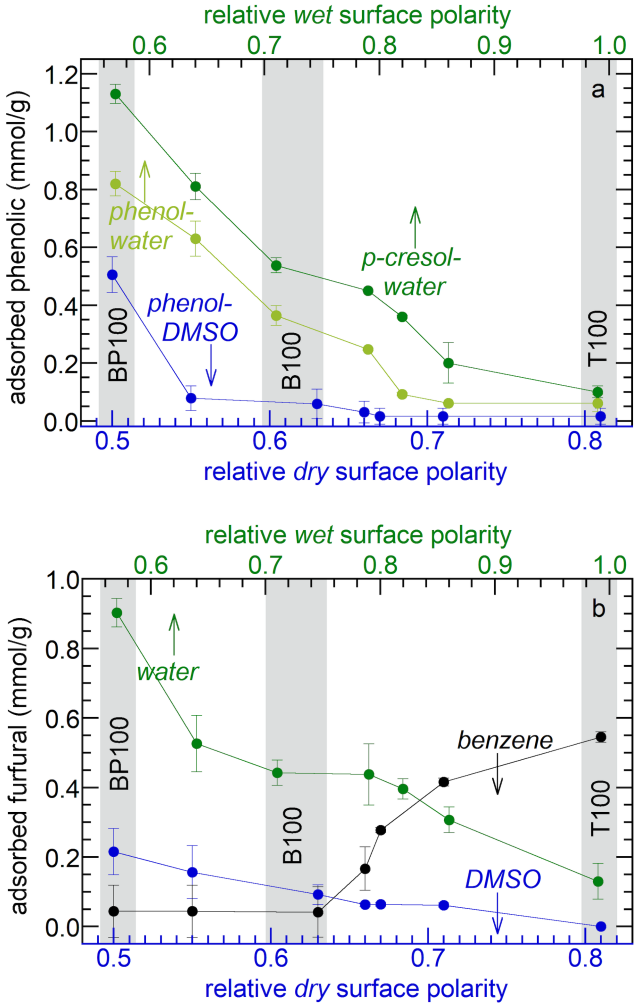

Fig. 2.7. Effect of PMO polarity on (a) amounts of phenol or *p*-cresol adsorbed from 40 mM solutions in water and DMSO; and (b) amounts of furfural adsorbed from 40 mM solutions in various solvents. Each experiment combined 20 mg PMO with 1.5 mL solution at 296 K.

2.4.6 Effect of solvent polarity on molecular partitioning at the solid-liquid interface

The nature of the solvent modulates the effect of surface polarity on molecular adsorption. For example, the phenol affinities of all the PMOs are dramatically lower when DMSO is the solvent instead of water, Fig. 2.7a. Thus the amount of phenol adsorbed on B100 from a DMSO solution decreased by 87 %, compared to adsorption from an aqueous solution. Reasoning in terms of a Born-Haber cycle,[55] we first note that phenol-surface interactions do not depend on solvent choice. The dielectric constant of phenol (15) is closer to that of DMSO (44) than water (73, all at 40 °C)[57,58], suggesting a higher energy cost to disrupt DMSO-phenol interactions than water-phenol interactions. In addition, the energy cost for disrupting solvent interactions with B100 is higher for DMSO than for water. Finally, solvent-solvent interactions are stronger for water than for DMSO. All of these terms are expected to suppress adsorption of phenol from DMSO. Compared to B100, BP100 shows less suppression (38 %) of phenol adsorption upon changing the solvent from water to DMSO, presumably due to a stronger phenol-surface interaction.

The effect of solvent polarity was further explored by comparing the adsorption of furfural from water with adsorption from DMSO or benzene (with relative polarities of 0.44 and 0.11, respectively, relative to water). Similar to phenol and *p*-cresol, the furfural affinities of the PMOs in contact with the aqueous solution increase monotonically as the surface polarity decreases (Fig. 2.7b, Table A2.5). Similar behavior is observed in DMSO, although the absolute amounts of adsorbed furfural are much lower. Since the relative polarity of furfural measured by the solvatochromic dye method (0.43)[59] is very close to that of DMSO (0.44), the solute-solvent interactions are presumably strong. In addition, the competition for surface adsorption sites will favor the more abundant solvent molecules when adsorption enthalpies are similar. However, the trend is reversed when furfural is dissolved in benzene

(relative polarity 0.111): now, the furfural affinities of the PMOs decrease with increasing surface polarity. Since benzene interactions with the more polar surfaces are much weaker, furfural adsorption is favored. The opposing trends in Fig. 2.7b illustrate the need to combine appropriate choice of solvent with surface polarity modulation to tune molecular adsorption.

2.5 Conclusion

This study sets the stage for design of porous solid catalysts with controlled surface polarity, in conjunction with rational solvent choice, to improve activity and selectivity in liquid-phase reactions by promoting preferential adsorption of reactants and desorption of desired products. The relative surface polarities of periodic mesoporous organosilicas (PMOs) can be tuned over a wide range by varying the chemical composition, independent of the textural properties. The mobility of near-surface molecules and their affinity for the surface are correlated with surface polarity. Tethered nitroxides experience decreased mobility as the surface polarity decreases, reflecting their increasingly strong association with the surface. Moreover, adsorption of organic molecules such as phenol, p-cresol, and furfural from polar solvents become more favorable as the surface polarity decreases. However, the effect can be reversed by changing the solvent polarity: thus such molecules adsorb less favorably from benzene as the surface polarity decreases. When the polarity of the solvent and solute are well-matched, adsorption is minimized. Thus, tuning the extent of adsorption precisely can be achieved by appropriate choices of solvent, surface polarity, and solute polarity. This systematic study demonstrates how readily achieved variations in the surface polarity of PMO-based materials results in significant changes in adsorption equilibria for classes of molecules relevant to important catalytic reactions. While the consequences of surface and

solvent polarity on adsorption are as expected, their rational prediction and ease of modulation suggests ways to design improved catalytic processes. Further refinements should include consideration of specific solute binding modes, such as cation–p interactions, electrostatic interactions, and H-bonding. Work is underway to include modification of PMO materials with active sites such as Brønsted/Lewis acid sites and metal nanoparticles, in order to assess polarity effects on heterogeneous reactivity.

2.6 References

(1) Manayil, J.; Lee, A.; Wilson, K. Functionalized Periodic Mesoporous Organosilicas: Tunable Hydrophobic Solid Acids for Biomass Conversion. *Molecules* **2019**, *24*, 239.

(2) Liu, F.; Huang, K.; Zheng, A.; Xiao, F.-S.; Dai, S. Hydrophobic Solid Acids and Their Catalytic Applications in Green and Sustainable Chemistry. *ACS Catal.* **2018**, *8*, 372–391.

(3) Sievers, C.; Noda, Y.; Qi, L.; Albuquerque, E. M.; Rioux, R. M.; Scott, S. L. Phenomena Affecting Catalytic Reactions at Solid–Liquid Interfaces. *ACS Catal.* **2016**, *6*, 8286–8307.

(4) Hu, X.; Wang, S.; Westerhof, R. J. M.; Wu, L.; Song, Y.; Dong, D.; Li, C.-Z. Acid-Catalyzed Conversion of C6 Sugar Monomer/Oligomers to Levulinic Acid in Water, Tetrahydrofuran and Toluene: Importance of the Solvent Polarity. *Fuel* **2015**, *141*, 56–63.

(5) Mellmer, M. A.; Sener, C.; Gallo, J. M. R.; Luterbacher, J. S.; Alonso, D. M.; Dumesic, J. A. Solvent Effects in Acid-Catalyzed Biomass Conversion Reactions. *Angew. Chem. Int. Ed.* **2014**, *53*, 11872–11875.

(6) Gilkey, M. J.; Xu, B. Heterogeneous Catalytic Transfer Hydrogenation as an Effective Pathway in Biomass Upgrading. *ACS Catal.* **2016**, *6*, 1420–1436.

(7) Wang, C.; Liu, Z.; Wang, L.; Dong, X.; Zhang, J.; Wang, G.; Han, S.; Meng, X.; Zheng, A.; Xiao, F.-S. Importance of Zeolite Wettability for Selective Hydrogenation of Furfural over Pd@Zeolite Catalysts. *ACS Catal.* **2018**, *8*, 474–481.

(8) Jin, Z.; Wang, L.; Hu, Q.; Zhang, L.; Xu, S.; Dong, X.; Gao, X.; Ma, R.; Meng, X.; Xiao, F.-S. Hydrophobic Zeolite Containing Titania Particles as Wettability-Selective Catalyst for Formaldehyde Removal. *ACS Catalysis* **2018**, 5250–5254.

(9) Otomo, R.; Yokoi, T.; Tatsumi, T. General Synthesis of Isosorbide from Sorbitol in Water over High-Silica Aluminosilicate Zeolites. *Appl. Catal., A* **2015**, *505*, 28–35.

(10) Li, L.; Yoshinaga, Y.; Okuhara, T. Water-Tolerant Catalysis by Mo–Zr Mixed Oxides Calcined at High Temperatures. *Phys. Chem. Chem. Phys.* **1999**, *1*, 4913–4918.

(11) Singappuli-Arachchige, D.; Kobayashi, T.; Wang, Z.; Burkhow, S. J.; Smith, E. A.; Pruski, M.; Slowing, I. I. Interfacial Control of Catalytic Activity in the Aldol Condensation: Combining the Effects of Hydrophobic Environments and Water. *ACS Catal.* **2019**, *9*, 5574–5582.

(12) Manayil, J. C.; dos Santos, V. C.; Jentoft, F. C.; Granollers Mesa, M.; Lee, A. F.; Wilson, K. Octyl Co-Grafted $PrSO_3H$/SBA-15: Tunable Hydrophobic Solid Acid Catalysts for Acetic Acid Esterification. *ChemCatChem* **2017**, *9*, 2231–2238.

(13) Singappuli-Arachchige, D.; Manzano, J. S.; Sherman, L. M.; Slowing, I. I. Polarity Control at Interfaces: Quantifying Pseudo-Solvent Effects in Nano-Confined Systems. *ChemPhysChem* **2016**, *17*, 2982–2986.

(14) Karimi, B.; Mirzaei, H. M. The Influence of Hydrophobic/Hydrophilic Balance of the Mesoporous Solid Acid Catalysts in the Selective Dehydration of Fructose into HMF. *RSC Adv.* **2013**, *3*, 20655.

(15) Karimi, B.; Mirzaei, H. M.; Behzadnia, H.; Vali, H. Novel Ordered Mesoporous Carbon Based Sulfonic Acid as an Efficient Catalyst in the Selective Dehydration of Fructose into 5-HMF: The Role of Solvent and Surface Chemistry. *ACS Appl. Mater. Interfaces* **2015**, *7*, 19050–19059.

(16) Pirez, C.; Lee, A. F.; Jones, C.; Wilson, K. Can Surface Energy Measurements Predict the Impact of Catalyst Hydrophobicity upon Fatty Acid Esterification over Sulfonic Acid Functionalised Periodic Mesoporous Organosilicas? *Catal. Today* **2014**, *234*, 167–173.

(17) Liu, J.; Yang, J.; Li, C.; Yang, Q. Catalytic Applications of Sulfonic Acid Functionalized Mesoporous Organosilicas with Different Fraction of Organic Groups in the Pore Wall. *J. Porous Mater.* **2009**, *16*, 273–281.

(18) Yang, Y.; Sayari, A. Mesoporous Organosilicates from Multiple Precursors: Co-Condensation or Phase Segregation/Separation? *Chem. Mater.* **2008**, *20*, 2980–2984.

(19) Bradley, R. H.; Rand, B. The Adsorption of Vapours by Activated and Heat-Treated Microporous Carbons. Part 2. Assessment of Surface Polarity Using Water Adsorption. *Carbon* **1993**, *31*, 269–272.

(20) Mietner, J. B.; Brieler, F. J.; Lee, Y. J.; Fröba, M. Properties of Water Confined in Periodic Mesoporous Organosilicas: Nanoimprinting the Local Structure. *Angew. Chem. Int. Ed.* **2017**, *56*, 12348–12351.

(21) Jahnke, J. P.; Idso, M. N.; Hussain, S.; Junk, M. J. N.; Fisher, J. M.; Phan, D. D.; Han, S.; Chmelka, B. F. Functionally Active Membrane Proteins Incorporated in Mesostructured Silica Films. *J. Am. Chem. Soc.* **2018**, *140*, 3892–3906.

(22) Bordignon, E.; Brutlach, H.; Urban, L.; Hideg, K.; Savitsky, A.; Schnegg, A.; Gast, P.; Engelhard, M.; Groenen, E. J. J.; Möbius, K.; Steinhoff, H.-J. Heterogeneity in the Nitroxide

Micro-Environment: Polarity and Proticity Effects in Spin-Labeled Proteins Studied by Multi-Frequency EPR. *Appl. Magn. Reson.* **2010**, *37*, 391–403.

(23) Zhao, D.; Feng, J.; Huo, Q.; Melosh, N.; Fredrickson, G. H.; Chmelka, B. F.; Stucky, G. D. Triblock Copolymer Syntheses of Mesoporous Silica with Periodic 50 to 300 Angstrom Pores. *Science* **1998**, *279*, 548–552.

(24) Goto, Y.; Inagaki, S. Synthesis of Large-Pore Phenylene-Bridged Mesoporous Organosilica Using Triblock Copolymer Surfactant. *ChemComm* **2002**, No. 20, 2410–2411.

(25) Brinker, C. J. Hydrolysis and Condensation of Silicates: Effects on Structure. *J. Non-Cryst. Solids* **1988**, *100*, 31–50.

(26) Bao, X. Y.; Zhao, X. S.; Qiao, S. Z.; Bhatia, S. K. Comparative Analysis of Structural and Morphological Properties of Large-Pore Periodic Mesoporous Organosilicas and Pure Silicas. *J. Phys. Chem. B* **2004**, *108*, 16441–16450.

(27) Bao, X. Y.; Zhao, X. S.; Li, X.; Chia, P. A.; Li, J. A Novel Route toward the Synthesis of High-Quality Large-Pore Periodic Mesoporous Organosilicas. *J. Phys. Chem. B* **2004**, *108*, 4684–4689.

(28) Kleitz, F.; Solovyov, L. A.; Anilkumar, G. M.; Choi, S. H.; Ryoo, R. Transformation of Highly Ordered Large Pore Silica Mesophases (Fm3m, Im3m and P6mm) in a Ternary Triblock Copolymer–Butanol–Water System. *ChemComm* **2004**, No. 13, 1536–1537.

(29) Kim, T.-W.; Kleitz, F.; Paul, B.; Ryoo, R. MCM-48-like Large Mesoporous Silicas with Tailored Pore Structure: Facile Synthesis Domain in a Ternary Triblock Copolymer−Butanol−Water System. *J. Am. Chem. Soc.* **2005**, *127*, 7601–7610.

(30) Yang, Y.; Sayari, A. Molecularly Ordered Biphenyl-Bridged Mesoporous Organosilica Prepared under Acidic Conditions. *Chem. Mater.* **2007**, *19*, 4117–4119.

(31) Jelinek, L.; sz. Kovats, E. True Surface Areas from Nitrogen Adsorption Experiments. *Langmuir* **1994**, *10*, 4225–4231.

(32) Rice, G. L.; Scott, S. L. Characterization of Silica-Supported Vanadium(V) Complexes Derived from Molecular Precursors and Their Ligand Exchange Reactions. *Langmuir* **1997**, *13*, 1545–1551.

(33) Reichardt, C.; Welton, T. *Solvents and Solvent Effects in Organic Chemistry*, 4th edn.; Wiley-VCH: Weinheim, 2011.

(34) Catalan, J.; Perez, P.; Laynez, J.; Blanco, F. G. Analysis of the Solvent Effect on the Photophysics Properties of 6-Propionyl-2-(Dimethylamino)Naphthalene (PRODAN). *J. Fluoresc.* **1991**, *1*, 215–223.

(35) Ortony, J. H.; Cheng, C.-Y.; Franck, J. M.; Kausik, R.; Pavlova, A.; Hunt, J.; Han, S. Probing the Hydration Water Diffusion of Macromolecular Surfaces and Interfaces. *New J. Phys.* **2011**, *13*, 015006.

(36) Schrader, A. M.; Monroe, J. I.; Sheil, R.; Dobbs, H. A.; Keller, T. J.; Li, Y.; Jain, S.; Shell, M. S.; Israelachvili, J. N.; Han, S. Surface Chemical Heterogeneity Modulates Silica Surface Hydration. *Proc. Natl. Acad. Sci. U. S. A.* **2018**, *115*, 2890–2895.

(37) Etienne, E.; Le Breton, N.; Martinho, M.; Mileo, E.; Belle, V. SimLabel: A Graphical User Interface to Simulate Continuous Wave EPR Spectra from Site-directed Spin Labeling Experiments. *Magn. Reson. Chem.* **2017**, *55*, 714–719.

(38) Stoll, S.; Schweiger, A. EasySpin, a Comprehensive Software Package for Spectral Simulation and Analysis in EPR. *J. Magn. Reson.* **2006**, *178*, 42–55.

(39) Cubo, A.; Iglesias, J.; Morales, G.; Melero, J. A.; Moreno, J.; Sánchez-Vázquez, R. Dehydration of Sorbitol to Isosorbide in Melted Phase with Propyl-Sulfonic Functionalized SBA-15: Influence of Catalyst Hydrophobization. *Appl. Catal., A* **2017**, *531*, 151–160.

(40) Hammes, K.; Smernik, R. J.; Skjemstad, J. O.; Schmidt, M. W. I. Characterisation and Evaluation of Reference Materials for Black Carbon Analysis Using Elemental Composition, Colour, BET Surface Area and 13C NMR Spectroscopy. *Appl. Geochem.* **2008**, *23*, 2113–2122.

(41) Zhuravlev, L. T. The Surface Chemistry of Amorphous Silica. Zhuravlev Model. *Colloids Surf., A* **2000**, *173*, 1–38.

(42) Ide, M.; El-Roz, M.; De Canck, E.; Vicente, A.; Planckaert, T.; Bogaerts, T.; Van Driessche, I.; Lynen, F.; Van Speybroeck, V.; Thybault-Starzyk, F.; Van Der Voort, P. Quantification of Silanol Sites for the Most Common Mesoporous Ordered Silicas and Organosilicas: Total versus Accessible Silanols. *Phys. Chem. Chem. Phys.* **2013**, *15*, 642–650.

(43) Gallas, J. P.; Goupil, J. M.; Vimont, A.; Lavalley, J. C.; Gil, B.; Gilson, J. P.; Miserque, O. Quantification of Water and Silanol Species on Various Silicas by Coupling IR Spectroscopy and In-Situ Thermogravimetry. *Langmuir* **2009**, *25*, 5825–5834.

(44) Giovambattista, N.; Debenedetti, P. G.; Rossky, P. J. Effect of Surface Polarity on Water Contact Angle and Interfacial Hydration Structure. *J. Phys. Chem. B* **2007**, *111*, 9581–9587.

(45) Lin, F.; Meng, X.; Mertens, M.; Cool, P.; Van Doorslaer, S. Probing Framework–Guest Interactions in Phenylene-Bridged Periodic Mesoporous Organosilica Using Spin-Probe EPR. *Phys. Chem. Chem. Phys.* **2014**, *16*, 22623–22631.

(46) Pivtsov, A.; Wessig, M.; Klovak, V.; Polarz, S.; Drescher, M. Localization of Guest Molecules in Nanopores by Pulsed EPR Spectroscopy. *J. Phys. Chem. C* **2018**, *122*, 5376–5384.

(47) Wessig, M.; Drescher, M.; Polarz, S. Probing Functional Group Specific Surface Interactions in Porous Solids Using ESR Spectroscopy as a Sensitive and Quantitative Tool. *J. Phys. Chem. C* **2013**, *117*, 2805–2816.

(48) Mason, R. P.; Polnaszek, C. F.; Freed, J. H. Interpretation of Electron Spin Resonance Spectra of Spin Labels Undergoing Very Anisotropic Rotational Reorientation. Comments. *J. Phys. Chem.* **1974**, *78*, 1324–1329.

(49) Stucki, J. W.; Banwart, W. L.; eds. *Advanced Chemical Methods for Soil and Clay Minerals Research: Proceedings of the NATO Advanced Study Institute Held at the University of Illinois, July 23–August 4, 1979*; Springer Science & Business Media.

(50) Biasi, R. S. de; Fernandes, A. A. R. The ESR Linewidth of Dilute Solid Solutions. *J. Phys. C: Solid State Phys.* **1983**, *16*, 5481–5489.

(51) Ottaviani, M. F.; Garcia-Garibay, M.; Turro, N. J. TEMPO Radicals as EPR Probes to Monitor the Adsorption of Different Species into X Zeolite. *Colloids Surf., A* **1993**, *72*, 321–332.

(52) Dzikovski, B.; Tipikin, D.; Livshits, V.; Earle, K.; Freed, J. Multifrequency ESR Study of Spin-Labeled Molecules in Inclusion Compounds with Cyclodextrins. *Phys. Chem. Chem. Phys.* **2009**, *11*, 6676–6688.

(53) Liu, Y. Is the Free Energy Change of Adsorption Correctly Calculated? *J. Chem. Eng. Data* **2009**, *54*, 1981–1985.

(54) Ocampo-Perez, R.; Leyva-Ramos, R.; Mendoza-Barron, J.; Guerrero-Coronado, R. M. Adsorption Rate of Phenol from Aqueous Solution onto Organobentonite: Surface Diffusion and Kinetic Models. *J. Colloid Interface Sci.* **2011**, *364*, 195–204.

(55) Singh, N.; Campbell, C. T. A Simple Bond-Additivity Model Explains Large Decreases in Heats of Adsorption in Solvents Versus Gas Phase: A Case Study with Phenol on Pt(111) in Water. *ACS Catal.* **2019**, *9*, 8116–8127.

(56) Keiluweit, M.; Kleber, M. Molecular-Level Interactions in Soils and Sediments: The Role of Aromatic π-Systems. *Environ. Sci. Technol.* **2009**, *43*, 3421–3429.

(57) Philip, J. C.; Haynes, D. CV.—The Dielectric Constants of Phenols and Their Ethers Dissolved in Benzene and m-Xylene. *J. Chem. Soc.Trans.* **1905**, *87*, 998–1003.

(58) Płowaś, I.; Świergiel, J.; Jadżyn, J. Relative Static Permittivity of Dimethyl Sulfoxide + Water Mixtures. *J. Chem. Eng. Data* **2013**, *58*, 1741–1746.

(59) Hoydonckx, H. E.; Van Rhijn, W.; De Vos, D. E.; Jacobs, P. A. Furfural and Derivatives. *Ullmann's Encyclopedia of Industrial Chemistry* **2007**, *16*, 285–313.

2.7 Appendix I

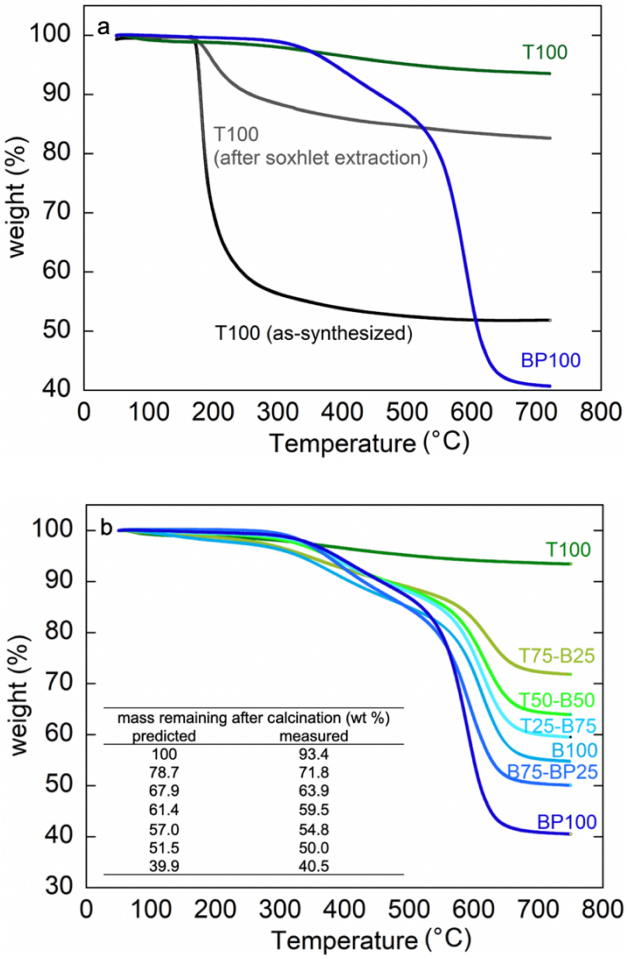

Fig. A2.1. (a) TGA of (a) as-synthesized T100, soxhlet-extracted T100, T100 and BP100 (after further calcination at 250 °C for 3 hours). (b) TGA of various PMOs after surfactant removal. All TGA data were recorded at a heating rate of 10 °C/min in air. The inset shows mass of each PMOs excluding phenylene and biphenylene bridging groups. Predicted mass was calculated on the basis of the formulas $x\mathrm{SiO_2}$ + $(1\text{-}x)\mathrm{O_{1.5}SiC_6H_4SiO_{1.5}}$ and $y\mathrm{O_{1.5}SiC_6H_4SiO_{1.5}}$ + $(1\text{-}y)\mathrm{O_{1.5}SiC_{12}H_8SiO_{1.5}}$, where x and y are mol% of TEOS and BTEB, respectively, in the synthesis mixture. Measured mass is based on apparent weight loss, measured by TGA in air.

Table A2.1. For each silane precursor,[a] amounts (mmol) used in the synthesis of various SBA-15-type materials

Material	TEOS	BTEB	TEOS/BTEB [b]	BTEBP	BTEB/BTEBP [c]
T100	30.0	-		-	
T75-B25	12.6	4.2	3	-	
T50-B50	5.8	5.8	1	-	
T25-B75	2.2	6.6	1/3	-	
B100	-	7.2		-	
B75-BP25	-	5.5		1.8	3
BP100	-	-		6.5	

[a] Tetraethyl orthosilicate (TEOS), 1,4-bis(triethoxysilyl)benzene (BTEB), 4,4′-bis(triethoxysilyl)-1,1′-biphenyl (BTEBP).

[b] With 3.0 g P123, the optimal amounts of silane to form the single-component materials are 30 mmol for TEOS, and 7.2 mmol for BTEB.[1,2] For the two-component materials, the amount of TEOS decreases gradually from 30 to 0 mmol, while the amount of BTEB increases gradually 0 to 7.2 mmol. The amounts of TEOS and BTEB for each SBA-15 type materials were chosen so that the TEOS/BTEB ratios are 3, 1, and 1/3.

[c] The amounts of BTEB and BTEBP used to synthesize B75-BP25 were determined in a similar fashion, based on the optimal amount of BTEBP needed.[3]

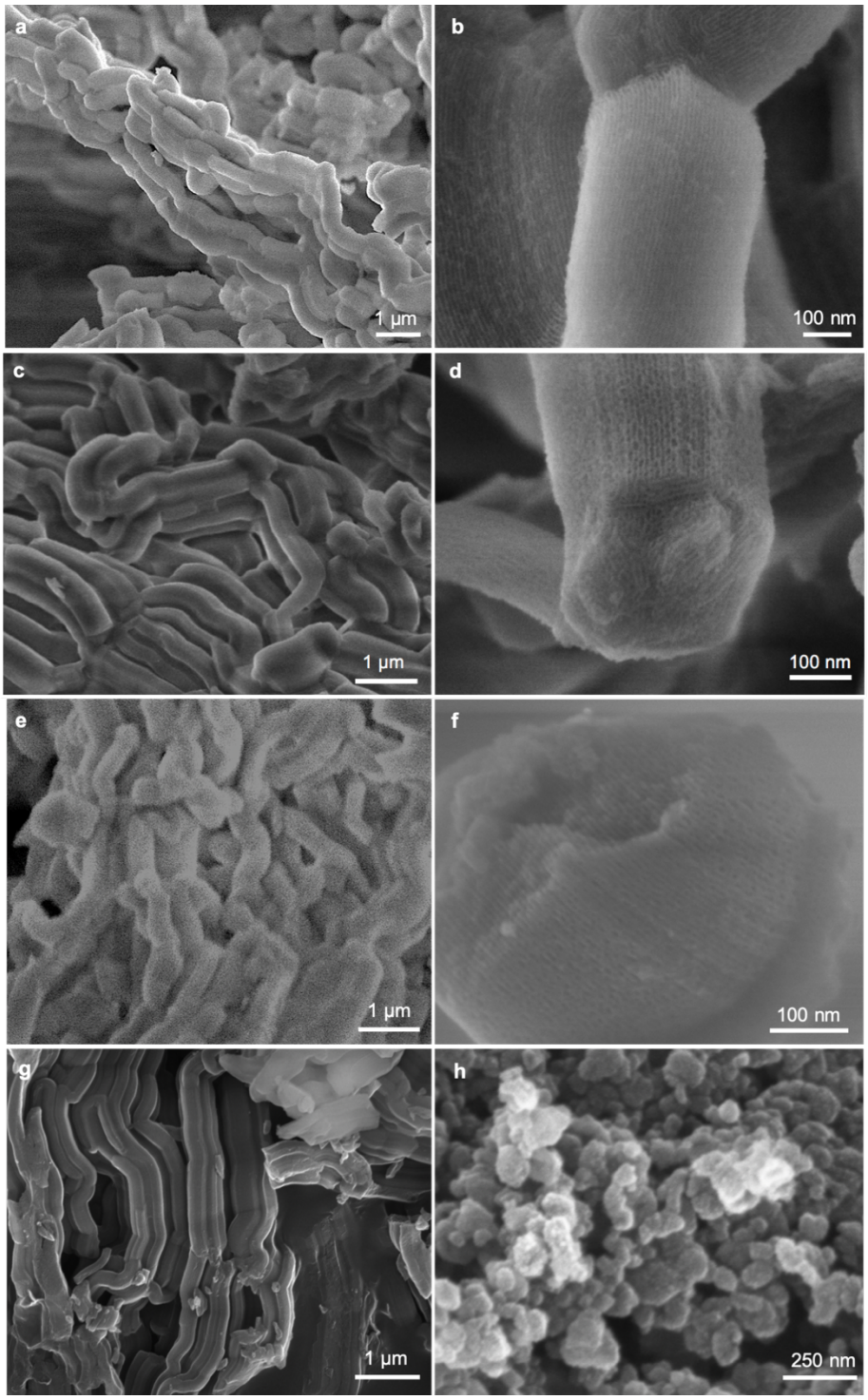

Fig. A2.2. SEM images of SBA-15-type materials: (a), (b) T100, (c), (d) T50-B50, (e), (f) B100, presented at two different magnifications (at the higher magnification, pore openings are visible); (g) B75-BP25; and (h) BP100.

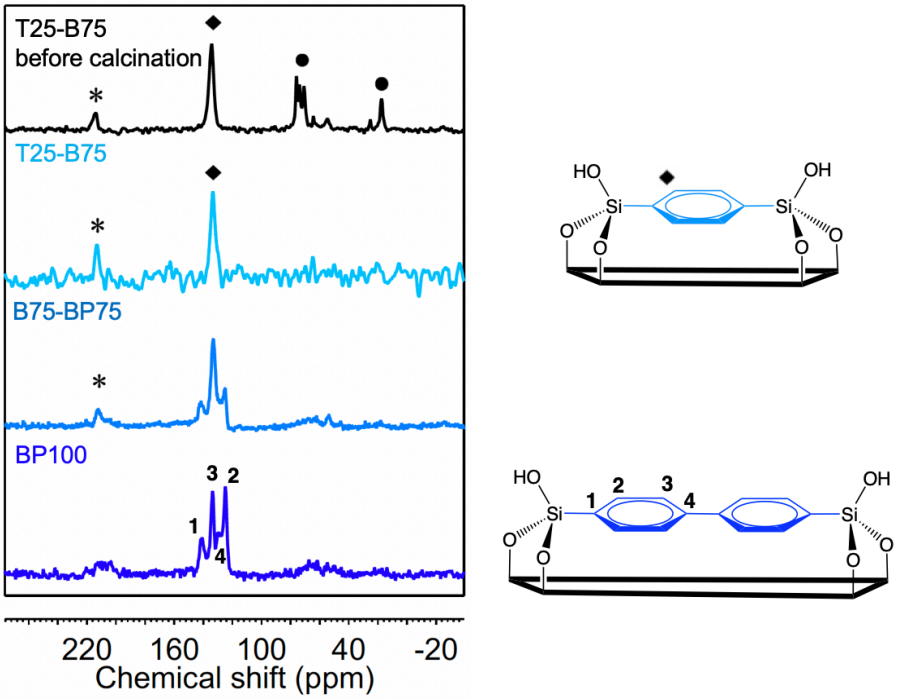

Fig. A2.3. ^{13}C CP/MAS NMR spectra of various SBA-15-type materials (10 kHz MAS; * indicates spinning side-bands). Signals at 17 and 70-76 ppm in the spectrum of T25-B75 correspond to residual P123 surfactant (●),[4] present even after 24 h Soxhlet extraction with ethanol. The signals disappear when the material is calcined in air at 250 °C for 3 h.[2] The remaining peak at 134 ppm corresponds to a single type of phenylene carbons.[5] Signals at 125, 129, 134, and 141 ppm in the spectrum of BP100 correspond to the four different biphenylene carbons.[3,5] Signals for both phenylene and biphenylene groups are observed in the spectrum of B75-BP25.

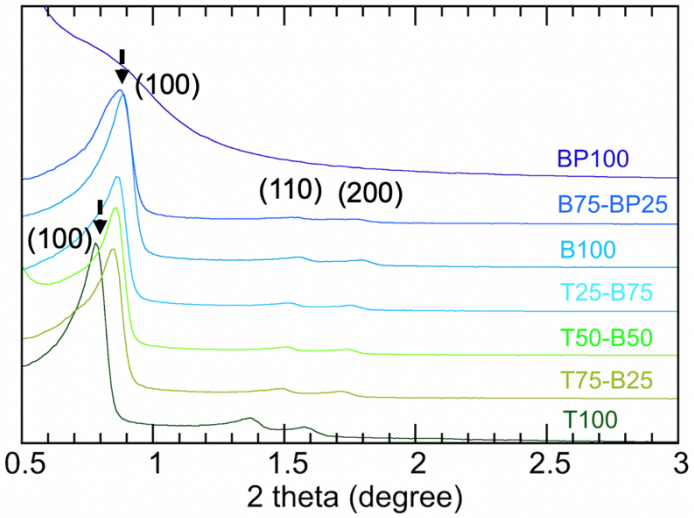

Fig. A2.4. Low-angle powder X-ray diffraction patterns of various SBA-15-type materials.

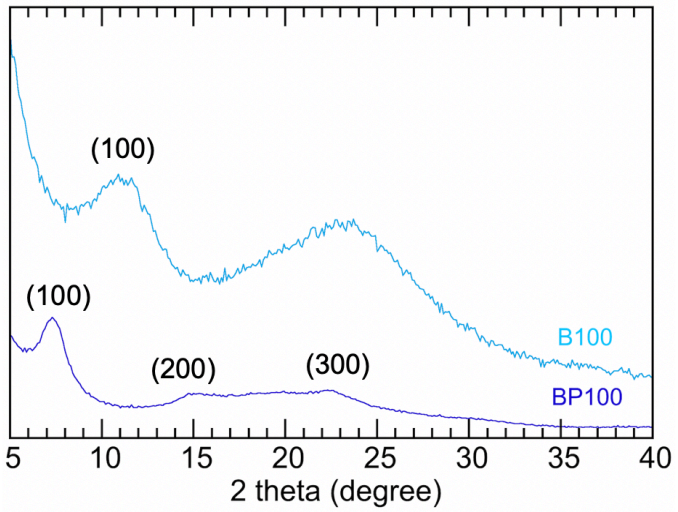

Fig. A2.5. Wide-angle powder XRD patterns for two SBA-15-type materials. All of the peaks are relatively broad, typical of mesoporous silicas synthesized using a non-ionic surfactant. The peak at $2\theta = 11$ ° for B100 corresponds to a *d*-spacing of 8.1 Å.[2] For BP100, peaks at $2\theta = 7.3$, 14.7, and 22.3 ° are assigned to a periodic biphenylene structure with a *d*-spacing of 11.9 Å, and its higher-order reflections (5.8 and 3.5 Å).[3,6]

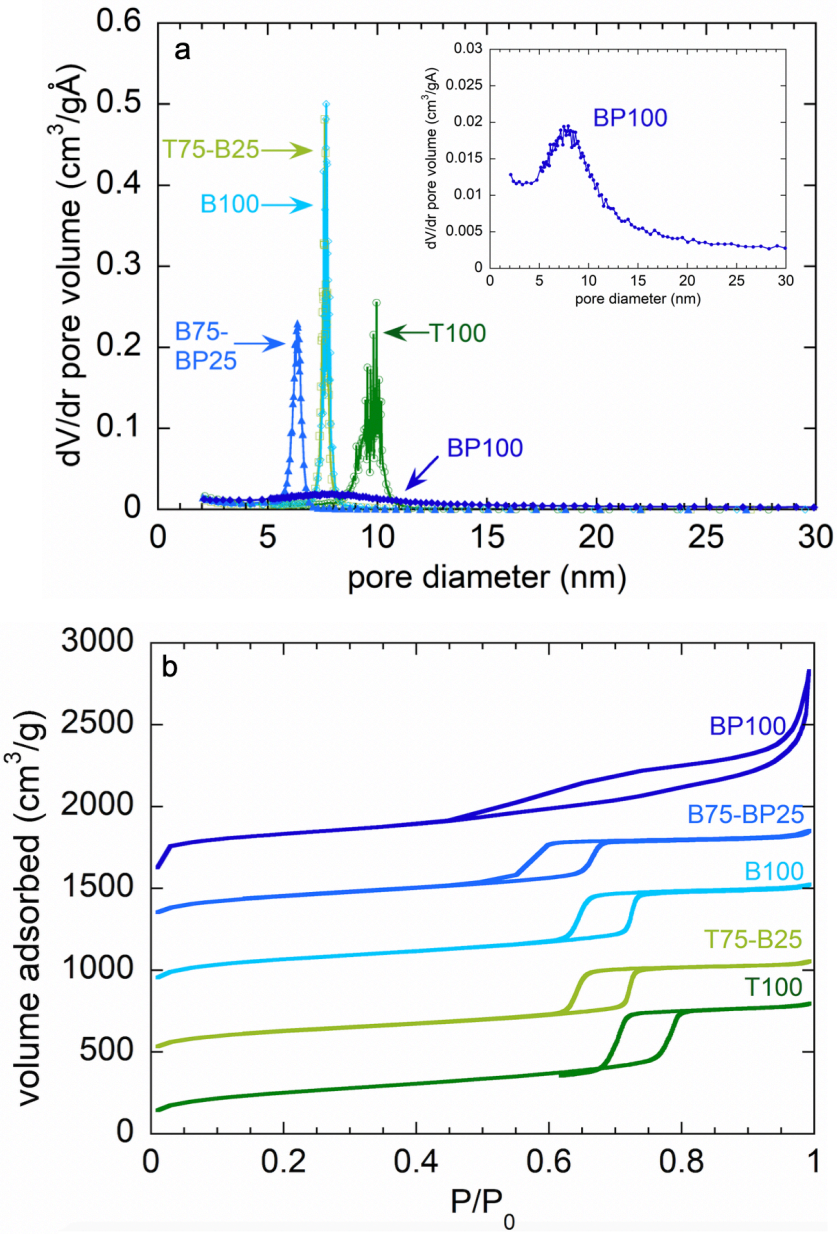

Fig. A2.6. (a) Pore size distributions for the selected PMOs. The inset shows the pore sizes of BP100, showing broader pore size distribution compared to that of other PMOs. (b) Nitrogen adsorption isotherms for the PMOs. Nitrogen adsorption analysis showed type IV isotherms typical of mesoporous materials. Interparticle porosity of BP100 resulted in the hysteresis loop extended to very high relative pressures.[3]

Table A2.2. Fluorescence maxima (nm) for Prodan adsorbed on various SBA-15-type powders, in both the dry state and suspended in water

Material	Peak position [a]	
	in water	dry
T100	526	509
T75-B25	512	499
T50-B50	510	494
T25-B75	507	493
B100	499	489
B75-BP25	490	480
BP100	482	473

[a] Measurement error in peak position is ± 1 nm.

Table A2.3. Relative polarities of various solvents, and their Prodan emission maxima (nm)

Solvent	Relative polarity [a]	λ_{max} [b]
water	1.000	527
methanol	0.762	502
ethanol	0.654	493
1-butanol	0.586	484
1-octanol	0.537	476
DMSO	0.444	465

[a] Inferred previously, by measuring the shift in the absorption spectrum of Reichardt's dye.[7,8]

[b] From a previous study.[9]

Table A2.4. Relative polarities of dry organosilica powders, and organosilicas suspended in water

Material	Relative *dry* surface polarity[a]	Relative *wet* surface polarity[a]
T100	0.81	0.99
T75-B25	0.71	0.86
T50-B50	0.67	0.82
T25-B75	0.66	0.79
B100	0.63	0.71
B75-BP25	0.55	0.64
BP100	0.50	0.57

[a] Relative polarity was interpolated using the maximum fluorescence wavelength of adsorbed using a calibration curve based on the emission of Prodan in various solvents (Table A2.3).

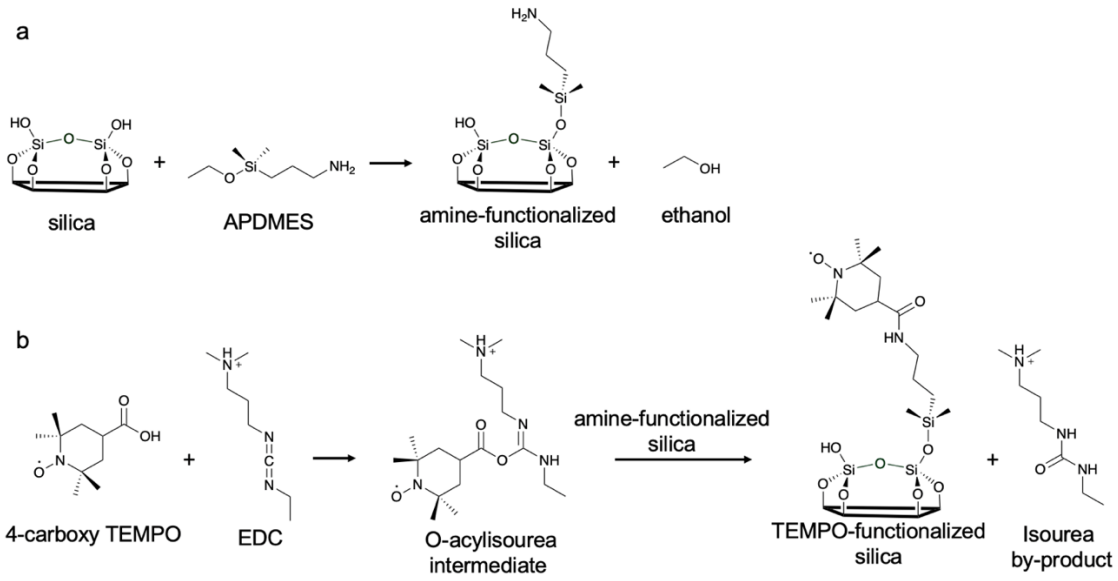

Scheme A2.1. Procedure for functionalization of (organo)silicas with 4-carboxy-TEMPO radicals. (a) The surface was modified with aminopropyl groups by grafting APDMES ((3-aminopropyl)-dimethylethoxysilane) from a pH 7 buffer solution. (b) The tethered amine was subsequently modified with 4-carboxy-TEMPO, using a solution of EDC (N-(3-dimethylaminopropyl)-N- ethylcarbodiimide hydrochloride) to catalyze the reaction.

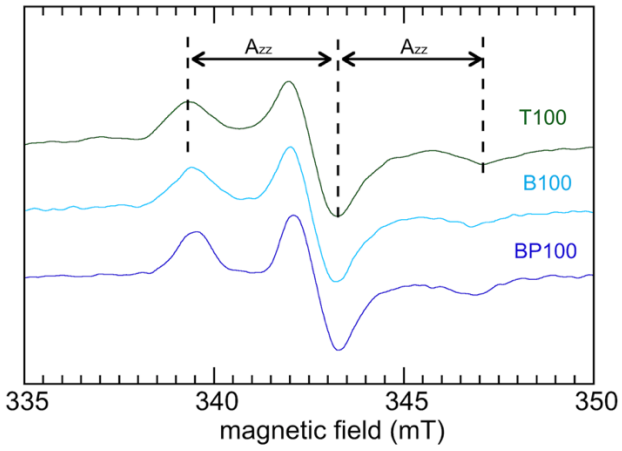

Fig. A2.7. Continuous-wave EPR spectra of 4-carboxy-TEMPO-functionalized SBA-15-type materials, suspended in a frozen water solution at 120 K. A_{zz} is defined as one-half the separation of the outer hyperfine extrema.[10]

Additional references

(1) Triblock Copolymer Syntheses of Mesoporous Silica with Periodic 50 to 300 Angstrom Pores. *Science* **1998**, *279*, 548–552.

(2) Goto, Y.; Inagaki, S. Synthesis of Large-Pore Phenylene-Bridged Mesoporous Organosilica Using Triblock Copolymer Surfactant. *Chem. Commun.* **2002**, No. 20, 2410–2411.

(3) Yang, Y.; Sayari, A. Molecularly Ordered Biphenyl-Bridged Mesoporous Organosilica Prepared under Acidic Conditions. *Chem. Mater.* **2007**, *19*, 4117–4119.

(4) Wang, Y.; Zibrowius, B.; Yang, C.; Spliethoff, B.; Schüth, F. Synthesis and Characterization of Large-Pore Vinyl-Functionalized Mesoporous Silica SBA-15. *Chem. Commun.* **2004**, No. 1, 46–47.

(5) Yang, Y.; Sayari, A. Mesoporous Organosilicates from Multiple Precursors: Co-Condensation or Phase Segregation/Separation? *Chem. Mater.* **2008**, *20*, 2980–2984.

(6) Kapoor, M. P.; Yang, Q.; Inagaki, S. Self-Assembly of Biphenylene-Bridged Hybrid Mesoporous Solid with Molecular-Scale Periodicity in the Pore Walls. *J. Am. Chem. Soc.* **2002**, *124*, 15176–15177.

(7) Reichardt, C.; Welton, T. *Solvents and Solvent Effects in Organic Chemistry*, 4th edn.; Wiley-VCH: Weinheim, 2011.

(8) Reichardt, C. Solvatochromic Dyes as Solvent Polarity Indicators. *Chem. Rev.* **1994**, *94*, 2319–2358.

(9) Catalan, J.; Perez, P.; Laynez, J.; Blanco, F. G. Analysis of the Solvent Effect on the Photophysics Properties of 6-Propionyl-2-(Dimethylamino)Naphthalene (PRODAN). *J. Fluoresc.* **1991**, *1*, 215–223.

(10) Stucki, J. W.; Banwart, W. L.; eds. *Advanced Chemical Methods for Soil and Clay Minerals Research: Proceedings of the NATO Advanced Study Institute Held at the University of Illinois, July 23–August 4, 1979*; Springer Science & Business Media.

Chapter 3. Entropic control of interfacial hydration in mesoporous organosilicas

3.1 Abstract

The structure and dynamics of interfacial water modulate the composition and behavior of adsorbates at functional surfaces in aqueous environments. Hydrophobic hydration is believed to store entropy at interfaces via the ordering of interfacial water, and thus contributes to its binding free energy. However, there is little experimental evidence for such entropic reservoirs, and virtually no precedent for their rational design at extended interfaces. In this study, the hydrophobicity of mesoporous silicas was modified in two distinct ways: (1) thermal dehydroxylation, via progressive condensation of surface silanols, and (2) incorporation of non-polar organic groups into the silica framework. Both approaches result in increasing hydrophobicity, manifested in the blue-shift of the fluorescence from an adsorbed solvatochromic dye. The weaker hydration of thermally treated inorganic silica surfaces with few silanols results in weaker water interactions and an abrupt increase in surface water diffusivity, measured by Overhauser dynamic nuclear polarization (ODNP) relaxometry. In contrast, the organosilicas show signatures of enhanced hydrophobic hydration: experimentally, they exhibit a monotonic decrease in surface water diffusivity; and computationally, molecular dynamics simulations of interfacial water reveal increased tetrahedrality, implying increased ordering, near an organosilica surface with nm-size organic domains, relative to the inorganic surface. These findings provide a long-sought validation of predictions that hydrophobic hydration at interfaces is controlled by the microscopic length scale of the hydrophobic regions. The insight further suggests that the hydration

thermodynamics of inorganic surfaces can be tuned to promote selective adsorption and, ultimately, reactivity.

3.2 Introduction

Interfacial hydration refers to the behavior of water molecules in the vicinity of an interface (typically, at distances ≤ 1 nm). It plays an important role in modulating interfacial solute dynamics and solute adsorption energies. Together, they influence the efficiencies of processes such as separations and catalysis that are mediated by sites located at soft and hard liquid interfaces. The surface hydrophobicity of proteins, polymers, and inorganic catalysts affects solute binding via mechanisms that remain poorly understood. For surfaces that are flat, extended, and uniform, hydrophobicity can be inferred from surface force or contact angle measurements. In the former, the repulsive force[1] or equilibrium interaction force[2] between two surfaces is correlated with hydrophobicity. In the latter, the receding contact angle (θ) of a water droplet reflects macroscopic hydrophobicity,[3] defined operationally as $\theta > 90$ °. However, the local hydrophobicity of real surfaces with geometric and chemical heterogeneity, such as is found in many porous materials, remains a challenge to evaluate. The fractal nature of such surfaces and their high curvature (both external and internal) make them intrinsically ill-suited for conventional macroscopic measurements, which furthermore cannot provide information at the molecular length scales that are relevant to adsorption and/or reaction.

From a fundamental point of view, a surface is locally hydrophobic when its Gibbs energy of hydration is positive, but $\Delta G_{hydration}$ is not readily measured. A definition of surface hydrophobicity that is more accessible involves the excess chemical potential, μ_{ex}, of an

adsorbed hydrophobic molecule.[4,5] The value of μ_{ex} can be determined from the equilibrium partitioning of the hydrophobe between the surface and the aqueous phase, eq 3.1.[6,7]

$$\mu^{ex} = -k_B T \ln \left[\frac{n^{local}/n_{H2O}^{local}}{n^{total}/n_{H2O}^{total}} \right] \quad (3.1)$$

Operationally, a surface is defined as hydrophobic if it has a negative value of μ_{ex}. Although the sign and magnitude of μ_{ex} are not readily measured at the nanometer scale, μ_{ex} can be computed from molecular dynamics simulations of model hydrophobes, such as methane molecules or Lennard-Jones particles. However, such studies still require a detailed knowledge of surface structure, which may not be available for real systems. Therefore, experimental methods to evaluate the thermodynamic properties of interfacial water, reflecting the local hydrophobicity of the surface, are needed to verify and benchmark the simulations.

The fluorescence from a solvatochromic dye molecule, such as Prodan, has been used an indirect probe of hydrophobicity. Its emission energy reflects the local polarity,[8,9] which is closely related to hydrophobicity.[10–12] In recent studies, the emission of adsorbed Prodan was used as an empirical measure of relative hydrophobicity in a series of mesoporous organosilicas.[13,14] Overhauser Dynamic Nuclear Polarization (ODNP) relaxometry provides another indirect measure of surface hydrophobicity, by quantifying the equilibrium dynamics of interfacial water. ODNP relies on cross-relaxation due to dipolar coupling between the ^{1}H nuclear spin of water molecules and the unpaired electron spin of a nearby radical (*aka* the spin label). At a magnetic field strength of 0.35 T, this coupling is effective for water molecules with correlation times for their motion relative to the spin label in the ps- to sub-

ns-range. By immobilizing the spin label at a surface, ODNP becomes sensitive to the translational motion of water molecules near that surface.[15,16] It has been used in this way to measure translational diffusivity for water molecules near proteins and other biomolecules labeled with paramagnetic spin probes.[6,17] The diffusivities correlate well with local surface hydrophobicities predicted by computed values of μ_{ex},[6] surface geometric topologies (as measured by local excluded volumes),[6] and solvation entropies.[17]

ODNP relaxometry measurements can also provide unique insight into the thermodynamic properties of interfacial hydration. A more hydrophobic surface may have a less negative Gibbs energy of hydration due to (1) a less negative hydration enthalpy (implying weaker binding of water to the surface), and/or (2) a more negative hydration entropy (due to greater ordering of the interfacial water, relative to the bulk).[18–21] Either effect can result in more favorable displacement of surface water by a hydrophobic solute and its binding to the more hydrophobic surface. However, water dynamics near hydrophobic surfaces should change in opposite ways in these limiting scenarios. When the value of $\Delta G_{hydration}$ is dominated by its enthalpic term, surface water motion becomes faster with increasing hydrophobicity, due to the lower enthalpic cost of dehydrating the surface to make space for solute adsorption. In contrast, slower surface water dynamics with increasing hydrophobicity indicate that the value of $\Delta G_{hydration}$ is dominated by its entropic term, since the liberation of more ordered surface water drives solute adsorption. A cross-over from enthalpically-driven to entropically-driven sorption is predicted to occur when the hydrophobic domain size decreases below ca. 1 nm.[20–22] Therefore trends in surface water diffusivity can reveal information about the length scale of the local hydrophobic domains.

This cross-over has been demonstrated experimentally, but only for highly idealized systems such as individual polymer chains of varying size.[23]

Amorphous silica is an important material used as an adsorbent for chemical separations, and as a support for heterogeneous catalysts. This study investigates variations in the hydration of amorphous silica surfaces with surface chemistry. Hydrophobicity was modified in two distinct ways: (1) by increasingly severe thermal treatment, which reduces the silanol/siloxane ratio on the silica surface,[2] and (2) by chemical incorporation of organic linkers with molecular dimensions (ca. 1 nm or less) into the silica framework.[13] Relative surface polarity was assessed via the fluorescence of adsorbed Prodan. Equilibrium surface water diffusivities were measured using ODNP relaxometry, and combined with molecular dynamics simulations to understand the enthalpic and entropic consequences of each type of surface modification.

3.3 Results

3.3.1 Systematic variation of silica hydrophobicity

Amorphous silicas with ordered mesoporosity (SBA-15-type) were modified to achieve gradually varying surface hydrophobicity. In one method, inorganic silica was subjected to thermal treatment. The silica was made by templated condensation of tetraethylorthosilicate (100 mol%, T100). SEM images show elongated fibers with diameters 0.3-0.6 μm and lengths 2-10 μm (Fig. A3.1). Calcination of T100 at 250 °C removes the templating surfactant. Silanol condensation requires higher temperatures, resulting in increased surface coverage by non-polar siloxane bonds (Scheme 3.1a).[24,25] Silicas subjected to this additional thermal treatment (up to 1000 °C under N_2 flow) are denoted by an appended

label indicating the temperature used for partial dehydroxylation. For example, T100-600 is an inorganic silica treated at 600 °C (note that the thermally treated silicas are reexposed to water in subsequent measurements, therefore they experience partial rehydroxylation). Upon heating, the B.E.T. surface area of the silica decreases gradually, from 709 m^2/g for T100 after calcination at 250 °C to 353 m^2/g for T100-1000 after thermal treatment at 1000 °C (Table A3.1). The nanoscale porosity is mostly maintained over this temperature range, as confirmed by small-angle X-ray diffraction (Fig. A3.2), although the average pore size decreases slightly, from 10 to 7 nm (Table A3.1 and Fig. A3.3).

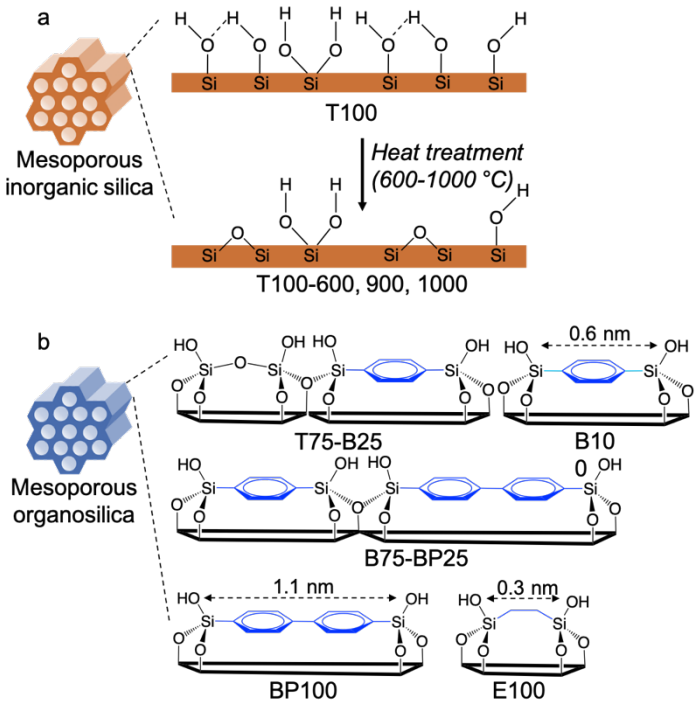

Scheme 3.1. Illustration of SBA-15-type silica materials used in this study, and their compositional variability: (a) mesoporous inorganic silica, with variable surface silanol

content achieved via thermal treatment, and (b) mesoporous organosilica, with variable framework linker composition.

In a second modification method, one or more organodisilanes (containing phenylene, biphenylene, or ethylene linkers) were incorporated into the framework of the ordered mesoporous silica during synthesis (Scheme 3.1b). Each organosilica is named according to the type of organodisilane precursor used (B: 1,4-bis(triethoxysilyl)benzene, BP: 4,4′-bis(triethoxysilyl)1-1′-biphenyl, E: 1,2-bis(trimethoxysilyl)ethane), and its proportion relative to the T precursor. For example, T75-B25 was synthesized by co-condensation of T (75 mol%) and B (25 mol%). In a recent study,[13] we showed that the fraction of phenylene and/or biphenylene linkers in the SBA-15 framework increases gradually without significantly altering the textural properties of the mesoporous silica, such as the B.E.T. surface area (ca. 700 m^2/g) and the pore size (5-10 nm), Table A3.1 and Fig. A3.2b. However, the biphenylene-bridged organosilica (BP100) has a significantly broader pore size distribution (±3.6 nm) compared to the other organosilicas (±0.8 nm or less).[13]

The surface silanol content of each silica was quantified by reaction with excess $VOCl_3$ vapor.[26] This method gives lower values than H/D exchange methods[27] or quantitative ^1H NMR analysis,[28] which also count sub-surface silanols that are inaccessible to $VOCl_3$. For example, the density of $VOCl_3$-accessible silanols on T100 is 1.8 nm^{-2} (Table 3.1), compared to ca. 5 nm^{-2} reported for various silica materials by H/D exchange.[27] The density of $VOCl_3$-accessible silanols decreases gradually with thermal treatment, to 0.1 nm^{-2} for T100-1000 (Table A3.2).

Table 3.1. Effect of thermal treatment and framework linkers on surface polarity and near-surface water dynamics in amorphous silicas

Silica [a]	Pore size (nm)	Thermal treatment (°C)	Silanol density [b] α_{OH} (nm^{-2})	Prodan emission [c] λ_{max} (nm)	Relative polarity [d]	$D_{surface}$ (10^{-10} m^2/s)
T100	9.7	-	1.8	508	0.80	10.0 ± 0.2
T100-600	8.8	600	1.2	504	0.76	9.4 ± 0.3
T100-900	7.9	900	0.9	499	0.71	12.6 ± 0.3
T100-1000	7.0	1000	0.5	493	0.66	13.7 ± 0.5
T75-B25	7.6	-	1.5	500	0.72	7.4 ± 0.2
B100	7.6	-	1.3	491	0.65	4.3 ± 0.5
B75-BP25	6.3	-	1.8	481	0.56	3.3 ± 0.2
E100	7.1	-	2.2	479	0.55	4.5 ± 0.5
BP100	5.0	-	1.6	475	0.52	2.4 ± 0.2
B100-350	6.0	400	1.0	483	0.58	8.6 ± 0.1

[a] All materials are ordered mesoporous silicas (SBA-15-type), made by condensing silanes in the presence of P123 as templating surfactant. Each material is named according to the type of silane precursor(s) used in its synthesis (T: tetraethylorthosilicate, B: 1,4-bis(triethoxysilyl)benzene, BP: 4,4′-bis(triethoxysilyl)1-1′-biphenyl, E: 1,2-bis(trimethoxysilyl)ethane), and their relative molar proportions. Each material was calcined at 250 °C to remove the templating surfactant, except for E100 (for which the surfactant was

removed by extraction in refluxing ethanol). The appended number indicates the temperature (in °C) of subsequent thermal treatment. [b] Silanol content was measured by $VOCl_3$ chemisorption, after evacuation to remove water at 170 °C and 0.1 mTorr for 7 h.[13,26] For silicas thermally treated after calcination, the silanol density was measured after immersion in water at room temperature for 3 d, resulting in partial rehydroxylation. Surface areas were obtained using the Brunauer-Emmett-Teller (B.E.T.) method, assuming the area occupied by an adsorbed N_2 molecule is 0.135 nm^2 (appropriate for perpendicular adsorption on oxide surfaces).[29] The generally accepted measurement error in B.E.T. surface areas, ± 10 %,[30] leads to an error in the silanol density of ca. 10 %. [c] Measurement error ±1 nm. [d] Relative polarity was interpolated using a calibration curve[31] based on the emission of Prodan in solvents of varying relative polarity (Table A3.3, Fig. A3.4).[32] The scale is anchored by assigning values of 0 and 1 to tetramethylmethylsilane and water, respectively.

Since the measurement of surface water dynamics by ODNP requires extended exposure of the silicas to water, silanol densities were measured after immersing each thermally treated T100 silica in water at room temperature for 3 d. Table A3.2 shows the changes (2-5× increase) in silanol density for the water-exposed silicas compared to the dry silicas. This partial rehydroxylation is expected,[33] and limits our ability to make measurements on silicas with very low surface hydroxyl densities, but the initial dehydroxylation process is not fully reversible.[34] Therefore the silanol content of the rehydrated T100 silicas still decreases smoothly, from 1.8 to 0.5 nm^{-2} with increasing thermal treatment temperature up to 1000 °C (Table 3.1).

The organosilicas containing phenylene and biphenylene linkers were not thermally treated, apart from the mild calcination required to remove the templating surfactant. Their silanol densities vary over a smaller range (1.8 - 1.3 nm^{-2}, Table 3.1), and lack a discernable trend. Ethylene-bridged silica (E100) has a slightly higher silanol density (2.2 nm^{-2}), due to the use of ethanol extraction rather than calcination to remove the templating surfactant (necessitated by the limited thermal stability of E100).[35] Consequently, changes in surface hydrophobicity for the mesoporous organosilicas (with the possible exception of E100) should be associated mainly with the nature and abundance of the organic linkers, rather than variations in their surface silanol content.

3.3.2 Relative polarities of silica surfaces

Changes in surface polarity (correlated with hydrophobicity) for the T100 series of thermally treated silicas were assessed by adsorbing Prodan from aqueous solution. To mimic the conditions required for subsequent ODNP measurement of surface water dynamics (see below), each thermally-treated silica was first immersed in water for 3 d, then Prodan was adsorbed from aqueous solution. Fluorescence spectra for the inorganic silica powders are compared in Fig. 3.1a. Their λ_{max} values decrease monotonically from 508 to 493 nm as the thermal treatment temperature increases up to 1000 °C. Thus, λ_{max} is correlated with silanol density (Table 3.1, Fig. A3.5).

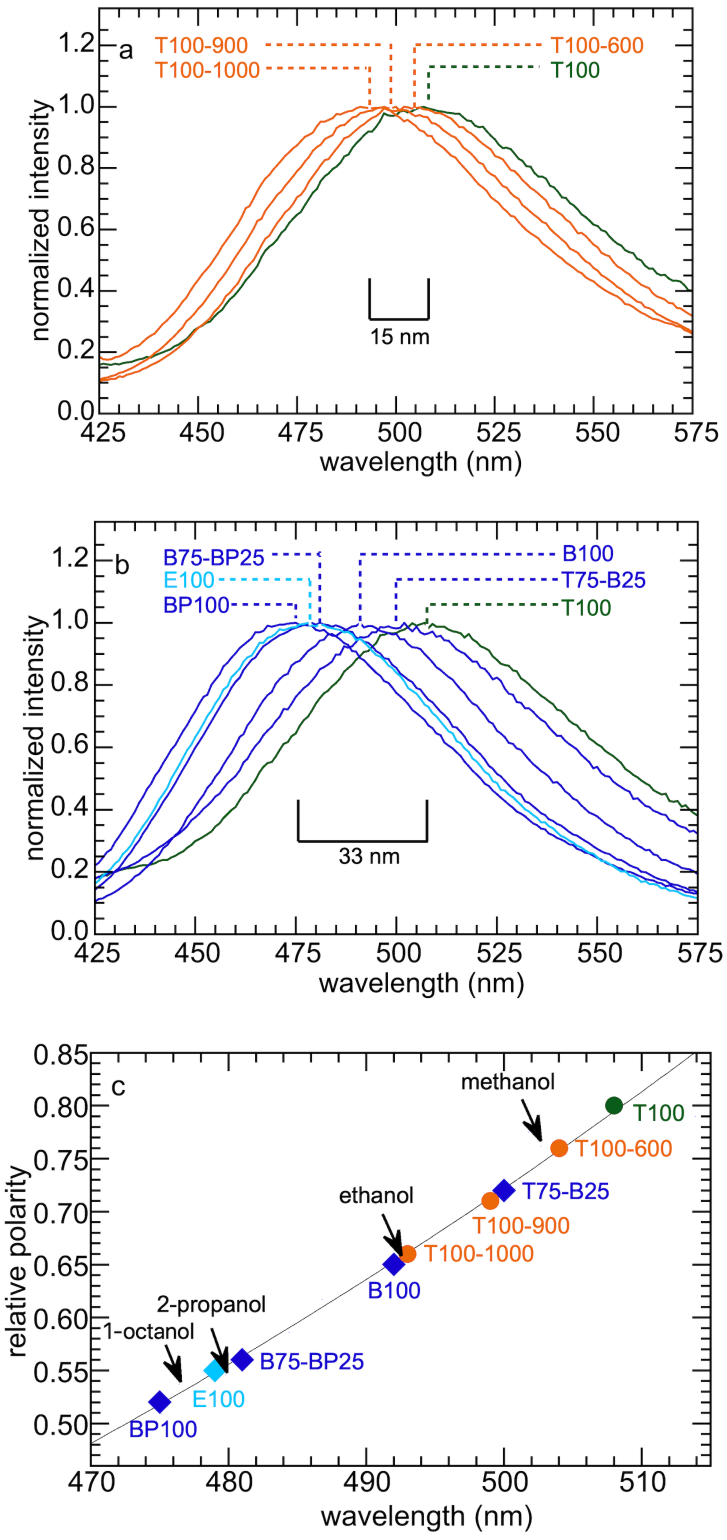

Fig. 3.1. Comparison of fluorescence spectra for Prodan adsorbed on T100 (green) with (a) mesoporous inorganic silica (T100) after various thermal treatments (orange circles), and (b)

various mesoporous organosilicas (not thermally treated, except as necessary for surfactant removal, blue diamonds). For the inorganic silicas, the appended number T100-X represents the thermal treatment temperature. In each case, spectra were recorded for dry silica powders. (c) Correlation between Prodan fluorescence emission maximum and relative solvent/surface polarity, for mesoporous inorganic silica frameworks containing only oxygen linkers (●), or a combination of oxygen and organic linkers (◆). Several solvent values are shown for comparison (arrows~~hollow symbols~~).

Fluorescence spectra for Prodan adsorbed on each organosilica are compared in Fig. 3.1b. Their λ_{max} values decrease monotonically as the fraction and size of the organic linkers incorporated into the framework increases. Notably, the presence of these organic linkers has a larger effect on surface polarity than silanol density, as evidenced by the much more significant blueshift (33 nm) of λ_{max} across the range of organosilicas (compared to just 15 nm for T100 after various thermal treatments).

Relative surface polarity values for each type of silica were obtained by comparison to calibrated λ_{max} values (obtained by interpolating values measured in various solvents of known polarity, ranging from 1.000 for water and 0.444 for dimethylsulfoxide, Table A3.3, Fig. A3.4).[31,32] The results are shown for both inorganic silicas and organosilicas in Fig. 3.1c. The relative surface polarities of the inorganic silicas with variable silanol contents range from 0.80 to 0.66. T100 without thermal treatment is slightly more polar than methanol, while heating to 1000 °C followed by partial rehydroxylation results in a relative surface polarity similar to ethanol. In the organosilica series, the relative polarities vary down to 0.52. The polarities of B100 and E100 are similar to ethanol and 2-propanol, respectively, while the

least polar material, BP100, is slightly less polar than 1-octanol. For organosilicas containing mixtures of linkers, such as B75-BP25 and T75-B25, intermediate values of λ_{max} were recorded. Thus gradually increasing the fraction of organic linkers results in intermediate surface polarities (Fig. A3.6a), similar to increasing the carbon chain length in aliphatic alcohols and ketones (Fig. A3.6b).[32] This result implies a uniform spatial distribution of the organic linkers, without segregation into organic-rich domains.

3.3.3 Probing the dynamics of interfacial water

The mobility of near-surface water provides insight into the thermodynamics of interfacial hydration. ODNP relaxometry is sensitive to water motion that occurs near a spin label, such as a stable nitroxide radical. It relies on the measurement of cross-relaxivity (k_σ), i.e., the relaxation rate of the ^{1}H nuclear spin of water, which is enhanced due to dipolar coupling to the unpaired electron spin (e) of the spin label.[15,16] ^{1}H-e cross-relaxation is efficient for water located within 1 nm of the spin label, and move with a correlation time less than or equal to the inverse electron spin Larmor frequency (9.8 GHz at 0.35 T).[15,16] The magnitude of k_σ is directly proportional to the rate of water diffusion near the spin label.[6]

Near an interface, molecules experience slower diffusion due to the geometric effect,[36,37] as well as their chemical interactions with the surface.[2,38] Since the geometric effect is expected to be similar for all mesoporous materials studied here, major differences in water diffusivity can be attributed to chemical interactions. By attaching the spin label to the surface, we ensure that the cross-relaxivity ($k_{\sigma,surface}$) reports only on the diffusivity of water less than ca. 2 nm from the surface (Scheme 3.2). In this study, 4-carboxy-TEMPO radicals were attached to silica via propylamine linkers, and the surface diffusivity $D_{surface}$ was obtained

from $k_{\sigma,surface}$. Although $D_{surface}$ values cannot be directly compared to bulk diffusivities measured by other techniques, $D_{surface}$ should correlate with surface water diffusivity.

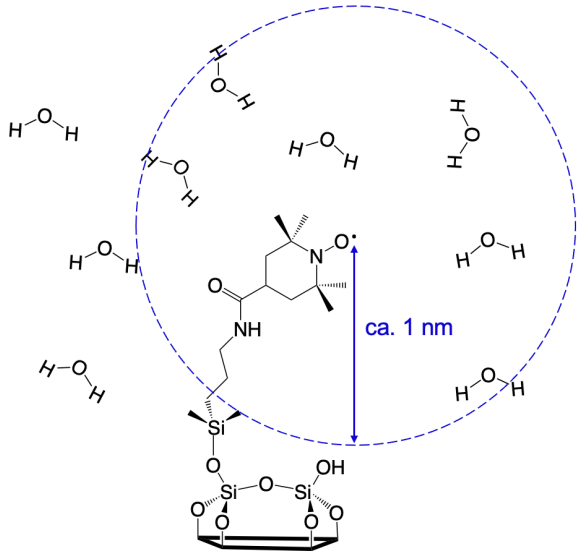

Scheme 3.2. A 4-carboxy-TEMPO radical, attached to a silica surface via a propylamine tether, acts as a spin probe for ODNP relaxometry, which measures water dynamics within ca. 1 nm of the radical, and therefore within ca. 2 nm of the interface.

3.3.4 Effect of surface silanol density on water mobility

Since water interacts with surface silanols via hydrogen-bonding, we expect its diffusivity to vary inversely with the surface silanol density. $D_{surface}$ values measured for each of the thermally treated T100 silicas are shown in Table 3.1 and Fig. 3.2. As expected, the value of $D_{surface}$ increases, from $(10.0 \pm 0.2) \times 10^{-10}$ m^2/s for T100 without thermal treatment to $(13.7 \pm 0.5) \times 10^{-10}$ m^2/s for T100-1000. Since this change is due to loss of hydrogen-bonding between water and surface silanols, hydration of inorganic silica surfaces is driven

principally by enthalpic stabilization associated with hydrogen bonding. Curiously, the change is not gradual: there is no increase in surface water diffusivity when T100 is treated at 600 °C, but the diffusivity rises abruptly when T100 is treated at 900 °C. These findings suggest a non-uniform distribution of surface silanols and the presence of silanol-free hydrophobic domains (see discussion below).

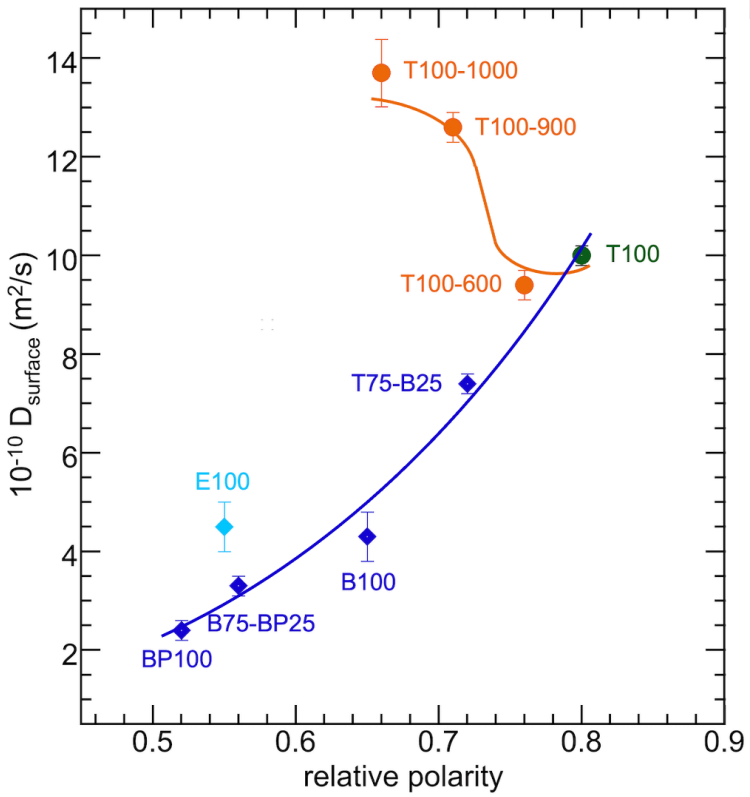

Fig. 3.2. Diffusivity of near-surface water ($D_{surface}$, derived from k_σ as measured by ODNP relaxometry) in mesoporous silicas containing only oxygen linkers (●), or a combination of oxygen and organic linkers (◆), as a function of the relative surface polarity (obtained by measuring the fluorescence of adsorbed Prodan, Fig. 3.1c). The solid lines are present only to guide the eye.

3.3.5 Effect of organic linkers on water diffusivity

The behavior of mesoporous organosilicas is very different to that of the thermally treated inorganic silicas. Fig. 3.2 shows their water diffusivity as a function of their relative surface polarity (blue diamonds). There is no obvious dependence of $D_{surface}$ on the silanol density (Fig. A3.7b), which varies little among the organosilicas. However, in contrast to the inverse correlation of surface water diffusivity with polarity for the inorganic silicas, $D_{surface}$ is *positively* correlated with surface polarity for the organosilicas. Thus the value of $D_{surface}$ for B100, $(4.3 \pm 0.5) \times 10^{-10}$ m^2/s, is half that of T100; the value for BP100, $(2.4 \pm 0.2) \times 10^{-10}$ m^2/s, is half that of B100. Since water molecules interact weakly with aromatic linkers, the variable hydration of the organosilica surfaces must be driven not by enthalpic but rather by entropic contributions (see below).

For ethylene-bridged E100, $D_{surface}$ is higher than expected based on its polarity. Since $D_{surface}$ did not change appreciably in the inorganic silica series as long as the silanol density was above the threshold value (see above), the slightly higher silanol density of E100 should not be responsible for its anomalous $D_{surface}$ value. Instead, we infer that the smaller ethylene linkers are less effective than aromatic linkers in inducing low entropy surface hydration.

Finally, reducing the pore sizes of B100 and E100 from ca. 7 nm to ca. 4 nm (Fig. A3.8) resulted in small decreases in surface water diffusivity (ca. 12 and 24 %, respectively, Fig. A3.9), suggesting that mesopore confinement effects are minor.

3.3.6 Contribution of silanols to water mobility near organosilica surfaces

The slower diffusion of interfacial water in the organosilicas relative to the inorganic silicas suggests that water molecules at the water-silica interface become more ordered as

hydrophobicity increases, resulting in a loss of entropy. Ordering may arise when water molecules that do not interact directly with the organic linkers form a hydrogen-bonded bridge or dome over the organic moieties, anchored at adjacent silanols (Scheme 3.3a). If some of these silanols are removed by thermal condensation, the mobility of the near-surface water should increase due to the decrease in water ordering (illustrated by the dotted red oval in Scheme 3.3b).

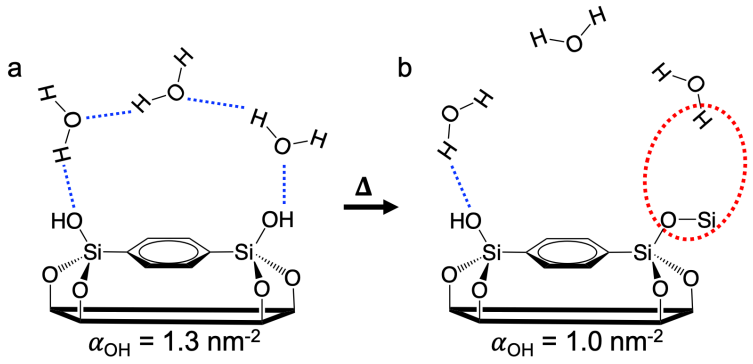

Scheme 3.3 (a) ordered water structure at an organosilica surface. The blue dotted lines represent hydrogen bonds. (b) reduction in ordering upon partial dehydroxylation of the organosilica. The red dotted oval highlights the loss of a hydrogen bond anchoring the water chain via a surface silanol.

To test this hypothesis, B100 was treated thermally at 350 °C, resulting in a reduction its surface silanol density from 1.3 to 1.0 nm^{-2} (Table 3.1). The Prodan fluorescence showed the expected blue-shift from 491 to 483 nm (Fig. A3.10). The lower polarity of B100-350 is similar to those of B75-BP25 and E100, however, the surface water diffusivity of B100-350 is significantly higher than either B75-BP25 or E100, and double that of B100 prior to thermal treatment (Table 3.1). Thus, it does departs significantly from the trend of decreasing water

diffusivity with increasing polarity observed for the organosilica series, reverting instead to the "normal" behavior of inorganic silica (i.e., water diffusivity *increases* with decreasing polarity). This result suggests that fewer silanols limit the effect of the organic linkers on water ordering. We note that, while a lower silanol density should also reduce the enthalpic contribution to surface hydration, $D_{surface}$ is not very sensitive to silanol density above a threshold value of ca. 1 nm^{-2}. Both B100 and B100-350 have silanol densities at or above this value (Table 3.1).

3.3.7 Simulation of water dynamics

The experimental evidence described above suggests that slower water diffusion near organosilica surfaces, relative to inorganic silica surfaces, arises from increased ordering of water molecules in the hydration layer. To test this hypothesis, molecular dynamics simulations of water near a hydroxylated amorphous silica slab were conducted, in the presence and absence of adsorbed benzene molecules (Fig. 3.3). The cut-offs for defining the hydration layer were chosen to include approximately two hydration layers, based on the density profiles in Fig. A3.11. The surface density of silanol groups was adjusted to 1.5 nm^{-2}, similar to the experimental values. The benzene molecules were placed on the surface to avoid blocking water-silanol interactions, and spaced approximately 1 nm apart. This distance is slightly longer than the expected spacing between phenylene groups of B100 (0.5-0.8 nm).[39] The simplified surface differs from the phenylene-bridged organosilica in that benzene is adsorbed rather than being incorporated into the silica framework, and is present only at the surface rather than being distributed throughout the material. Nevertheless, the model should provide qualitative insight into water dynamics near the experimental surface.

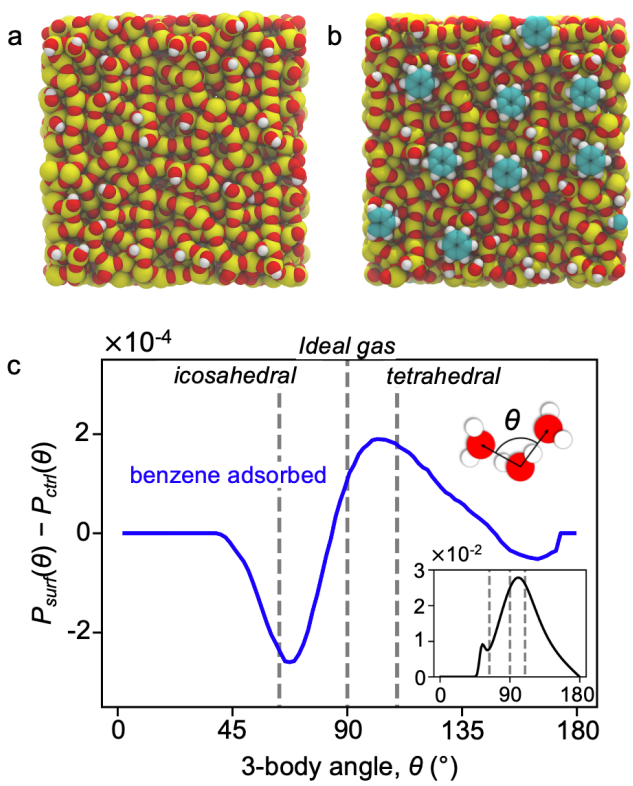

Fig. 3.3. Snapshots of an amorphous silica surface with its silanol density, α_{OH}, adjusted to approx. 1.5 nm^{-2}. Both snapshots were taken after the simulation, such that the surfaces are fully relaxed. Water molecules are removed in order to show the surface structure clearly. (a) The inorganic surface used as a control, and (b) the same surface, with adsorbed benzene molecules. (c) The probability distribution of three-body angles (θ) for water near the surface with adsorbed benzene, relative to the distribution for water near the surface without benzene (control). The inset depicts the distribution of three-body angles in the bulk, which is identical for both surfaces. Compared to the control, the surface with adsorbed benzene shows a clear increase in tetrahedral water structuring, and a corresponding decrease in icosahedral water structuring.

Water dynamics were assessed by computing the 2D diffusivity of water in the hydration layer for both silica surfaces. For the surface with adsorbed benzene, the average 2D diffusivity in its hydration layer is $(16.5 \pm 0.5) \times 10^{-10}$ m^2 s^{-1}, compared to $(20.0 \pm 0.4) \times 10^{-10}$ m^2 s^{-1} for the control surface without benzene. This finding is consistent with the experimental observation of slower water dynamics near organosilica surfaces.

Water structure and ordering in the hydration layers of both silica surfaces were compared via their three-body angle distributions. These distributions describe the angles subtended by a central water molecule and any two of its nearest neighbors. Compared to a simple fluid without directional interactions (e.g., liquid argon), the three-body angle distribution for water shows a pronounced shift in population towards the tetrahedral angle. In general, the presence of a surface causes the three-body angle distribution of near-surface water molecules to change, relative to the distribution in bulk water. Previously, shifts towards a reduction in tetrahedral population relative to bulk water have been seen in the hydration of extended, flat hydrophobic surfaces[40], while an enhanced tetrahedral population relative to bulk water has appeared as a signature of nanometer-scale hydrophobe solvation.[41] In this work, water near the benzene-modified surface shows increased tetrahedral ordering, compared to water near the inorganic surface (Fig. 3.3c). That is, adsorbed benzene induces increased tetrahedrality in the hydration-layer water, shifting the population of near-tetrahedral angles closer to that of bulk water (i.e., showing stronger preference for angles of ca. 109.5 °).

The benzene-modified surface also has a stronger *thermodynamic* signature of hydrophobicity than the inorganic surface. Specifically, the excess chemical potential μ_{ex}^{HS} for solvating a methane-sized (3.3 Å) hard sphere probe (i.e., an idealized small molecule

hydrophobe) near the surface is lower for the adsorbed-benzene surface than for the inorganic surface (Fig. A3.11). Specifically, within 0.8 nm of the surface, the value of μ_{ex}^{HS}/k_BT is (9.390 ± 0.003) for the benzene-modified surface, compared with (10.000 ± 0.004) for the control surface, consistent with increased hydrophobicity for the benzene-modified surface.

3.4 Discussion

Tuning surface hydrophobicity is a powerful method to control solute adsorption. Enzymes use hydrophobic hydration by locally ordered water to facilitate solute binding to their active sites, in which the interfacial water molecules serve as a low entropy reservoir. The liberation of ordered solvent molecules from hydrophobic zeolite micropores leads to large entropy gains upon solute adsorption, compensating for the enthalpic penalties associated with solvent reorganization.[42–44] In heterogeneous catalysis, this entropic effect can influence the energetics of adsorption, stabilize transition states, and ultimately increase catalytic activity.[43–45] The prospect of designing more heterogeneous catalysts with precisely configured hydrophobicities is appealing. This idea presupposes accurate information about the hydration thermodynamic properties of catalyst surfaces (usually, internal pore surfaces) and the chemical potentials of adsorbed solute molecules. Such measurements are lacking, because of the difficulty in applying many of the available tools, including single molecule force measurements,[23] Raman scattering of solutes and water molecules,[21] or THz absorption spectroscopy combined with MD simulation.[46] However, if the surface can be functionalized with a spin probe, ODNP can now be used to obtain the necessary insight, and to deconvolute the overlapping effects of geometry, surface chemistry, length scale, density, and heterogeneity.

As inorganic mesoporous silica (T100) becomes more hydrophobic due to progressive removal of its surface silanols, the diffusivity of its near-surface water increases. This change is consistent with a decrease in the number of hydrogen-bonding interactions between water molecules and surface silanol groups, which results in a reduced enthalpy of surface hydration. Interestingly, the increase in diffusivity shown in Fig. 3.2 is not gradual: there is negligible difference in water diffusivity for surface silanol densities of 1.8 and 1.2 nm^{-2} (corresponding to no additional thermal treatment, and thermal treatment at 600 °C, respectively), followed by an abrupt increase when the surface silanol density declined to 0.9 nm^{-2} (corresponding to thermal treatment at 900 °C). A further decrease in silanol density to 0.5 nm^{-2} (after thermal treatment at 1000 °C) gave a negligible change in diffusivity.

Similar observations were made in a study of water mobility near the surface of a non-porous silica, where the discontinuity appeared between pre-treatment temperatures of 700 and 800 °C.[2] It was attributed to disruption of a contiguous 2D water percolation network (silanol-water-silanol, connected through hydrogen bonds), which is present only above a threshold silanol density (ca. 1 nm^{-2} for mesoporous inorganic silica, Table 3.1, Fig. A3.7a). On silicas treated at lower temperatures, silanol clustering would create departures from the random distribution of surface silanols that allow the hydrogen-bond network to persist, even as the total silanol content varies significantly.[2,47–49] This type of clustering requires, by corollary, the presence of large silanol-free regions which interact weakly with water due to the low polarity of siloxane bonds.

In contrast to the modest effect of decreasing silanol density on water mobility, increasing the surface hydrophobicity via the incorporation of organic linkers into the silica framework results in a much more dramatic (and monotonic) change in the dynamics of

interfacial water. Furthermore, the change is *in the opposite direction*. Thus, the presence of organic groups appears to alter water dynamics by a mechanism that is entirely different from a scarcity of silanols. The slowing of surface water dynamics with increasing surface hydrophobicity in the organosilica series strongly suggests ordering of water molecules around the organic moieties, i.e., these embedded linkers are hydrated by low entropy water.

The computed structural shift towards increased tetrahedrality of interfacial water near the benzene-modified surface is also consistent with hydrophobic regions hydrated by ordered water, and with the established theoretical framework for the hydration of hydrophobic molecules, which predicts increased ordering of interfacial water and a corresponding reduction in entropy. In contrast, simulations of water near surfaces with extended hydrophobic regions predict that diffusivity should increase as the hard-sphere chemical potential decreases (i.e., as the surface becomes thermodynamically more hydrophobic).[4] The temperature dependence of the interfacial tension between aliphatic hydrocarbons and water shows that the sign of $\Delta S_{hydration}$ changes from negative to positive as the hydrocarbon chain length decreases.[18] Thus, the hydration of very small hydrophobes is entropy-driven. Since interfacial water molecules appear to experience the organic linkers in organosilica frameworks as discrete, small-scale perturbations to the extended silica surface, and the hydration of these surfaces should also be entropy-driven.

A quantitative framework was developed to estimate the hydrophobic length-scale for which entropic-enthalpic reversal in the Gibbs energy of hydration is expected to occur. Lum-Chandler-Weeks theory predicts that $\Delta G_{hydration}$ is dominated by entropy and scales with volume while for larger hydrophobes $\Delta G_{hydration}$ is dominated by enthalpy and scales with exposed surface area[22] since the hydration dynamics is governed by interface formation. The

transition is expected to occur on the nanometer length-scale. Studies of model hydrophobes also predict a characteristic length of ca. 1 nm for the entropic-enthalpic reversal.[19,20,22,50,51] Experimentally, water ordering has been observed for small hydrophobic solutes such as alkanes, alcohols and single polymer chains whose length-scales are, indeed, ≤ 1 nm.[21,23,52,53] The solute is encaged by laterally hydrogen-bonded water (i.e., not directly interacting with the hydrophobe), without disrupting the hydrogen-bond network of the surrounding water medium.

In principle, this entropic-enthalpic reversal may also occur in materials with extended surfaces (i.e., with dimensions much larger than nm) provided the chemical features have nm-scale dimensions, but no such observation has yet been made. Assuming the hydrophobic domains on organosilica surfaces are uniformly distributed, the length scale of the domain is determined mainly by the Si-Si distance associated with the Si-R-Si linker. Using typical Si-C and C-C bond lengths,[54–56] the relevant Si-Si distances are estimated to be 0.3, 0.6, and 1.1 nm for E100, B100, and BP100, respectively (Scheme 3.1). These sizes are comparable to the predicted crossover length scale (ca. 1 nm) for entropically- vs. enthalpically-driven hydration.[20,22,57] Several water molecules may form a hydrogen-bonded bridge (or dome) over the small organic domains, anchored by silanols located at the periphery (Scheme 3.3). Increasing the density of surface organic groups generates more low entropy spots, leading to gradually decreasing surface water mobility. Removal of the anchoring silanols should lead to an increase in surface water diffusivity, confirmed experimentally by the higher $D_{surface}$ value for B100 after thermal treatment at 350 °C to cause partial dehydroxylation.

3.5 Conclusion

The thermodynamic properties of interfacial water are key in modulating the strength of solute binding to surfaces. How the surface chemistry affects the local thermodynamic properties of interfacial water on real surfaces is poorly understood, and the deliberate design of inorganic surfaces in order to control surface water dynamics has not previously been reported. In this study, the effects of two types of progressive surface modification were investigated to make amorphous silica gradually more hydrophobic: (1) decreasing the silanol/siloxane ratio by thermal treatment, thereby creating large patches of hydrophobic, silanol-free regions that interact weakly with water, and (2) incorporating organic linkers into the silica framework, thereby creating small hydrophobic domains that induce local ordering of interfacial water (hydrophobic hydration). Thus the enthalpic and entropic contributions to surface hydration can be separately and deliberately altered by modulating the surface chemistry of silica. In particular, the ability to design low entropy "hotspots" with locally ordered water in silica mesopores is expected to inspire new approaches to improve the efficiency of separations and catalysis, by tuning the strength of solute adsorption.

3.6 Materials and methods

3.6.1 Chemicals

Tetraethylorthosilicate (TEOS, 98%), 1,4-bis(triethoxysilyl)benzene (BTEB, 96%), 4,4´-bis(triethoxysilyl)1-1´-biphenyl (BTEBP, 95%), 1,2-bis(trimethoxysilyl)ethane (BTME, 96%), Pluronic 123, 1,2,4-trimethylbenzene (TMB, 98%), vanadium oxytrichloride (99%), ammonium vanadate, hydrogen peroxide (30 wt% in H_2O), sulfuric acid (95.0 - 98.0 %), *N*-(3-dimethylaminopropyl)-*N*-ethylcarbodiimide hydrochloride, 2-(*N*-morpholino)ethanesulfonic acid (MES), and *N,N*-dimethyl-6-propionyl-2-naphthylamine

(Prodan) were purchased from Sigma Aldrich. 4-Carboxy-TEMPO and 3-aminopropyldimethylethoxysilane were purchased from Santa Cruz Biotechnology and Gelest, Inc., respectively. All were used as-received.

3.6.2 Synthesis and pretreatment of mesoporous silicas

The silica syntheses followed a previously described procedure,[13] with the exception of E100. Reagent amounts used to obtain each material are shown in Table A3.4. E100 was synthesized by modifying previously reported methods.[58,59] P123 (3.0 g) was dissolved in aqueous HCl (106 mL, 0.17 M) by stirring at 150 rpm overnight in a Pyrex glass flask at room temperature. 1,2-Bis(trimethoxysilyl)ethane (16 mmol) was injected dropwise. The mixture was heated to 40 °C in a warm water bath and agitated for 23 h. The reaction mixture was removed from the water bath and transferred to a Parr pressure vessel equipped with a Teflon liner (125 mL). The reactor was sealed and placed in an oven at 100 °C for 48 h. After cooling to room temperature, the resulting suspension was filtered and washed with ~500 mL water, then mixed with ~200 mL ethanol and stirred at 60 °C overnight. After filtering to remove ethanol containing the P123 surfactant, the surfactant extraction was repeated twice more.

Partially dehydroxylated inorganic silicas were obtained by heating T100 (500 mg) to the desired temperature in a tube furnace at a ramp rate of 10 °C/min, then holding for 6 h in a flow of dry N_2. To partially dehydroxylate B100, the organosilica (100 mg) was heated at 350 °C for 3 h in a flow of dry N_2. After thermal treatment, the silicas were stored in air prior to use. Readsorption of moisture from the laboratory ambient therefore partially restored their hydroxyl content. Further rehydroxylation occurred during functionalization with 4-carboxy-

TEMPO via propylamine linkers attached to the surface silanol groups, following a previously described method.[13]

3.6.3 Characterization of silica morphology

SEM images were obtained using a ThermoFisher Apero C LoVac Field Emission Gun Scanning Electron Microscopy (FEG SEM). X-ray powder diffraction patterns of air-exposed silicas were acquired using a Rigaku X-ray diffractometer equipped with Cu Kα radiation. N_2 sorption isotherms were measured at 77 K using a 3Flex Surface Characterization Analyzer (Micrometrics). Before each measurement, the silica was heated at 150 °C for 8 h in flowing N_2 to remove adsorbed water. Apparent surface areas were measured using the Brunauer-Emmett-Teller (B.E.T.) method, assuming a molecular area for adsorbed N_2 of 0.135 nm^2.[29] Pore size distributions were obtained by analyzing the adsorption branches of the isotherms, using the Barrett-Joyner-Halenda (B.J.H.) method.

3.6.4 Surface hydroxyl density measurements

Physically adsorbed water was removed from each silica by evacuation in a Schlenk tube at 170 °C and 10^{-4} Torr for 7 h. A portion of the dry silica (30 mg) was exposed to excess $VOCl_3$ vapor for 25 min to convert accessible silanols (≡SiOH) to ≡$SiOVOCl_2$, according to a previously described procedure.[26] The chemisorbed vanadium was extracted from a precisely weighed sample in air (approx. 10 mg) with a freshly-made H_2SO_4 solution (1 M, 5.0 mL) containing H_2O_2 (0.26 M). The UV-vis spectrum of the resulting solution was measured using a UV-2401 spectrophotometer (Shimadzu). The absorbance at 448 nm was converted to vanadium loading using a calibration curve prepared using ammonium vanadate.

3.6.5 Assessment of surface polarity

Each silica (20 mg) was immersed in water (1 mL) for 3 d, then an aqueous solution of Prodan (5 mL, 30 μM) was added, and stirred for 1 h. The mixture was centrifuged at 3000 rpm for 3 min, then the supernatant liquid was decanted. The wet solid containing adsorbed Prodan was dried using a rotary evaporator (Buchi Rotavapor R-210) at 30 °C and 100 mbar. After removing liquid water, the silica was further dried at 85 °C for 2 h in the oven and fluorescence spectrum was measured with a FluoroMax 4 fluorimeter (Horiba), using an excitation wavelength of 365 nm. The peak maximum λ_{max} was obtained from the zero-crossing of the first-derivative. In order to estimate the relative polarity of silica surfaces, λ_{max} values for dissolved Prodan in various solvents[31] were correlated with reported values for relative solvent polarity.[32] A second-order polynomial function fitted to the data was used to interpolate relative polarities for silicas based on their λ_{max} values.

3.6.6 Overhauser dynamic nuclear polarization (ODNP) NMR relaxometry

Functionalization of silica by 4-carboxy-TEMPO followed a previously described procedure.[13] Spin concentrations were estimated by comparison of the double integral of the EPR spectrum to the value for an aqueous solution of 4-carboxy-TEMPO (200 μM). A sample of spin-labeled silica suspended in water (40-80 mg/mL) was loaded into a quartz capillary tube (0.6 mm I.D., 0.84 mm O.D). The X-band continuous-wave (CW) EPR spectrum was recorded using a Bruker EMX CW EPR spectrometer equipped with a Bruker ER-4119HS-LC resonator, operating at a microwave frequency of ca. 9.3 GHz, 1 mW microwave power, 100 kHz modulation frequency, and 0.4 G modulation amplitude.

ODNP measurements were conducted at room temperature using a Bruker EMX CW EPR spectrometer and a Bruker Avance III NMR console. The sample was positioned inside the coil of a home-built NMR probe. The coil, an oval-shaped Helmholtz pair, was tuned and matched using an RLC circuit consisting of two variable capacitors and one fixed inductor. The coil and sample were positioned in the center of a microwave cavity (ER 4119HS-LC, Bruker Biospin). The software Xenon was used to tune the cavity. An EPR spectrum was acquired to identify the magnetic field value at the center of the spectrum (ca. 348.5 mT) and the resonant frequency of the loaded cavity (ca. 9.78 GHz). The NMR probe was subsequently tuned to the ^{1}H Larmor frequency at the magnetic field used in the experiments (ca. 14.83 MHz). NMR signal enhancements were measured upon irradiation of the central EPR resonance of the nitroxide radical, using applied microwave powers up to a maximum of approx. 6 W. The data used to calculate hydration parameters consist of an array of NMR signal enhancements measured as a function of applied microwave power, and the corresponding array of ^{1}H longitudinal relaxation times (T_1) at each applied microwave power.

Hydration parameters were calculated following previously published procedures,[16,60–62] as explained in more detail in the SI. Briefly, the NMR signal enhancement with microwave power caused by the Overhauser effect is asymptotic, due to the saturation behavior of the electron spin transition. An equation modeling the saturation profile is fitted to data describing the enhancement profile. The "cross-relaxivity", k_σ accounts for the effective rate of hyperpolarization, which is directly related to the rate of diffusion of water molecules near the spin label.[15]

3.6.7 Computational methods

MD simulations were performed in GROMACS (release 2016.1)[63] using the TIP4P-Ew water model,[64] in conjunction with force field parameters developed for models of amorphous silica interfaces.[65] The model is approximately 4 nm × 4 nm, and 2 nm thick. The PARMED package[66] was used to decrease the silanol density to approx. 1.5 OH/nm^2, by identifying pairs of silanols to undergo condensation. A hydroxyl group and a proton were removed before creating a siloxane bond between the remaining oxygen and the undercoordinated silicon. Silanol pairs considered for condensation were those with Si-Si distances ≤ 0.55 nm and O-O distances ≤ 0.45 nm. H-bonded silanol pairs with O-O distances ≤ 0.35 nm and O-H-O angles > 110 ° were removed first, before proceeding to condense other pairs.

To model the organosilica surface, benzene molecules were placed onto the silica surface at locations selected to avoid covering silanols. Parameters for benzene were obtained from the Automated Topology Builder.[67,68] An energy minimization was performed in vacuum with surface silicon atoms frozen, to allow the benzene molecules to achieve low-energy, adsorbed configurations. All surfaces were then solvated with 1840 water molecules and subjected to further energy minimization, while keeping surface silicon atoms and adsorbed benzene molecules frozen. After the simulation box dimension perpendicular to the interface was adjusted so that the water density far from the interface (bulk water, at least 1 nm from the silica surface) was close to its pressure-equilibrated value, a final energy minimization was performed with only silicon atoms frozen (in order to preserve the surface structure).

In all simulations, the time-step was 0.002 ps, with coordinates output every 0.5 ps. Equilibration consisted of an initial constant-volume run of 100 ps using a Berendsen

thermostat[69] with a coupling constant of 0.5 ps. Subsequently, the system was equilibrated with 200 ps of NPT simulation using the same thermostat and a Berendsen barostat set to 1 bar acting only on the dimension perpendicular to the box, with a coupling constant of 5 ps and a compressibility of 4.5 $\times 10^{-5}$ bar^{-1}. The constant pressure simulation was repeated to calculate the average box dimension perpendicular to the interface. The simulation box was scaled accordingly and 100 ps of further equilibration was performed in the NVT ensemble using a Nose-Hoover thermostat[70,71] at 300 K and with a coupling constant of 2 ps. The final production run, for which all analyses were performed, used the same thermostat for a total 10 ns. Dynamics were propagated with the velocity Verlet algorithm,[72] with all bonds involving hydrogen constrained via LINCS.[73] Throughout all MD simulations, the surface silicon atoms as well as three of the carbon atoms in all benzene rings were position-restrained with spring constants of 1000 kJ/mol·nm, allowing hydroxyl groups to move and form hydrogen bonds freely with water. Lennard-Jones and Coulombic pair interactions were cut and shifted to zero at 1.2 nm, with long-range electrostatics handled by the Smooth Particle Mesh Ewald algorithm using GROMACS default parameters.[74]

Three-body angle distributions were calculated as described in the literature,[41] considering the angle between all pairs of water oxygens within a radial distance of 0.332 nm (approx. the first RDF minimum for TIP4P-Ew water at ambient temperature and pressure) from a central water oxygen. Three-body angle distributions at surfaces consider only water oxygens within 0.8 nm of the mean interface, defined as the distance from the surface where the water oxygen density reaches 9.96 nm^{-3} (i.e., approx. 30 % of the bulk density). The pytraj package[75] was used to analyze the simulation trajectories.

Excess chemical potential of hard-sphere insertion is defined as $\mu_{ex}^{HS} = k_B T \ln p_V$, where p_V is the probability of successful insertion of a hard sphere of volume V, considering all configurations sampled during the simulation trajectory.[4] Successful insertions result when there is no overlap of the hard sphere with the centers of any water oxygen or surface heavy atoms. In this work, p_V was computed as a function of distance from the mean silica-water interface by counting the number of successful insertions of hard spheres of volume V placed at random locations in 2D planes of varying distance z from the surface.

3.7 References

(1) Vigil, G.; Xu, Z.; Steinberg, S.; Israelachvili, J. Interactions of Silica Surfaces. *J. Colloid Interface Sci.* **1994**, *165*, 367–385.

(2) Schrader, A. M.; Monroe, J. I.; Sheil, R.; Dobbs, H. A.; Keller, T. J.; Li, Y.; Jain, S.; Shell, M. S.; Israelachvili, J. N.; Han, S. Surface Chemical Heterogeneity Modulates Silica Surface Hydration. *Proc. Natl. Acad. Sci. U. S. A.* **2018**, *115*, 2890–2895.

(3) Law, K. Y. Definitions for Hydrophilicity, Hydrophobicity, and Superhydrophobicity: Getting the Basics Right. *J. Phys. Chem.* **2014**, *5*, 686–688.

(4) Monroe, J. I.; Shell, M. S. Computational Discovery of Chemically Patterned Surfaces That Effect Unique Hydration Water Dynamics. *Proc. Natl. Acad. Sci. U. S. A.* **2018**, *115*, 8093–8098.

(5) Xi, E.; Venkateshwaran, V.; Li, L.; Rego, N.; Patel, A. J.; Garde, S. Hydrophobicity of Proteins and Nanostructured Solutes Is Governed by Topographical and Chemical Context. *Proc. Natl. Acad. Sci. U. S. A.* **2017**, *114*, 13345–13350.

(6) Barnes, R.; Sun, S.; Fichou, Y.; Dahlquist, F. W.; Heyden, M.; Han, S. Spatially Heterogeneous Surface Water Diffusivity around Structured Protein Surfaces at Equilibrium. *J. Am. Chem. Soc.* **2017**, *139*, 17890–17901.

(7) Acharya, H.; Vembanur, S.; Jamadagni, S. N.; Garde, S. Mapping Hydrophobicity at the Nanoscale: Applications to Heterogeneous Surfaces and Proteins. *Faraday Discuss.* **2010**, *146*, 353.

(8) Baral, S.; Phillips, M.; Yan, H.; Avenso, J.; Gundlach, L.; Baumeier, B.; Lyman, E. Ultrafast Formation of the Charge Transfer State of Prodan Reveals Unique Aspects of the Chromophore Environment. *J. Phys. Chem. B* **2020**, *124*, 2643–2651.

(9) Klymchenko, A. S. Solvatochromic and Fluorogenic Dyes as Environment-Sensitive Probes: Design and Biological Applications. *Acc. Chem. Res.* **2017**, *50*, 366–375.

(10) Giovambattista, N.; Debenedetti, P. G.; Rossky, P. J. Effect of Surface Polarity on Water Contact Angle and Interfacial Hydration Structure. *J. Phys. Chem. B* **2007**, *111*, 9581–9587.

(11) Kanduč, M.; Schlaich, A.; Schneck, E.; Netz, R. R. Water-Mediated Interactions between Hydrophilic and Hydrophobic Surfaces. *Langmuir* **2016**, *32*, 8767–8782.

(12) Hamilton, W. C. A Technique for the Characterization of Hydrophilic Solid Surfaces. *J. Colloid Interface Sci.* **1972**, *40*, 219–222.

(13) Moon, H.; Han, S.; Scott, S. L. Tuning Molecular Adsorption in SBA-15-Type Periodic Mesoporous Organosilicas by Systematic Variation of Their Surface Polarity. *Chem. Sci.* **2020**, *11*, 3702–3712.

(14) Singappuli-Arachchige, D.; Manzano, J. S.; Sherman, L. M.; Slowing, I. I. Polarity Control at Interfaces: Quantifying Pseudo-Solvent Effects in Nano-Confined Systems. *ChemPhysChem* **2016**, *17*, 2982–2986.

(15) Biller, J. R.; Barnes, R.; Han, S. Perspective of Overhauser Dynamic Nuclear Polarization for the Study of Soft Materials. *Curr. Opin. Colloid Interface Sci.* **2018**, *33*, 72–85.

(16) Franck, J. M.; Pavlova, A.; Scott, J. A.; Han, S. Quantitative Cw Overhauser Effect Dynamic Nuclear Polarization for the Analysis of Local Water Dynamics. *Prog. Nucl. Magn. Reson. Spectrosc.* **2013**, *74*, 33–56.

(17) Fisette, O.; Päslack, C.; Barnes, R.; Isas, J. M.; Langen, R.; Heyden, M.; Han, S.; Schäfer, L. V. Hydration Dynamics of a Peripheral Membrane Protein. *J. Am. Chem. Soc.* **2016**, *138*, 11526–11535.

(18) Kauzmann, W. Some Factors in the Interpretation of Protein Denaturation. In *Advances in Protein Chemistry*; Academic Press, 1959; Vol. 14, pp 1–63.

(19) Athawale, M. V.; Jamadagni, S. N.; Garde, S. How Hydrophobic Hydration Responds to Solute Size and Attractions: Theory and Simulations. *J. Chem. Phys.* **2009**, *131*, 115102.

(20) Huang, D. M.; Geissler, P. L.; Chandler, D. Scaling of Hydrophobic Solvation Free Energies. *J. Phys. Chem. B* **2001**, *105*, 6704–6709.

(21) Davis, J. G.; Gierszal, K. P.; Wang, P.; Ben-Amotz, D. Water Structural Transformation at Molecular Hydrophobic Interfaces. *Nature* **2012**, *491*, 582–585.

(22) Lum, K.; Chandler, D.; Weeks, J. D. Hydrophobicity at Small and Large Length Scales. *J. Phys. Chem. B* **1999**, *103*, 4570–4577.

(23) Di, W.; Gao, X.; Huang, W.; Sun, Y.; Lei, H.; Liu, Y.; Li, W.; Li, Y.; Wang, X.; Qin, M.; Zhu, Z.; Cao, Y.; Wang, W. Direct Measurement of Length Scale Dependence of the Hydrophobic Free Energy of a Single Collapsed Polymer Nanosphere. *Phys. Rev. Lett.* **2019**, *122*, 047801.

(24) Zhuravlev, L. T. The Surface Chemistry of Amorphous Silica. Zhuravlev Model. *Colloids Surf., A* **2000**, *173*, 1–38.

(25) Ek, S. Determination of the Hydroxyl Group Content in Silica by Thermogravimetry and a Comparison with 1H MAS NMR Results. *Thermochim. Acta* **2001**, *379*, 201–212.

(26) Rice, G. L.; Scott, S. L. Characterization of Silica-Supported Vanadium(V) Complexes Derived from Molecular Precursors and Their Ligand Exchange Reactions. *Langmuir* **1997**, *13*, 1545–1551.

(27) Zhuravlev, L. T. Concentration of Hydroxyl Groups on the Surface of Amorphous Silicas. *Langmuir* **1987**, *3*, 316–318.

(28) Humbert, B. Estimation of Hydroxyl Density at the Surface of Pyrogenic Silicas by Complementary NMR and Raman Experiments. *J. Non-Cryst. Solids* **1995**, *191*, 29–37.

(29) Jelinek, L.; sz. Kovats, E. True Surface Areas from Nitrogen Adsorption Experiments. *Langmuir* **1994**, *10*, 4225–4231.

(30) Hammes, K.; Smernik, R. J.; Skjemstad, J. O.; Schmidt, M. W. I. Characterisation and Evaluation of Reference Materials for Black Carbon Analysis Using Elemental Composition, Colour, BET Surface Area and 13C NMR Spectroscopy. *Appl. Geochem.* **2008**, *23*, 2113–2122.

(31) Catalan, J.; Perez, P.; Laynez, J.; Blanco, F. G. Analysis of the Solvent Effect on the Photophysics Properties of 6-Propionyl-2-(Dimethylamino)Naphthalene (PRODAN). *J. Fluoresc.* **1991**, *1*, 215–223.

(32) Reichardt, C.; Welton, T. *Solvents and Solvent Effects in Organic Chemistry*, 4th edn.; Wiley-VCH: Weinheim, 2011.

(33) Mrowiec-Bialoń, J. Determination of Hydroxyls Density in the Silica-Mesostructured Cellular Foams by Thermogravimetry. *Thermochim. Acta* **2006**, *443*, 49–52.

(34) Shioji, S.; Kawaguchi, M.; Hayashi, Y.; Tokami, K.; Yamamoto, H. Rehydroxylation of Dehydrated Silica Surfaces by Water Vapor Adsorption. *Adv. Powder Technol.* **2001**, *12*, 331–342.

(35) Ide, M.; El-Roz, M.; De Canck, E.; Vicente, A.; Planckaert, T.; Bogaerts, T.; Van Driessche, I.; Lynen, F.; Van Speybroeck, V.; Thybault-Starzyk, F.; Van Der Voort, P. Quantification of Silanol Sites for the Most Common Mesoporous Ordered Silicas and Organosilicas: Total versus Accessible Silanols. *Phys. Chem. Chem. Phys.* **2013**, *15*, 642–650.

(36) Xu, X.; Zhao, Y.; Wang, J.; Zhang, N.; Wang, C.; Zhang, J.; Wei, N. Water Flow inside Various Geometric Nano-Confinement Channels. *Phys. Chem. Chem. Phys.* **2020**, *22*, 24633–24639.

(37) Tohidi, M.; Toghraie, D. The Effect of Geometrical Parameters, Roughness and the Number of Nanoparticles on the Self-Diffusion Coefficient in Couette Flow in a Nanochannel by Using of Molecular Dynamics Simulation. *Physica B Condens. Matter.* **2017**, *518*, 20–32.

(38) Wei, M.-J.; Zhou, J.; Lu, X.; Zhu, Y.; Liu, W.; Lu, L.; Zhang, L. Diffusion of Water Molecules Confined in Slits of Rutile TiO2(110) and Graphite(0001). *Fluid Phase Equilib.* **2011**, *302*, 316–320.

(39) Fujita, S.; Inagaki, S. Self-Organization of Organosilica Solids with Molecular-Scale and Mesoscale Periodicities. *Chem. Mater.* **2008**, *20*, 891–908.

(40) Stock, P.; Monroe, J. I.; Utzig, T.; Smith, D. J.; Shell, M. S.; Valtiner, M. Unraveling Hydrophobic Interactions at the Molecular Scale Using Force Spectroscopy and Molecular Dynamics Simulations. *ACS Nano* **2017**, *11*, 2586–2597.

(41) Monroe, J. I.; Shell, M. S. Decoding Signatures of Structure, Bulk Thermodynamics, and Solvation in Three-Body Angle Distributions of Rigid Water Models. *J. Chem. Phys.* **2019**, *151*, 094501.

(42) Bai, P.; Siepmann, J. I.; Deem, M. W. Adsorption of Glucose into Zeolite Beta from Aqueous Solution. *AIChE J.* **2013**, *59*, 3523–3529.

(43) Di Iorio, J. R.; Johnson, B. A.; Román-Leshkov, Y. Ordered Hydrogen-Bonded Alcohol Networks Confined in Lewis Acid Zeolites Accelerate Transfer Hydrogenation Turnover Rates. *J. Am. Chem. Soc.* **2020**, *142*, 19379–19392.

(44) Cordon, M. J.; Harris, J. W.; Vega-Vila, J. C.; Bates, J. S.; Kaur, S.; Gupta, M.; Witzke, M. E.; Wegener, E. C.; Miller, J. T.; Flaherty, D. W.; Hibbitts, D. D.; Gounder, R. Dominant Role of Entropy in Stabilizing Sugar Isomerization Transition States within Hydrophobic Zeolite Pores. *J. Am. Chem. Soc.* **2018**, *140*, 14244–14266.

(45) Serva, A.; Salanne, M.; Havenith, M.; Pezzotti, S. Size Dependence of Hydrophobic Hydration at Electrified Gold/Water Interfaces. *Proc. Natl. Acad. Sci. U. S. A.* **2021**, *118*, e2023867118.

(46) Conti Nibali, V.; Pezzotti, S.; Sebastiani, F.; Galimberti, D. R.; Schwaab, G.; Heyden, M.; Gaigeot, M.-P.; Havenith, M. Wrapping Up Hydrophobic Hydration: Locality Matters. *J. Phys. Chem. Lett.* **2020**, *11*, 4809–4816.

(47) Chien, J. C. W. A Study of Surface Structures of Submicron Metal Oxides by Vanadium Tetrachloride as a Paramagnetic Probe. *J. Am. Chem. Soc.* **1971**, *93*, 4675–4684.

(48) Peri, J. B.; Hensley, A. L. The Surface Structure of Silica Gel. *J. Phys. Chem.* **1968**, *72*, 2926–2933.

(49) Cyran, J. D.; Donovan, M. A.; Vollmer, D.; Siro Brigiano, F.; Pezzotti, S.; Galimberti, D. R.; Gaigeot, M.-P.; Bonn, M.; Backus, E. H. G. Molecular Hydrophobicity at a Macroscopically Hydrophilic Surface. *Proc. Natl. Acad. Sci. U. S. A.* **2019**, *116*, 1520–1525.

(50) Rajamani, S.; Truskett, T. M.; Garde, S. Hydrophobic Hydration from Small to Large Lengthscales: Understanding and Manipulating the Crossover. *Proc. Natl. Acad. Sci. U. S. A.* **2005**, *102*, 9475–9480.

(51) Huang, D. M.; Chandler, D. The Hydrophobic Effect and the Influence of Solute−Solvent Attractions. *J. Phys. Chem. B* **2002**, *106*, 2047–2053.

(52) Wu, X.; Lu, W.; Streacker, L. M.; Ashbaugh, H. S.; Ben-Amotz, D. Temperature-Dependent Hydrophobic Crossover Length Scale and Water Tetrahedral Order. *J. Phys. Chem. Lett.* **2018**, *9*, 1012–1017.

(53) Grdadolnik, J.; Merzel, F.; Avbelj, F. Origin of Hydrophobicity and Enhanced Water Hydrogen Bond Strength near Purely Hydrophobic Solutes. *Proc. Natl. Acad. Sci. U.S.A.* **2017**, *114*, 322–327.

(54) Xiao, S.; Myers, M.; Miao, Q.; Sanaur, S.; Pang, K.; Steigerwald, M. L.; Nuckolls, C. Molecular Wires from Contorted Aromatic Compounds. *Angew. Chem., Int. Ed.* **2005**, *44*, 7390–7394.

(55) Tacke, R.; Mallak, M.; Willeke, R. Pentacoordination of Silicon by Four Covalent Si−S Bonds and One Covalent Si−C Bond. *Angew. Chem., Int. Ed.* **2001**, *113*, 2401–2403.

(56) Beagley, B.; Monaghan, J. J.; Hewitt, T. G. Electron-Diffraction Studies of Tetramethylsilane and Hexamethyldisilane, and Discussion of the Lengths of Si-C Bonds. *J. Mol. Struct.* **1971**, *8*, 401–411.

(57) Huang, D. M.; Chandler, D. Temperature and Length Scale Dependence of Hydrophobic Effects and Their Possible Implications for Protein Folding. *Proc. Natl. Acad. Sci. U. S. A.* **2000**, *97*, 8324–8327.

(58) Esquivel, D.; Ouwehand, J.; Meledina, M.; Turner, S.; Tendeloo, G. V.; Romero-Salguero, F. J.; Clercq, J. D.; Voort, P. V. D. Thiol-Ethylene Bridged PMO: A High Capacity Regenerable Mercury Adsorbent via Intrapore Mercury Thiolate Crystal Formation. *J. Hazard. Mater.* **2017**, *339*, 368–377.

(59) Sanchez, C.; Jeremias, F.; Ernst, S.-J.; Henninger, S. K. Synthesis, Functionalization and Evaluation of Ethylene-Bridged PMOs as Adsorbents for Sorption Dehumidification and Cooling Systems. *Micropor. Mesopor. Mat.* **2017**, *244*, 151–157.

(60) Armstrong, B. D.; Han, S. Overhauser Dynamic Nuclear Polarization To Study Local Water Dynamics. *J. Am. Chem. Soc.* **2009**, *131*, 4641–4647.

(61) Franck, J. M.; Kausik, R.; Han, S. Overhauser Dynamic Nuclear Polarization-Enhanced NMR Relaxometry. *Micropor. Mesopor. Mat.* **2013**, *178*, 113–118.

(62) Armstrong, B. D.; Han, S. A New Model for Overhauser Enhanced Nuclear Magnetic Resonance Using Nitroxide Radicals. *J. Chem. Phys.* **2007**, *127*, 104508.

(63) Abraham, M. J.; Murtola, T.; Schulz, R.; Páll, S.; Smith, J. C.; Hess, B.; Lindahl, E. GROMACS: High Performance Molecular Simulations through Multi-Level Parallelism from Laptops to Supercomputers. *SoftwareX* **2015**, *1–2*, 19–25.

(64) Horn, H. W.; Swope, W. C.; Pitera, J. W.; Madura, J. D.; Dick, T. J.; Hura, G. L.; Head-Gordon, T. Development of an Improved Four-Site Water Model for Biomolecular Simulations: TIP4P-Ew. *J. Chem. Phys.* **2004**, *120*, 9665–9678.

(65) Emami, F. S.; Puddu, V.; Berry, R. J.; Varshney, V.; Patwardhan, S. V.; Perry, C. C.; Heinz, H. Force Field and a Surface Model Database for Silica to Simulate Interfacial Properties in Atomic Resolution. *Chem. Mater.* **2014**, *26*, 2647–2658.

(66) Swails, J.; Hernandez, C.; Mobley, D. L.; Nguyen, H.; Wang, L. P.; Janowski, P. ParmEd: Cross-Program Parameter and Topology File Editor and Molecular Mechanical Simulator Engine Http://Parmed.Github.Io/ParmEd/Html/Index.Html (Accessed Dec 5, 2016).

(67) Malde, A. K.; Zuo, L.; Breeze, M.; Stroet, M.; Poger, D.; Nair, P. C.; Oostenbrink, C.; Mark, A. E. An Automated Force Field Topology Builder (ATB) and Repository: Version 1.0. *J. Chem. Theory Comput.* **2011**, *7*, 4026–4037.

(68) Stroet, M.; Caron, B.; Visscher, K. M.; Geerke, D. P.; Malde, A. K.; Mark, A. E. Automated Topology Builder Version 3.0: Prediction of Solvation Free Enthalpies in Water and Hexane. *J. Chem. Theory Comput.* **2018**, *14*, 5834–5845.

(69) Berendsen, H. J. C.; Postma, J. P. M.; van Gunsteren, W. F.; DiNola, A.; Haak, J. R. Molecular Dynamics with Coupling to an External Bath. *J. Chem. Phys.* **1984**, *81*, 3684–3690.

(70) Hoover, W. G. Canonical Dynamics: Equilibrium Phase-Space Distributions. *Phys. Rev. A* **1985**, *31*, 1695–1697.

(71) Martyna, G. J.; Klein, M. L.; Tuckerman, M. Nosé–Hoover Chains: The Canonical Ensemble via Continuous Dynamics. *J. Chem. Phys.* **1992**, *97*, 2635–2643.

(72) Swope, W. C.; Andersen, H. C.; Berens, P. H.; Wilson, K. R. A Computer Simulation Method for the Calculation of Equilibrium Constants for the Formation of Physical Clusters of Molecules: Application to Small Water Clusters. *J. Chem. Phys.* **1982**, *76*, 637–649.

(73) Hess, B.; Bekker, H.; Berendsen, H. J. C. LINCS: A Linear Constraint Solver for Molecular Simulations. *J. Comput. Chem.* **1997**, *18*, 10.

(74) Essmann, U.; Perera, L.; Berkowitz, M. L.; Darden, T.; Lee, H.; Pedersen, L. G. A Smooth Particle Mesh Ewald Method. *J. Chem. Phys.* **1995**, *103*, 8577–8593.

(75) Nguyen, H.; Roe, D. R.; Swails, J.; Case, D. A. PYTRAJ: Interactive Data Analysis for Molecular Dynamics Simulations (Accessed Dec 5, 2016).

3.8 Appendix II

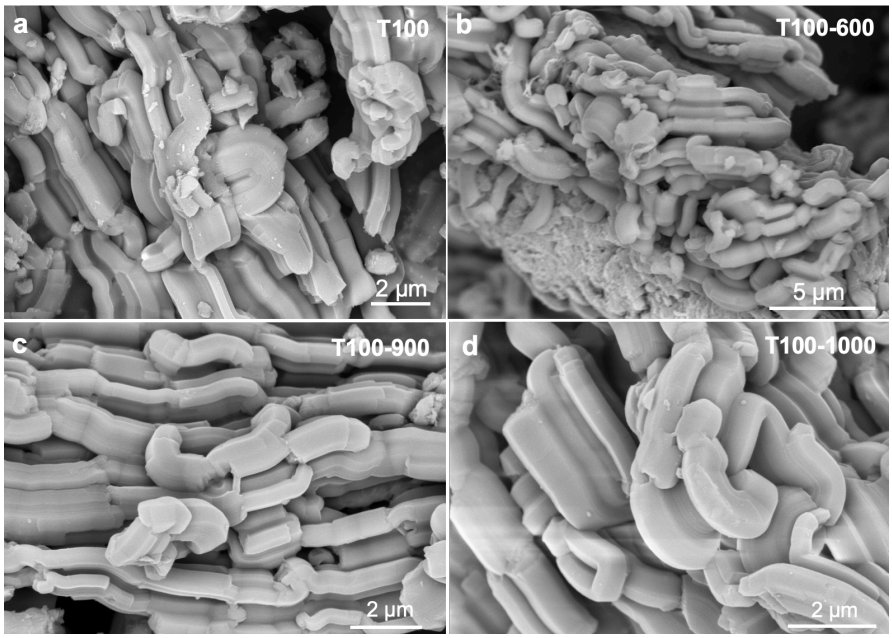

Fig. A3.1. SEM images of mesoporous inorganic silicas before and after thermal treatment from 600 to 1000 °C.

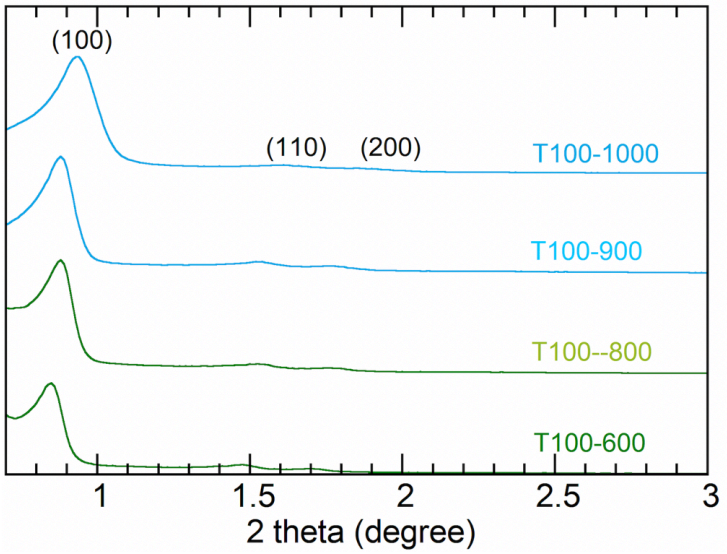

Fig. A3.2. Small-angle XRD patterns of mesoporous inorganic silicas (T100) after thermal treatment from 600 to 1000 °C.

Table A3.1. Physicochemical properties of mesoporous (organo)silicas [a]

Silicas	Thermal treatment temperature (°C)	Framework linkers				B.E.T. surface area (m^2 g^{-1}) [b]	Pore volume (cm^3 g^{-1}) [c]	Pore size (nm) [d]
		Oxo	Phenylene	Biphenylene	Ethylene			
T100-none	-	•				709	1.12	9.7 ± 0.5
T100-600	600	•				644	1.01	8.8 ± 0.7
T100-800	800	•				498	0.87	8.3 ± 0.7
T100-900	900	•				444	0.86	7.9 ± 0.8
T100-1000	1000	•				353	0.63	7.0 ± 0.8
T75-B25	-	•	•			668	0.99	7.6 ± 0.3
B100	-	•	•			721	1.08	7.6 ± 0.8
B75-BP25	-	•		•		719	1.01	6.3 ± 0.3
BP100	-	•		•		728	1.18	5.0 ± 3.6
E100	-	•			•	791	1.43	7.1 ± 0.5

[a] Physicochemical properties of phenylene and/or biphenylene bridged organosilicas are excerpted from our previous literature.[1] [b] Surface area was obtained using the Brunauer-Emmett-Teller (B.E.T) method, assuming an area of adsorbed N_2 of 0.135 nm^2 per molecule.[2] [c] Measured at P/P_0 = 0.99. [d] Pore size and its standard deviation were calculated using the Barrett-Joyner-Halenda (B.J.H.) method.

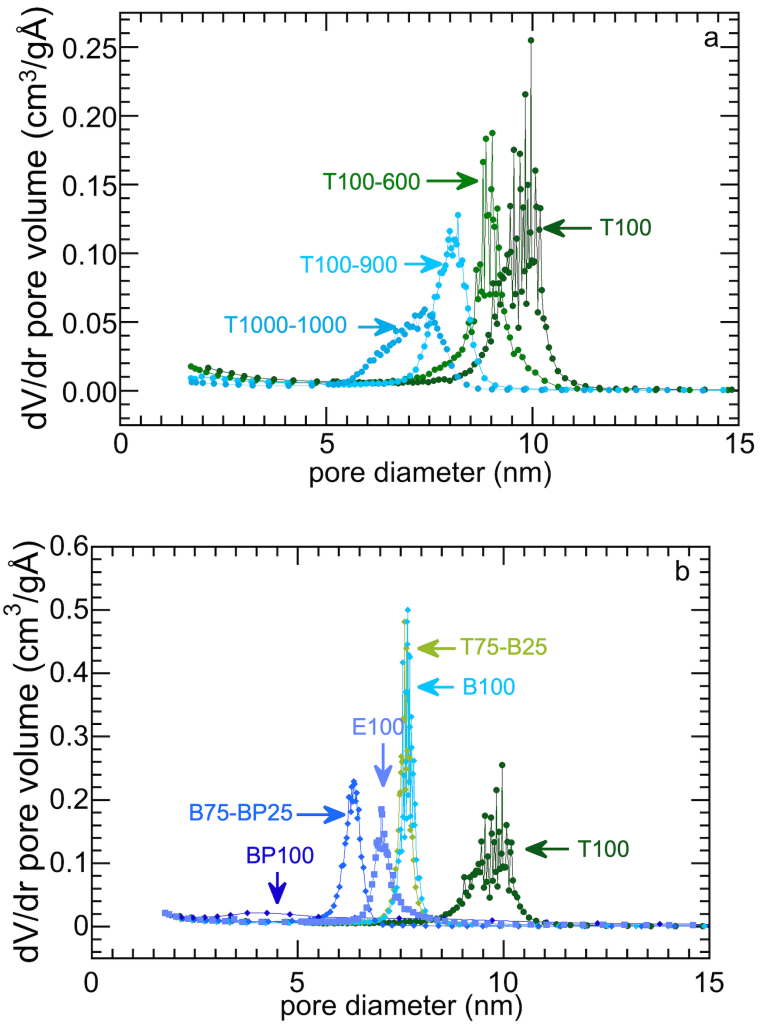

Fig. A3.3. Pore size distribution of mesoporous (a) inorganic silicas and (b) organosilicas.

Table A3.2. Silanol density before and after rehydroxylation

Silicas	Thermal treatment temperature. (°C)	Before rehydroxylation, α_{OH} (nm^{-2})	3 d after rehydroxylation α_{OH} (nm^{-2})
T100-600	600	0.6	1.2
T100-900	900	0.3	0.9
T100-1000	1000	0.1	0.5

Table A3.3. Relative polarities of various solvents, and their Prodan emission maxima (nm)

Solvent	Relative polarity [a]	λ_{max} [b]
water	1.000	527.5
2,2,2-trifluoroethanol	0.898	517.6
Ethylene-glycol	0.790	513.6
Methanol	0.762	502.7
Formamide	0.775	501.8
2,2,2-trichloroethanol	0.722	500.8
Ethanol	0.654	493.0
1-propanol	0.617	486.8
1-butanol	0.586	484.4
2-propanol	0.546	479.8
1-octanol	0.537	476.4
Cyclohexanol	0..509	475.1
Dimethyl sulfoxide (DMSO)	0.444	464.5

[a] Inferred previously, by measuring the shift in the absorption spectrum of Reichardt's dye.[3]

[b] From a previous study.[4]

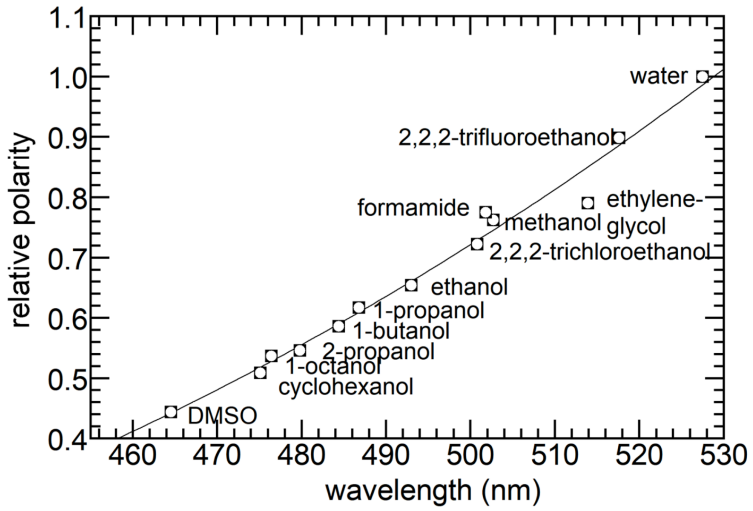

Fig. A3.4. Correlations between the relative polarities[3] and Prodan fluorescence emission maxima of various solvents.[4] The data are fitted using a second order polynomial function.

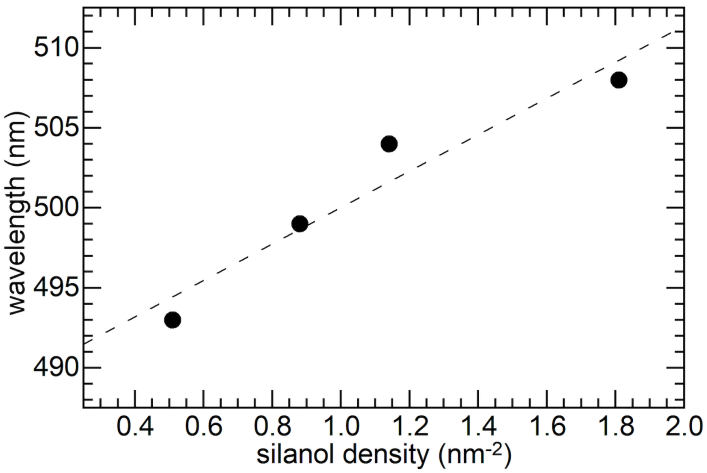

Fig. A3.5. Correlations between the silanol density of T100 inorganic silicas and Prodan fluorescence wavelength.

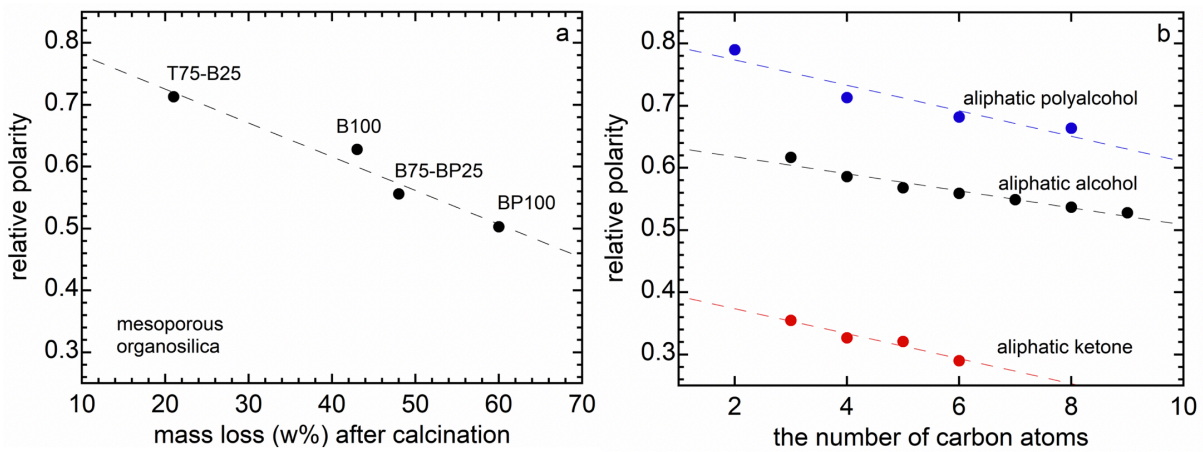

Fig. A3.6. Relative polarity of (a) mesoporous organosilica as a fucntion of mass loss after calcination at 720 °C (b) Relative polarity of aliphatic alcohol, ketone, and polyalcohol as a function of the number of carbon atoms.[3] Aliphatic alcohol includes 1-propanol, 1-butanol, etc. Aliphatic ketones are propanone, 2-butanone, etc, and aliphatic polyalcohols are ethylene glycol, diethylene glycol, etc.

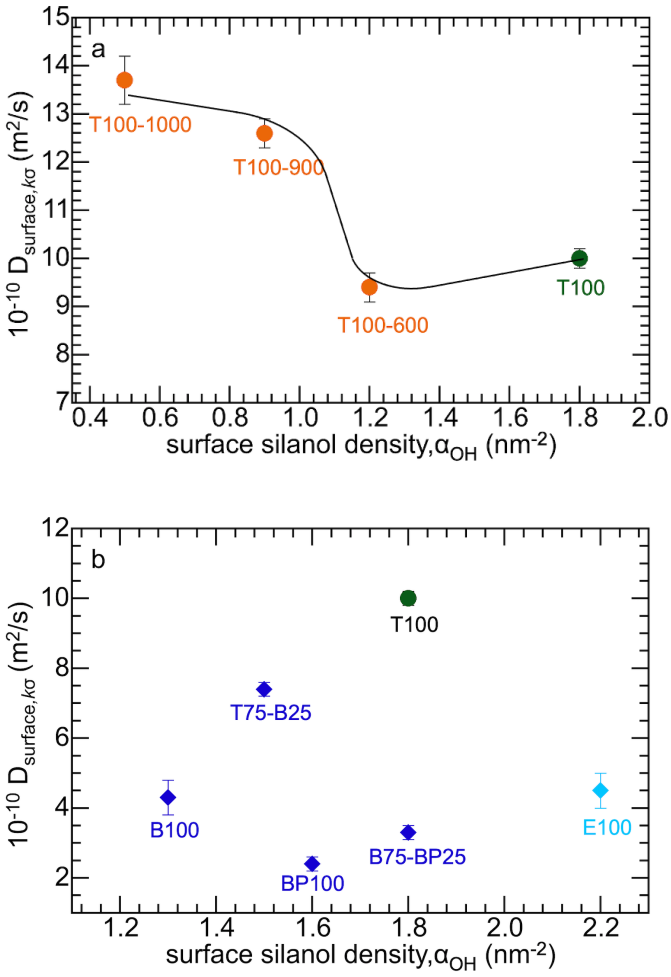

Fig. A3.7. Surface water diffusivity ($D_{surface,k\sigma}$) near (a) mesoporous inorganic silicas and (b) mesoporous organosilica, as a function of their relative surface silanol density. Linker composition in silicas (●: siloxane; ◆: ethylene, phenylene- and/or biphenylene).

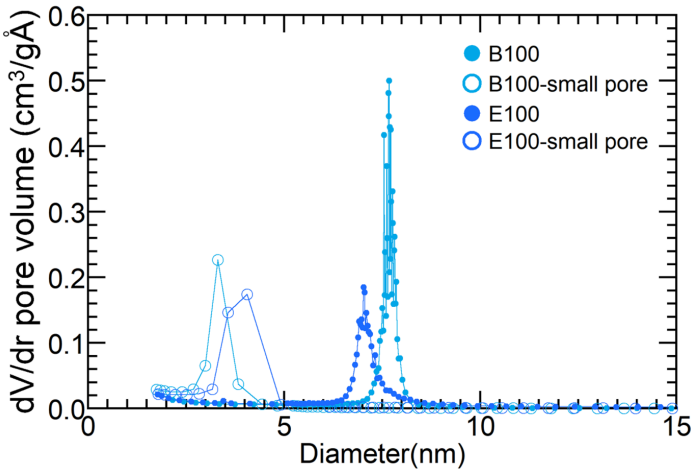

Fig. A3.8. Pore size distributions for small pore and large pore B100 and E100.

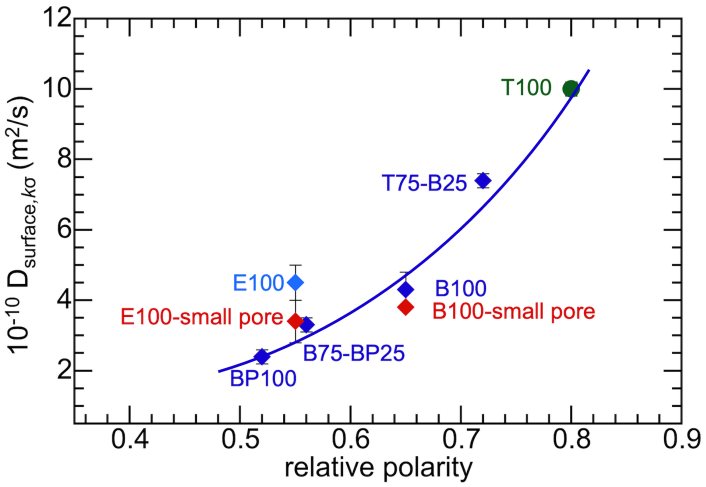

Fig. A3.9. Surface water diffusivity ($D_{surface,k\sigma}$) near mesoporous organosilica, as a function of their relative polarity. The phenylene and ethylene bridged organosilicas with smaller pore sizes (ca. 4 nm) were synthesized using Brij®S10 surfactant following the previous method.[5]

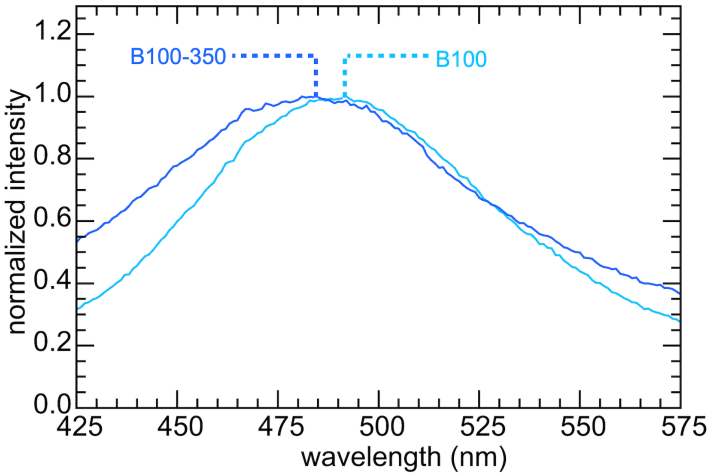

Fig. A3.10. Fluorescence spectrum for Prodan adsorbed on phenylene-bridged organosilica (B100) and thermal-treated B100 at 350 °C under N_2 flow (B100-350).

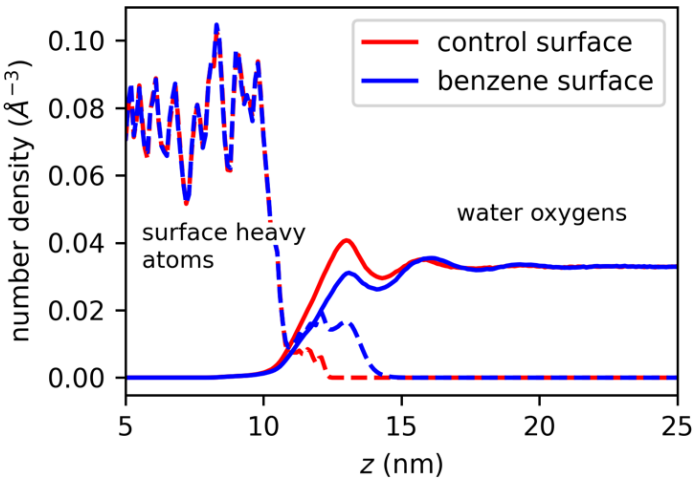

Fig. A3.11. Number density of water oxygens and heavy surface atoms (Si, O, and C), averaged over the x and y directions, is given as a function of distance z from the center of the surface. Far away from the water-surface interface (around z=11), densities are identical between the control and adsorbed-benzene surface. Near the water-surface interface, an additional heavy-atom peak for the benzene surface indicates the presence of adsorbed benzenes. The first peak in water density for the benzene surface is diminished in magnitude compared with the control surface, but occurs at an identical distance from the center of the surface.

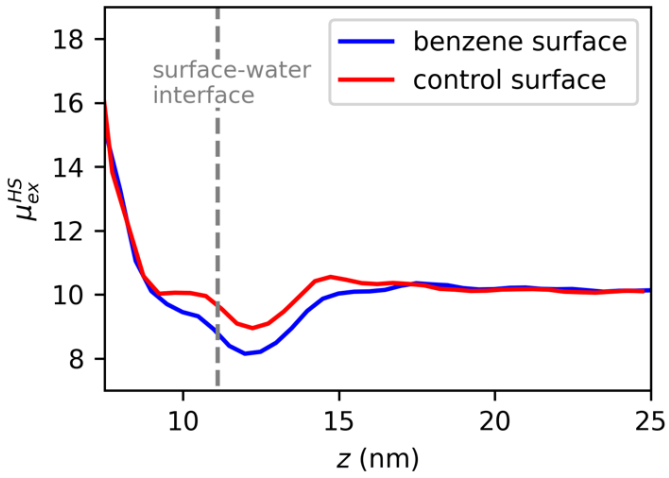

Fig. A3.12. The excess chemical potential for inserting a methane-sized (3.3 Å) hard-sphere probe as a function of distance from the center of the surface is given, calculated using the Widom insertion method. The approximate location of the water-surface interface, calculated using water density plots, is depicted via the dashed vertical line. Near the water-surface interface, the μ_{ex}^{HS} for the benzene surface tends to be lower than that of the control surface. This suggests that displacing water with a hydrophobic hard-sphere probe is more favorable in the adsorbed-benzene case, and indicates that this surface is thermodynamically more hydrophobic than the control.

Table A3.4. Synthesis composition of mesoporous (organo)silicas.

Material[a]	Silica precursor	Amount (mmol)	HCl[f] (mL)	Surfactant	Amount (g)
T100-none	TEOS[b]	30	1.8	P123	3.0
T75-B25	TEOS / BTEB[c]	12.5 / 4.2	1.8	P123	3.0
B100	BTEB	7.2	1.8	P123	3.0
B75-BP25	BTEB / BTEBP[d]	5.5 / 1.8	1.8	P123	3.0
BP100	BTEBP	6.5	5.5	P123/1-BuOH	3.0 / 4.0
E100	BTME[e]	16	1.8	P123	3.0

[a] The numbers in the abbreviated names represent precursor molar ratios used in the synthesis mixture. [b]Tetraethyl orthosilicate. [c]1,4-Bis(triethoxysilyl)benzene. [d]4,4′-bis(triethoxysilyl)1-1′-biphenyl. [e]1,2-bis(trimethoxysilyl)ethane. [f]HCl 36.5 % [g]1,2,4-trimethylbenzene.

Additional references

(1) Moon, H.; Han, S.; Scott, S. L. Tuning Molecular Adsorption in SBA-15-Type Periodic Mesoporous Organosilicas by Systematic Variation of Their Surface Polarity. *Chem. Sci.* **2020**, *11*, 3702–3712.

(2) Jelinek, L.; sz. Kovats, E. True Surface Areas from Nitrogen Adsorption Experiments. *Langmuir* **1994**, *10*, 4225–4231.

(3) Reichardt, C.; Welton, T. *Solvents and Solvent Effects in Organic Chemistry*, 4th edn.; Wiley-VCH: Weinheim, 2011.

(4) Catalan, J.; Perez, P.; Laynez, J.; Blanco, F. G. Analysis of the Solvent Effect on the Photophysics Properties of 6-Propionyl-2-(Dimethylamino)Naphthalene (PRODAN). *J. Fluoresc.* **1991**, *1*, 215–223.

(5) Sebastián Manzano, J.; Singappuli-Arachchige, D.; Parikh, B. L.; Slowing, I. I. Fine-Tuning the Release of Molecular Guests from Mesoporous Silicas by Controlling the Orientation and Mobility of Surface Phenyl Substituents. *Chem. Eng. J.* **2018**, *340*, 73–80.

Chapter 4. *Operando* observation of the molecular adsorption effect on the activity and selectivity in phenol hydrogenation over hydrophilic and hydrophobic Pd catalysts

4.1 Abstract

The extent of interaction between reactants and a catalytically active surface in the presence of a solvent is an important factor controlling catalytic activity and selectivity. Liquid phase conditions are particularly relevant to the conversion of lignocellulosic biomass and its derivatives, such as glucose isomerization/dehydration and monolignol hydrogenolysis/hydrogenation. To assess the influence of surface composition on the extent of phenol adsorption, and the resulting effect on catalytic activity and selectivity in phenol hydrogenation, Pd nanoparticles were supported on hydrophilic and hydrophobic mesoporous silica made using organosilica precursors. These materials were used to catalyze phenol hydrogenation at 60 °C, while *operando* NMR spectra were collected. Additional peaks representing molecules (phenol, cyclohexanone, and cyclohexanol) interacting with the surface were observed. The peaks shifted during the reaction due to changes in the chemical composition of the adsorbed layer. Kinetic profiles indicate that a hydrophobic catalyst with biphenylene linkers gives a higher phenol conversion rate and selectivity to cyclohexanone than a corresponding hydrophilic catalyst. Analysis of in situ NMR arrays and ex situ adsorption suggest that increased phenol concentration at the surface leads to increased Pd active site-phenol interactions, suppressing the reaction of cyclohexanone in spite of an increase in cyclohexanone adsorption onto the support.

4.2 Introduction

Valorization of biomass to chemicals and fuels is an important process to lower dependence on fossil sources and reduce carbon footprints.[1–3] In order to enable efficient biomass conversion by the heterogeneous catalytic systems, various strategies have been introduced.[4,5] One of the well-known catalytic systems in biomass conversion to renewable chemicals such as furfural and 5-hydroxymethyl furfural is a biphasic solvent system consisting of aqueous and organic solvents. The reactant and catalyst are both present in the aqueous phase, but the product is efficiently extracted into an organic solvent that does not contain the catalyst.[6–8] In this way, both catalytic activity and selectivity are improved. Similarly, varying the surface hydrophilicity/hydrophobicity has been investigated to alter the interactions of reactants or products with catalyst surfaces.[9–13] For example, furfural hydrogenation to furan was explored using a hydrophilic zeolite with a higher silanol density.[13] The hydrophilic surface promotes efficient desorption of the product, furan, thereby minimizing the formation of the by-products, dihydrofuran and tetrahydrofuran.[13] Thus designing catalyst surface properties based on controlling interactions with reactant or product molecules can be a powerful strategy to improve activity and selectivity.

An indirect way to evaluate the interaction between the surface and a molecule in solution involves measuring the change in solution concentration due to adsorption. In this way, the extent of molecular adsorption onto a catalyst is obtained.[13–15] Alternatively, the adsorbate-catalyst interaction can be observed directly, using a spectroscopic technique such as MAS NMR.[16–19] The interaction is manifested in the NMR by a broader peak with a slightly different chemical shift compared to that of the molecule in the bulk solution, due to restricted mobility of adsorbed molecules. The fraction of adsorbed species can be quantified using the

areas of adsorbed and solution-phase NMR peaks. For instance, a ^{13}C MAS NMR investigation of zeolite-glucose mixtures in a water-γ-valerolactone (GVL) mixed solvent at 298 K showed that 65 % of the glucose was confined in the micropores when the solvent contained 46 mol% GVL.[20] Conducting a catalytic reaction in *operando* mode using MAS NMR spectroscopy allows observation of the reaction kinetics[21,22] as well as the fraction of adsorbed species,[20] meaning that the effect of molecular adsorption can be investigated *in-situ.* This combination can provide valuable information regarding surface effects on activity and selectivity.

In this study, phenol hydrogenation was chosen as a model reaction in order to investigate the effect of molecular adsorption on activity/selectivity. Phenol is one of the compounds formed during lignin pyrolysis,[23] and previous literature has shown that phenol adsorption can vary greatly on different surfaces.[24,25] Thus, determining the relationship between phenol adsorption and activity/selectivity in hydrogenation can shed light on how to convert other aromatic compounds derived from lignin, such as guaiacol, cresol, and vanillin.[26–28]

Previous studies on phenol hydrogenation over Pd-based catalysts suggest that the selectivity to cyclohexanone or cyclohexanol is determined by the orientation of adsorbed phenol. Non-planar or co-planar adsorption was proposed to lead to cyclohexanone or cyclohexanol, respectively.[29–33] In particular, it was suggested that adsorption on Al_2O_3 was suggested to be co-planar, yielding cyclohexanol as the main product.[32] However, few studies show selectivity to cyclohexanol over Pd/Al_2O_3 catalysts.[34,35] Instead, a number of works report that Pd catalysts are selective to cyclohexanone, which can be further hydrogenated to

cyclohexanol.[36–38] These results indicate that convincing explanation for the effect of the reactant-support interaction on selectivity has yet to be found.

In this work, we focus on the effect of molecular adsorption on activity and selectivity. Hydrophilic SBA-15-type mesoporous silica with a surface consisting of siloxane and silanol groups, as well as hydrophobic mesoporous silicas containing biphenylene linker, were synthesized. The surface polarities of each Pd catalyst were assessed by measuring the fluorescence of adsorbed Prodan, which blue-shifts when the polarity of its environment decreases.[39,40] Subsequently, kinetic profiles for phenol hydrogenation were measured and amounts of adsorbed species were quantified using ^{13}C MAS NMR in *operando* mode. The effect of molecular adsorption is interpreted based on adsorption profiles and kinetic analysis using a Langmuir Hinshelwood mechanism.

4.3 Materials and methods

4.3.1 Chemicals

All commercial materials were used as received. Tetraethylorthosilicate (T, 98%), 4,4′-bis(triethoxysilyl)-1,1′-biphenyl (BP, 95%), Pluronic P123, unlabeled phenol (99%), *N*,*N*-dimethyl-6-propionyl-2-naphthylamine (Prodan), palladium(II) acetate, and acetonitrile (≥99.9%) were purchased from Sigma Aldrich. Labeled phenol (1-^{13}C, 99%) was obtained from Cambridge Isotope Laboratories, Inc. H_2 (5 % in N_2 and 10 % in Ar), CO (9.890 % in He) and He (UHP) were purchased from Airgas, Inc. MCM-41(pore size: 2.7 nm, B.E.T. surface area: 682 m^2/g) was purchased from Advanced Chemical Supplier (ACS) Material LLC and used as-received.

4.3.2 Catalyst preparation

The SBA-15-type silica and organosilica used as catalyst supports were synthesized by templated condensation of T or BP, following previously reported methods.[41–43] Hydrophilic (Pd-T) and hydrophobic (Pd-BP) catalysts were prepared via incipient wetness impregnation. Pd(II) acetate (5.3 mg) was dissolved in acetonitrile (250 or 380 μL for Pd-T and Pd-BP, respectively). The solids were dried at 80 °C for 3 h, then heated in air to 300 °C with a ramp rate of 1 °C/min and held for 2 h. The resulting materials contain 0.95 and 0.94 wt% Pd for Pd-BP and Pd-T, respectively. Both catalysts were activated by reduction at 200 °C for 2 h in flowing 5 % H_2/N_2. The reduced catalysts were stored in N_2-filled glass vials until use.

4.3.3 Catalyst characterization

The average Pd particle size and Pd dispersion were determined for each catalyst by CO chemisorption, using a Micrometrics Autochem ii 2920, equipped with a TCD detector. The catalyst was pretreated by heating in flowing H_2/Ar (10 vol%, 50 mL/min) to 200 °C at a ramp rate of 5 °C min^{-1}, and held at 200 °C for 2 h. After cooling to 35 °C under flowing He (50 mL/min), the catalyst was subjected to 20 pulses of CO (9.890 vol% in He). The amount of CO not adsorbed on each pulse was measured, and a Pd/CO chemisorption stoichiometry to 2 was assumed to calculate Pd dispersion.[44]

N_2 sorption isotherms were measured at 77 K using a 3 Flex Micrometrics porosimeter. Before measurement, each material was heated at 423 K for 8 h in flowing N_2 to remove physically adsorbed water. The apparent surface area was calculated using the Brunauer–Emmett–Teller (B.E.T.) equation, assuming a molecular area of 0.135 nm^2 for

adsorbed N_2.[45] The average pore diameter was calculated by analyzing the adsorption branch of the N_2 isotherm, using the Barrett–Joyner–Halenda (B.J.H.) method.

Powder X-ray diffraction patterns were acquired from 5 to 60 ° [2θ], using a Rigaku X-ray diffractometer equipped with Cu Kα radiation. TEM images were collected using a ThermoFisher Talos G2 200X TEM/STEM. To assess surface polarity, 20 mg catalyst was stirred with an aqueous solution of Prodan (30 μM, 5 mL) at room temperature overnight. After centrifugation at 3000 rpm for 10 min, the supernatant liquid was decanted and the solid was dried in air in an oven at 80 °C for 6 h. The fluorescence spectrum was recorded by dispersing ca. 5 mg catalyst in 4 mL water, using a Horiba FluoroMax 4 spectrometer and an excitation wavelength of 365 nm.

The amounts of adsorbed phenol were measured by mixing a sample of the catalyst (20 mg) with an aqueous solution of phenol (1.5 mL, 50 mM). The slurry was agitated in a IKA Vortex 4 digital mixer at 3000 rpm for 2 h, then centrifuged at 3000 rpm for 5 min to separate the solid. The decanted supernatant was analyzed by solution-state ^{1}H NMR (Varian Unity, 500 MHz). A shim map was created for H_2O solvent to use the H_2O peak as a standard without using other internal standards.

4.3.4 *Operando* MAS NMR spectroscopy

Magic-angle-spinning (MAS) NMR experiments were performed on a Bruker Avance NMR spectrometer equipped with an 11.7 T magnet and a 7.5 mm magic-angle spinning (MAS) triple resonance ^{1}H/X/Y probe. A specially-designed solid-state NMR rotor accommodates liquid-solid mixtures at high temperatures (<250 °C) and pressures (<225 bar).[22] The rotor bushing is constructed of Vespel and is equipped with Viton O-rings.

Calibration of the spectrometer temperature setting was performed by acquiring ^{1}H NMR spectra of ethylene glycol.[46] The rotor was loaded with phenol-1-^{13}C (6 mg), catalyst (3.8 mg), H_2O (120 μL), and H_2 (50 bar). The MAS rate was set and maintained at 3 kHz. When the desired temperature was reached, ^{13}C NMR spectra were collected until all the phenol was converted to cyclohexanol. Each spectrum was acquired with 8 scans, a relaxation delay of 25 ms, and an acquisition time of 30 s.

4.3.5 Kinetic Analyses

Kinetic profiles for phenol hydrogenation were obtained by integrating the phenol, cyclohexanone, and cyclohexanol peaks, at ca. 154, 219, and 69 ppm, respectively. Spectral deconvolution to quantify adsorbed amounts was conducted using the Bruker Biospin software TopSpin 4.1.1. A microkinetic model which assumed Langmuir-Hinshelwood dependence on the concentration of each species was proposed. The microkinetic model, which consisted of time dependent differential and algebraic equations, was fit to the kinetic profiles with nonlinear least squares regression in MATLAB.

4.4 Results and Discussion

4.4.1 Catalyst synthesis and characterization

Pd nanoparticles were formed on two mesoporous silicas: a hydrophilic (T, with oxygen linkers) and a hydrophobic (BP, with biphenylene linkers), by the incipient wetness impregnation method. The average pore size for BP is 5.3 nm, compared to 9.4 nm for T (Table A4.1 and Fig. A4.1). However, according to CO chemisorption, the Pd dispersion is 52 % for both materials (Table A4.2), corresponding to an average nanoparticle size of ca. 2.1

and 1.8 nm (assuming hemisphere and cubic shape). As expected for particles of this size, the wide-angle XRD pattern shows negligible intensity for the Pd(111) reflection at 2θ = ca. 40 ° (Fig. A4.2).[47,48] The TEM images of Pd-BP show nanoparticles of diameter (2.7 ± 0.5) nm (Fig. A4.3).

The surface polarity of the two supports was compared by measuring the fluorescence of adsorbed Prodan.[43,49] Its fluorescence is blue-shifted in less polar environments. Prodan was adsorbed from water onto both supports (without Pd) and both catalysts (with Pd). Fluorescence spectra were recorded after isolating each material and redispersing in water. Fig. 4.1 shows a large blue-shift in λ_{max} for BP (483 nm) compared to T (523 nm), confirming that the organosilica surface is much less polar than the silica surface. This result is consistent with a previous report.[43] Compared to polarity measurements of solvents made using Prodan dye,[39] the interfacial polarities of BP and T dispersed in water are deemed to be similar to those of 1-butanol and water, respectively.

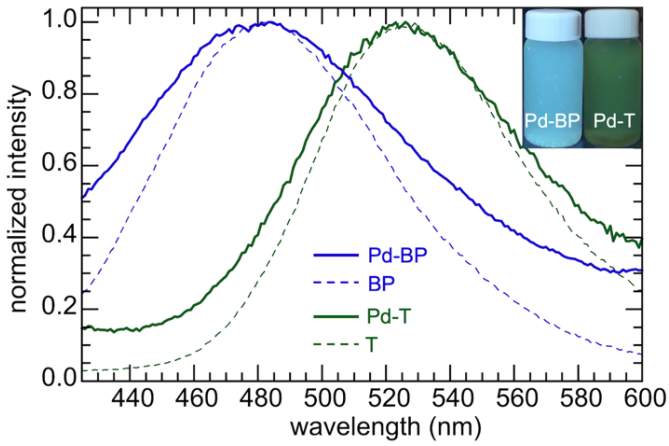

Fig. 4.1. Fluorescence of Prodan adsorbed on mesoporous supports (dashed lines) and Pd catalysts (solid lines). The inset shows a photograph of the Prodan fluorescence for Pd-BP and Pd-T, suspended in water.

The fluorescence of adsorbed Prodan was also measured for the Pd catalysts (inset to Fig. 4.1). The λ_{max} values are similar in the presence and absence of Pd, Fig. 4.1, indicating that the average surface polarity is not affected by Pd deposition. However, the fluorescence is broader in the presence of Pd nanoparticles. When BP was heated to 300 °C (as during the formation of the Pd nanoparticles), a similar broadening was observed (Fig. A4.4). Thus the effect appears to be caused not by the presence of Pd but by the thermal treatment steps.

Phenol adsorption was assessed for both supports (without Pd) and both catalysts (with Pd). Hydrophobic BP and Pd-BP adsorb ca. 7× more phenol (ca. 0.7 molecules/nm^2) than the corresponding hydrophilic support and catalyst (ca. 0.1 molecules/nm^2, Table 4.1). Although the dimensions of a phenol molecule (ca. 0.5 nm) are much smaller than the mesopore diameter, we confirmed that the smaller average pore size of BP and Pd-BP (ca. 5 nm) does not play a role in its increased affinity for phenol by conducting the same experiment with MCM-41 silica (average pore diameter 2.7 nm). It adsorbs a similar amount of phenol (0.09 molecule/nm^2) as T and Pd-T (average pore diameter ca. 9 nm). Thus the surface hydrophobicity as determined by the linker chemical composition, rather than the pore size, appears to be the major factor controlling phenol adsorption. Cyclohexanone adsorption was assessed for both catalysts as well. Hydrophobic Pd-BP adsorbs ca. 3× more cyclohexanone (0.87 molecules/nm^2) than hydrophilic Pd-T (0.28 molecules/nm^2). Thus, the hydrophobic surface show higher affinity to both phenol and cyclohexanone.

Table 4.1. Amounts of phenol and cyclohexanone adsorbed onto 20 mg solid from 1.5 mL of a 50 mM aqueous solution at room temperature

Materials	Phenol adsorbed (molecules/nm^2) [a]	Cyclohexanone adsorbed (molecules/nm^2) [a]
T	0.09	-
Pd-T	0.08	0.28
BP	0.67	-
Pd-BP	0.73	0.87
MCM-41	0.09	-

[a] B.E.T. Surface areas were used in calculating the density of adsorbed phenol by assuming an area for adsorbed N_2 of 0.135 nm^2/molecule.

A competitive adsorption test was conducted to investigate the relative affinities of each organic molecule for the two catalyst supports as a function of temperature. A mixture of phenol/cyclohexanone/cyclohexanol solution (70 mM each in water) was combined with each support. For BP, the fraction of adsorbed phenol decreased slightly from 14 % at room temperature to 12 % at 70 °C, while the fraction of adsorbed cyclohexanone increased from 17 to 25 % (Fig. A4.5a). Thus phenol adsorption (displacing adsorbed water) is nearly thermoneutral, while cyclohexanone adsorption is slightly endothermic (Fig. A4.6). For the T support, the fraction of phenol adsorbed is ca. 1-2 % at R.T and 70 °C, while the fraction of cyclohexanone adsorbed increases from 4 to 12 % (Fig. A4.5b). Again, these results confirm that BP has a higher adsorption capacity for both phenol and cyclohexanone than the T support.

4.4.2 Analysis of *operando* NMR spectra obtained from Pd-BP

The effect of surface hydrophobicity on phenol hydrogenation was studied using *operando* NMR spectroscopy. Fig. 4.2 shows a time-resolved array of ^{13}C MAS NMR spectra showing how an aqueous solution of phenol evolves in the presence of Pd-BP at 60 °C. Consistent with previous experimental and theoretical studies of heterogeneous Pd catalysts,[36–38] phenol is hydrogenated first to the intermediate cyclohexanone, which is then hydrogenated further to cyclohexanol. The peaks at 154, 219, and 69 ppm correspond to phenol-1-^{13}C, cyclohexanone-1-^{13}C and cyclohexanol-1-^{13}C, respectively. There is no evidence for scrambling of the ^{13}C label.

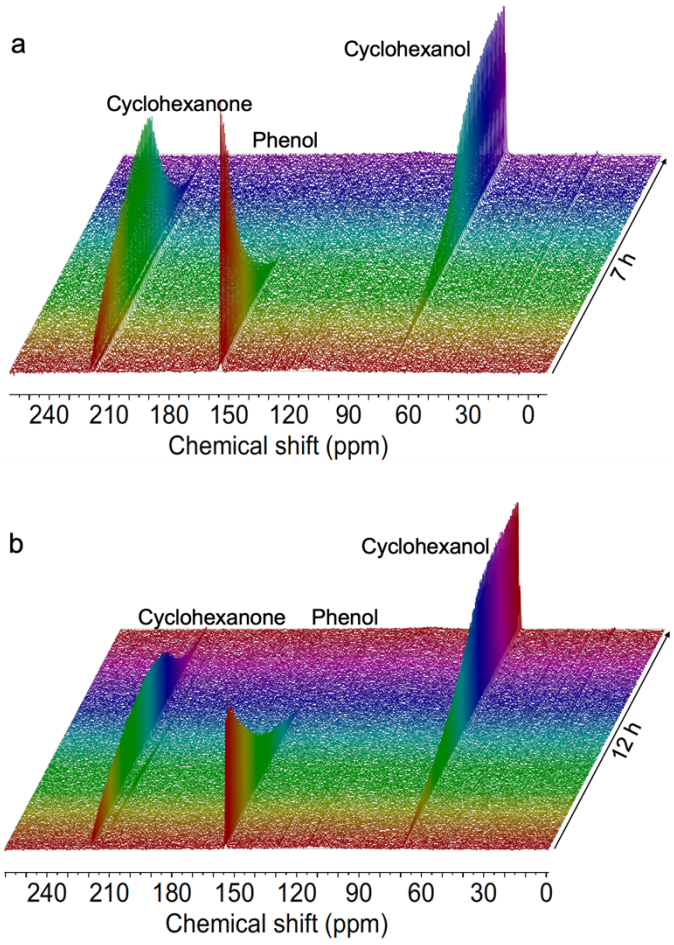

Fig. 4.2. Time-resolved *operando* ^{13}C MAS NMR spectra, showing phenol hydrogenation catalyzed by (a) Pd-BP and (b) Pd-T catalysts. Reaction conditions: catalyst 3.8 mg, H_2O 0.12 mL, phenol (1-^{13}C) 6 mg, H_2 50 bar (pressure at 23 °C), 60 °C. MAS 3 kHz.

Each region in the NMR spectral array is magnified in Fig. 4.3. For phenol-1-^{13}C, the solution phase peak at 154.2 ppm is accompanied by a downfield peak which emerges during the first two hours of reaction (Fig. 4.3a). It is assigned to adsorbed phenol due to its larger linewidth (see below). It shifts slightly and monotonically from ca. 154 to 155 ppm, before disappearing when phenol is completely converted. In the cyclohexanone region, the solution

phase peak at 219 ppm is accompanied by a well-separated, upfield peak (Fig. 4.3b). It appears at ca. 216 ppm, shortly after the beginning of the reaction. The chemical shift of this peak for adsorbed cyclohexanone changes in a more complex way: it decreases from 216 to 215 ppm in the first 2 h, then increases to 215.5 ppm over the next 2 h, before decreasing again, to 214 ppm at 5 h and finally disappearing. In the cyclohexanol region, the appearance of the solution phase cyclohexanol peak at 69 ppm is accompanied by an overlapping, upfield peak representing adsorbed cyclohexanol (Fig. 4.3c).

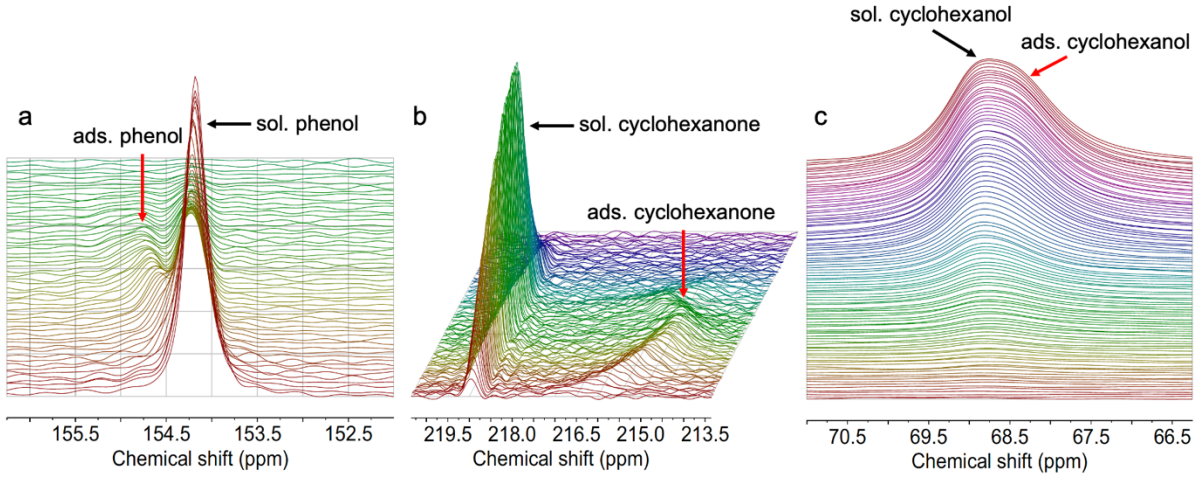

Fig. 4.3. *Operando* ^{13}C MAS NMR spectra showing details of regions for (a) phenol-1-^{13}C, (b) cyclohexanone-1-^{13}C, and (c)) cyclohexanol-1-^{13}C. Peaks for adsorbed species are indicated by the red arrows.

The ^{13}C NMR peaks were deconvoluted in order to measure their line widths, since increased line width is associated with reduced mobility, characteristic of adsorption. The width of the peak measured as the full width at half-maximum (FWHM) assigned to phenol adsorbed on Pd-BP is ca. 1.5× higher than that of the solution phase peak (Table A4.3). The width of the peak assigned to cyclohexanone adsorbed on Pd-BP is ca. 3× higher than the

corresponding solution-phase peak (Table A4.4). This indicates that the mobility of adsorbed cyclohexanone is lower than that of adsorbed phenol. Since cyclohexanone is less polar than phenol (relative polarities: cyclohexanone: 0.281, phenol: 0.701), cyclohexanone is expected to be less well solvated by water than phenol, and therefore to experience a stronger driving force to interact with the Pd-BP surface.

The peak positions of the adsorbed species change during the reaction (Fig. 4.3) due to shielding or deshielding of the nucleus, caused by changes in electron density, magnetic induction, or other factors. The chemical shifts of the adsorbed peaks reflect changes in the chemical composition of the adsorbed layer on the surface as the reaction proceeds. To investigate this effect further, the effect of solution-phase chemical composition on the ^{13}C NMR chemical shift of phenol-1-^{13}C was investigated. Fig. 4.4a shows that increasing phenol concentration from 0.05 to 0.4 M (compared to an initial concentration of 0.53 M in the *operando* experiment) has little effect less than 0.01 ppm on the chemical shift of the C_1 peak at ca. 155 ppm. In contrast, gradually increasing the cyclohexanone (0.15-0.45 M) or cyclohexanol (0.15-0.3 M) concentrations causes a monotonic shift downfield in the phenol peak (Fig. 4.4b), due to increasing extent of hydrogen-bonding interactions.[50,51] A mixture of all three species also results in a downfield chemical shift (Fig. 4.4b). These trends in the solution-phase chemical shift of phenol mirror those observed in the *operando* NMR array, where the chemical shift of adsorbed phenol moves downfield as the cyclohexanone or cyclohexanol concentration increases. However, the change in phenol chemical shift observed in the presence of cyclohexanone and/or cyclohexanol is an order of magnitude smaller for the solution-phase (ca. 0.04 ppm) compared to the sorbed phase (ca. 0.6 ppm). The change is

concentration-dependent, therefore the difference may be caused by a higher density of molecules on the surface, relative to the solution.

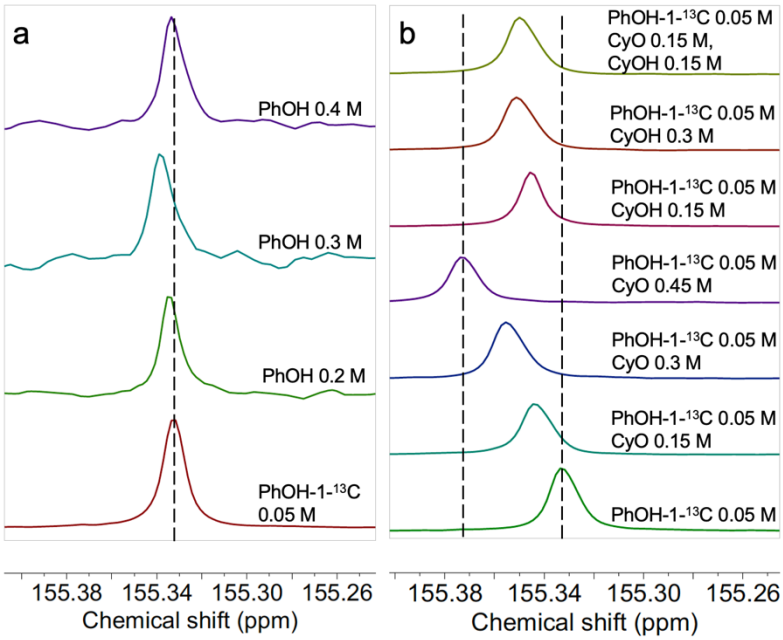

Fig. 4.4. Solution-state ^{13}C NMR spectra showing the effect of (a) phenol concentration, and (b) cyclohexanone/cyclohexanol concentration, on the phenol C_1 chemical shift.

To further investigate the effect of cyclohexanone/cyclohexanol on the chemical shift of adsorbed phenol, solid-state MAS NMR spectra were recorded for BP in contact with an aqueous solution of phenol-1-^{13}C (0.1 M), as well as phenol solutions containing cyclohexanone, cyclohexanol, and a mixture of the two (Fig. 4.5). A peak for adsorbed phenol (representing 52 % of the total intensity) is observed *upfield* (156.31 ppm) of the solution-phase peak at 156.36 ppm for the phenol-BP mixture (Fig. 4.5a). However, the peak moves *downfield* of the solution phase peak to 156.67 ppm when cyclohexanol (0.3 M) is also present in solution (Fig. 4.5b). Its fractional contribution to the intensity was increased from 52 to 55

% of the total. Deconvolution confirms a ca. 0.4 ppm increase in the chemical shift of adsorbed phenol in the presence of cyclohexanol (Fig. 4.5a, b). The intensity of the downfield shoulder is more pronounced in the presence of cyclohexanone (0.3 M), and the fraction of adsorbed phenol increases again, to 64 % with the chemical shift of 156.86 ppm (Fig. 4.5d). A phenol solution containing both cyclohexanone and cyclohexanol (0.15 M each) results in a downfield shoulder with an intermediate fractional intensity (58 %) and chemical shift (156.77 ppm, Fig. 4.5c). This result shows that phenol and cyclohexanone/cyclohexanol are not competitively adsorbed onto the surface, but adsorbed cyclohexanone/cyclohexanol contribute to the increase in phenol adsorption via a hydrogen bonding. Previous study that the enthalpy of phenol-cyclohexanone association found to be higher than that of phenol dimerization supports this adsorption results.[50] In addition, the trends in the chemical shift mirror the observations in the array of *operando* NMR spectra. Thus, co-adsorption of cyclohexanone and/or cyclohexanol causes deshielding of the 1-^{13}C signal of adsorbed phenol, as well as an increase in the amount of adsorbed phenol.

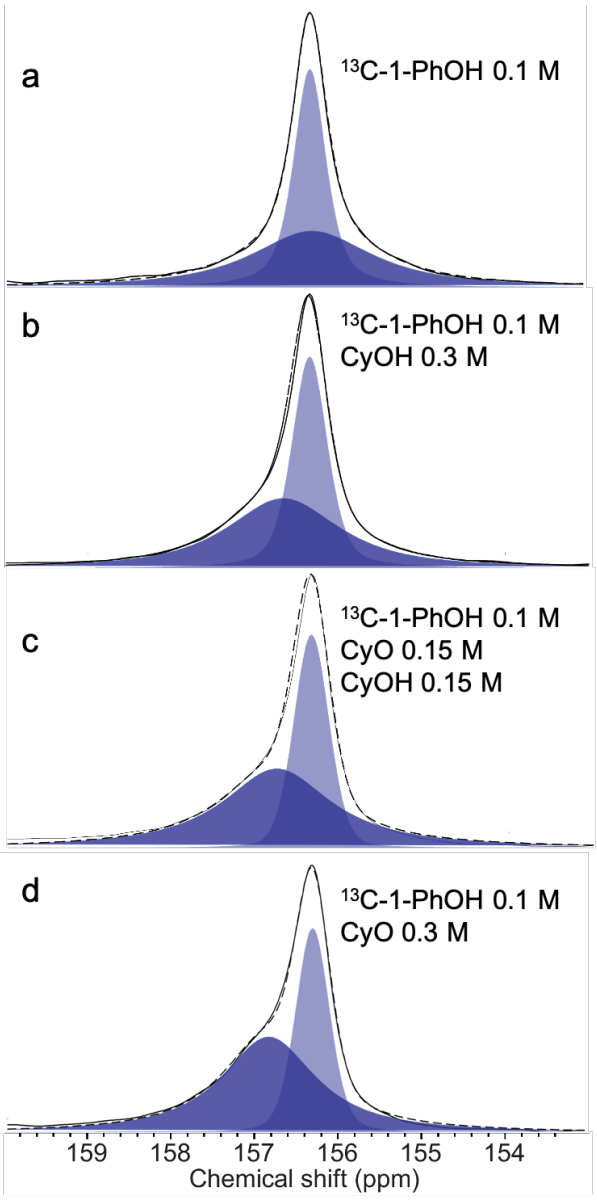

Fig. 4.5. ^{13}C MAS NMR spectra, showing the effect of solution chemical composition on the adsorption and chemical shift of phenol. An aqueous solution of phenol-1-^{13}C (0.1 M in 0.36 mL H_2O) was mixed with the organosilica (BP, 10 mg), in the (a) absence and (b-d) presence of cyclohexanol and/or cyclohexanone as indicated. Bright and dark portion spectra correspond to solution-phase and adsorbed-phase phenol. Solid and simulated lines are experimental and simulated spectra. Spectra were recorded at room temperature and 3 kHz MAS.

The effect of solution composition on the chemical shift of cyclohexanone in water was investigated in a similar fashion. In contrast to the negligible effect of phenol concentration on the phenol C_1 chemical shift, increasing the cyclohexanone concentration from 0.1 to 0.4 M causes a significant upfield shift of the C_1 peak (by ca. 0.12 ppm, Fig. 4.6a). Adding either phenol or cyclohexanol to the aqueous solution of cyclohexanone (0.1 M) led to a smaller upfield chemical shift of ca. 0.06 ppm (Fig. 4.6b, c). Previous literature showed that the NMR peak position of the carbonyl carbon shifts upfield when the surrounding of a ketone molecule becomes less polar.[52–54] Thus, these results suggest that the initial upfield shift of the peak for adsorbed cyclohexanone at the beginning of the reaction is caused mainly by the increasing surface concentration of adsorbed cyclohexanone. The subsequent downfield chemical shift of adsorbed cyclohexanone may be due to an increase in the amount of co-adsorbed cyclohexanol, which is more polar than cyclohexanone. The complex behavior of the peak for adsorbed cyclohexanone is discussed in the context of the kinetic profile in the next section.

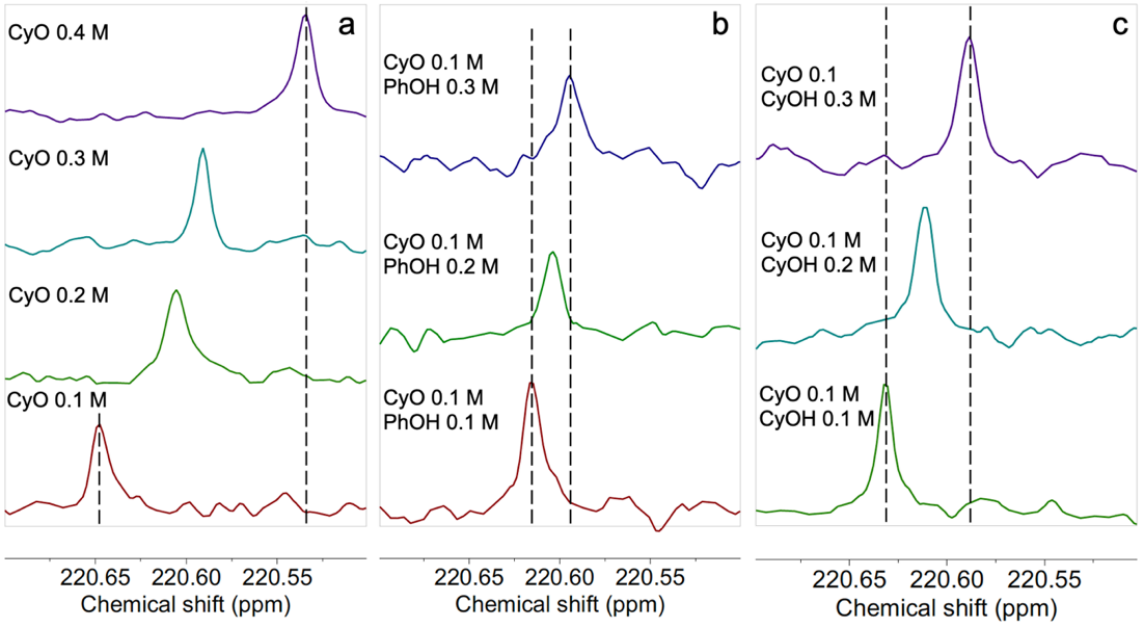

Fig. 4.6. Solution-state ^{13}C NMR spectra of cyclohexanone, showing the effect of (a) cyclohexanone concentration, (b) added phenol, and (c) added cyclohexanol, on the C_1 chemical shift.

4.4.3 Kinetics of phenol hydrogenation catalyzed by Pd-BP

Kinetic profiles were extracted from the array of NMR spectra by integration of all solution-phase and adsorbed-phase peaks. The time-dependent total concentrations (both phases) for each organic species are shown in Fig. 4.7. Phenol decreases monotonically, and nearly linearly, over ca. 3 h. Cyclohexanone is formed, reaching a broad plateau in concentration (ca. 0.35 M) from 2.8 to 3.8 h, then abruptly starting to decline and eventually disappearing after 6 h. The rate of cyclohexanol production is slower initially, then accelerates during the cyclohexanone plateau. These shapes indicate that cyclohexanone hydrogenation becomes much faster when it no longer competes with phenol for adsorption sites on the Pd nanoparticles.

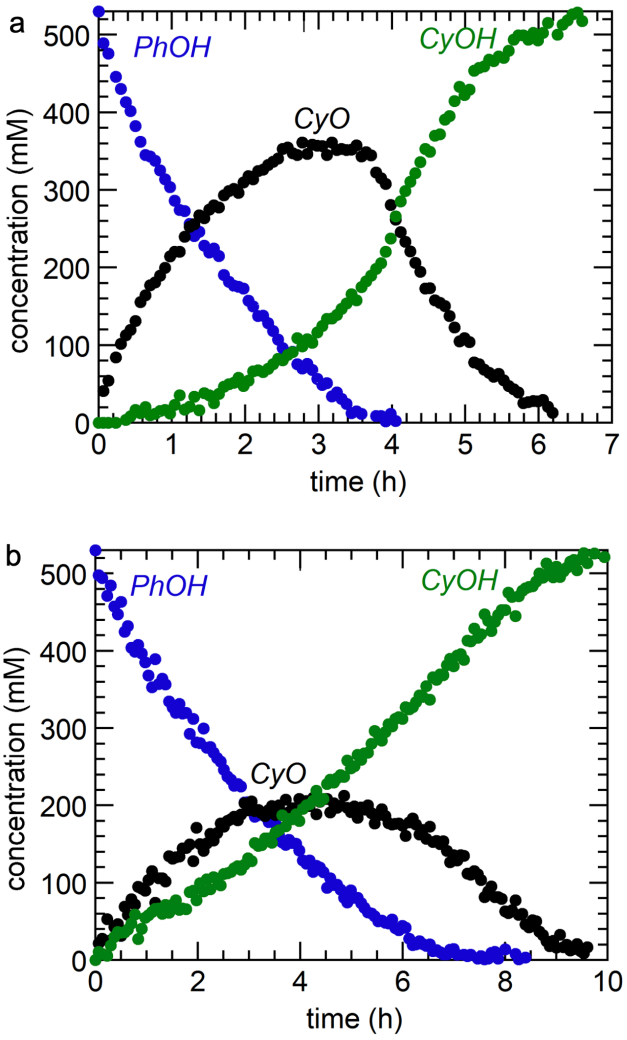

Fig. 4.7. Kinetic profiles for phenol hydrogenation catalyzed by (a) Pd-BP and (b) Pd-T catalysts obtained by integrating the *operando* ^{13}C NMR peaks representing both solution and adsorbed phases.

The cyclohexanone kinetic profile in the reaction catalyzed by Pd-BP was analyzed as separate solution and adsorbed contributions. The concentration profiles are quite distinct, Fig. 4.8. The amount of adsorbed cyclohexanone reaches a plateau and decreases slowly even as the amount of cyclohexanone in solution continues to increase. This suggests that adsorbed cyclohexanone molecules are hydrogenated due to decreasing phenol concentration on the

surface. More importantly, when all phenol has been converted, at 3.8 h, the concentration of cyclohexanone in solution decreases abruptly, while the concentration of adsorbed cyclohexanone decreases smoothly. This suggests that cyclohexanone in the solution phase adsorbs more rapidly on Pd active sites due to its higher mobility than cyclohexanone adsorbed on the support, as confirmed by the peak line widths (Table A4.4), in the absence of phenol.

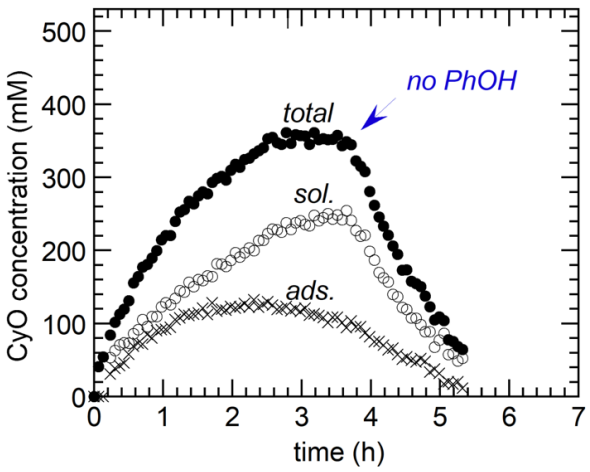

Fig. 4.8. Concentration profiles for cyclohexanone during phenol hydrogenation catalyzed by Pd-BP at 60°C: solution-phase, adsorbed, and total.

Fig. 4.9 shows the chemical shift profile of adsorbed cyclohexanone, superimposed on the kinetic profiles of adsorbed molecules. As briefly mentioned above, the chemical shift initially decreases, indicating the surrounding of cyclohexanone becomes less polar. This coincides with the rapid increase in adsorbed cyclohexanone concentration (consistent with the effect of concentration on chemical shift shown in Fig. 4.6). During this period (0 – 1.5 h), the surface layer is composed primarily of phenol and cyclohexanone, with the latter becoming dominant as the reaction proceeds. The chemical shift stabilizes at 2 h, and the

plateau in adsorbed cyclohexanone is reached, presumably because the effects of decreasing adsorbed phenol and increasing adsorbed cyclohexanone on the chemical shift are effectively equal and opposite. When the adsorbed cyclohexanone concentration decreases from 3 – 4 h, the chemical shift of adsorbed cyclohexanone increases again due to the appearance of adsorbed cyclohexanol, which is more polar than cyclohexanone. Finally, after phenol is completely consumed, the chemical shift decreases again despite the rapid decrease in cyclohexanone concentration, due to increased co-adsorption of cyclohexanol, which might displace polar, adsorbed water molecules.

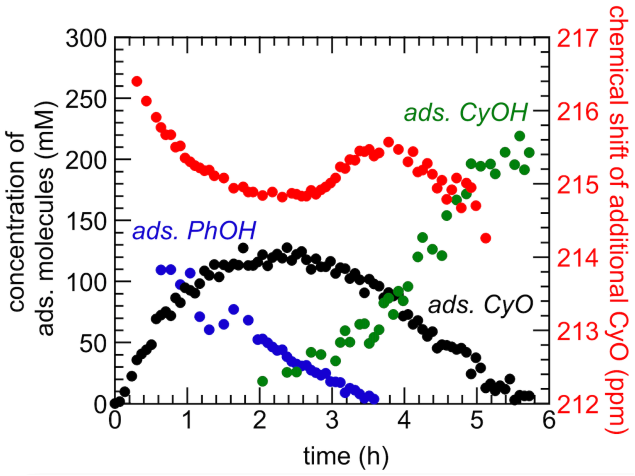

Fig. 4.9. Comparison of the time profile for the chemical shift for adsorbed cyclohexanone (right-hand ordinate) with kinetic profiles for adsorbed molecules during phenol hydrogenation.

4.4.4 Analysis of *operando* NMR spectra obtained using Pd-T

To assess the effect of surface polarity on activity and selectivity, polar Pd-T was used to catalyze phenol hydrogenation. ^{13}C MAS NMR spectra were collected under the same

reaction conditions. The same peaks are evident, and the reaction proceeds as with Pd-BP (Fig. 4.2b).

The regions containing the phenol, cyclohexanone, and cyclohexanol C_1 peaks are shown magnified in Fig. 4.10. Similar to the experiment with Pd-BP, the peak for adsorbed phenol-1-^{13}C appears at a higher chemical shift relative to the corresponding solution peak, Fig. 4.10a. The peak width for adsorbed phenol is 25 % larger than the solution-phase peak, Table A4.3, consistent with its reduced mobility. The peak position for adsorbed phenol shifts gradually downfield, from ca. 154.3 to 155.5 ppm, until phenol is fully consumed at ca. 6.5 h. The peak for adsorbed cyclohexanone becomes visible after 1.5 h, at a lower chemical shift than the solution-phase peak (Fig. 4.10b). Its peak width is only slightly higher (ca. 15 %, Table A4.4) than cyclohexanone in the solution phase, reflecting weak interaction with the polar surface. Over the next 6 h, it gradually shifts upfield from 214 ppm to 212 ppm, due to the increasing amounts of adsorbed cyclohexanone and cyclohexanol as the phenol concentration in solution decreases. The peak for adsorbed cyclohexanol is also observed at a lower chemical shift than the corresponding solution-phase peak (Fig. 4.10c).

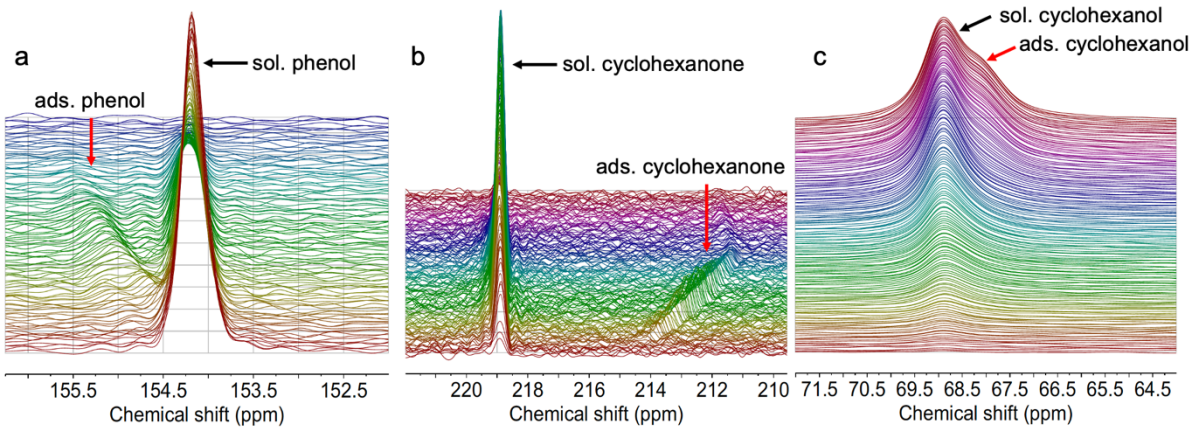

Fig. 4.10. *Operando* ^{13}C MAS NMR spectra, recorded during phenol hydrogenation over the Pd-T catalyst, showing magnified regions for (a) phenol-1-^{13}C, (b) cyclohexanone-1-^{13}C, and (c) cyclohexanol-1-^{13}C. Red arrows indicate peaks corresponding to adsorbed species.

The behavior of the peak for adsorbed phenol was further investigated by recording MAS NMR spectra for T immersed in various phenol/cyclohexanone/cyclohexanol solutions at room temperature. Compared to an aqueous solution of phenol-1-^{13}C (0.1 M, 0.36 mL), the addition of 10 mg T has little effect on the peak shape or position, suggesting that the concentration of adsorbed phenol is very low. However, a clear peak for adsorbed phenol is visible in the presence of cyclohexanol (0.3 M), Fig. 4.11a. The peak is shifted downfield by 0.9 ppm, and represents 25% of the total phenol present, according to spectral deconvolution. The same concentration of cyclohexanone causes a higher downfield shift (1.3 ppm, Fig. 4.11c), but a lower intensity (16% of total phenol). The dramatic changes in the adsorbed fraction of phenol in the presence of co-adsorbates suggest strongly cooperative interactions in the adsorbed layer. A mixture of cyclohexanol and cyclohexanone (0.15 M each) results in an intermediate intensity and chemical shift (Fig. 4.11b), although the latter is closer to the chemical shift of phenol co-adsorbed with cyclohexanone.

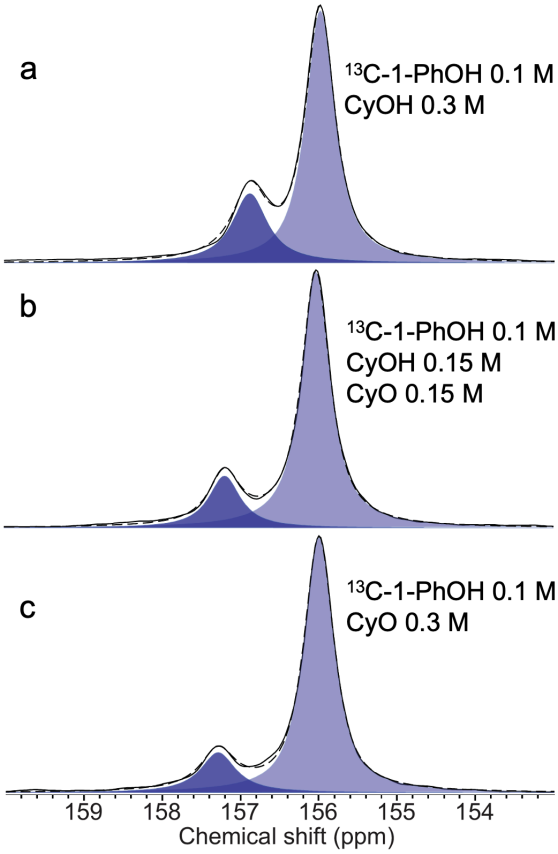

Fig. 4.11. ^{13}C MAS NMR spectra showing the effect of solution chemical composition on phenol adsorption on Pd-T. The concentration of phenol-1-^{13}C was fixed at 0.1 M while cyclohexanone/cyclohexanol concentrations were further varied as indicated in (a-c). Bright and dark portion spectra correspond to solution-phase and adsorbed-phase phenol. Solid and simulated lines are experimental and simulated spectra. In each experiment, 10 mg T was mixed with 0.36 mL aqueous solution. Spectra were recorded at room temperature with 3 kHz MAS.

4.4.5 Kinetics of phenol hydrogenation catalyzed by Pd-T

Kinetic profiles for the Pd-T catalyst were extracted from the ^{13}C MAS NMR spectral array by integrating peaks for both the solution and adsorbed phases. The time-dependent total concentrations (both phases) for each organic species are shown in Fig. 4.7b. The reaction catalyzed by Pd-T is significantly slower than the reaction catalyzed by Pd-BP. Furthermore, the shapes of the kinetic profiles differ. Phenol decreases monotonically and nearly linearly over ca. 7 h. Cyclohexanone is formed and reaches a very broad plateau in concentration (ca. 0.20 M) which lasts from 3-5 h. When it starts to decline, it does so gradually, eventually disappearing after 10 h. A small amount of cyclohexanol is formed rapidly in the first hour, then the rate slows briefly before accelerating again and staying approximately constant until the reaction is nearly complete. Interestingly, this experiment shows that the concentrations of all three components (phenol, cyclohexanone, and cyclohexanol) are approximately equal at ca. 3.5 h.

4.4.6 The fraction of adsorbed species on the support during the reactions

The main difference between the Pd-BP and Pd-T catalysts lies in their surface polarities, arising due to the presence of different (non-reactive) framework linkers. Pd-BP contains biphenylene linkers, which afford a less polar surface than Pd-T with oxygen linkers. Consequently, Pd-BP adsorbs much more phenol from an aqueous solution at room temperature (Table. 4.1 and Fig. A4.5). During phenol hydrogenation at 60 °C, the peak width is 23 % larger for phenol adsorbed on Pd-BP than on Pd-T (Table A4.3). Similarly, the peak width is about double for cyclohexanone adsorbed on Pd-BP compared to cyclohexanone adsorbed on Pd-T, Table A4.4. Thus the previous results suggest that both phenol and cyclohexanone interact more strongly with the Pd-BP surface during the reactions.

To further support the phenol/cyclohexanone interaction with the catalyst surfaces during the reactions, the fractions of adsorbed phenol and cyclohexanone present under reaction conditions were quantified by deconvoluting and integrating the signals for phenol in the adsorbed and solution phases separately. As expected, the adsorbed fractions of both species are higher for Pd-BP than for Pd-T (Fig. 4.12). The fraction of phenol adsorbed on Pd-BP is approx. constant at ca. 35 % in the period from 2-3 h when the peak is clearly visible, while the fraction of phenol adsorbed on Pd-T is only ca. 20 % in the interval from 2-5.5 h (Fig. 4.12a). Interestingly, the fractions appear to increase even as the phenol concentration in solution decreases, suggesting cooperative adsorption of phenol and cyclohexanone. The behavior of adsorbed cyclohexanone also shows evidence of cooperativity. The fraction of cyclohexanone adsorbed on Pd-BP increased to 40 % at 0.5 h, then decreased gradually to 30 % at 4 h (Fig. 4.12b). By contrast, the fraction of cyclohexanone adsorbed on Pd-T increased gradually to only ca. 10 % at 3 h, then declined until it became negligible when phenol was fully consumed at ca. 6 h, even though cyclohexanone was still present in the solution (and indeed was still in the plateau region, Fig. 4.7b).

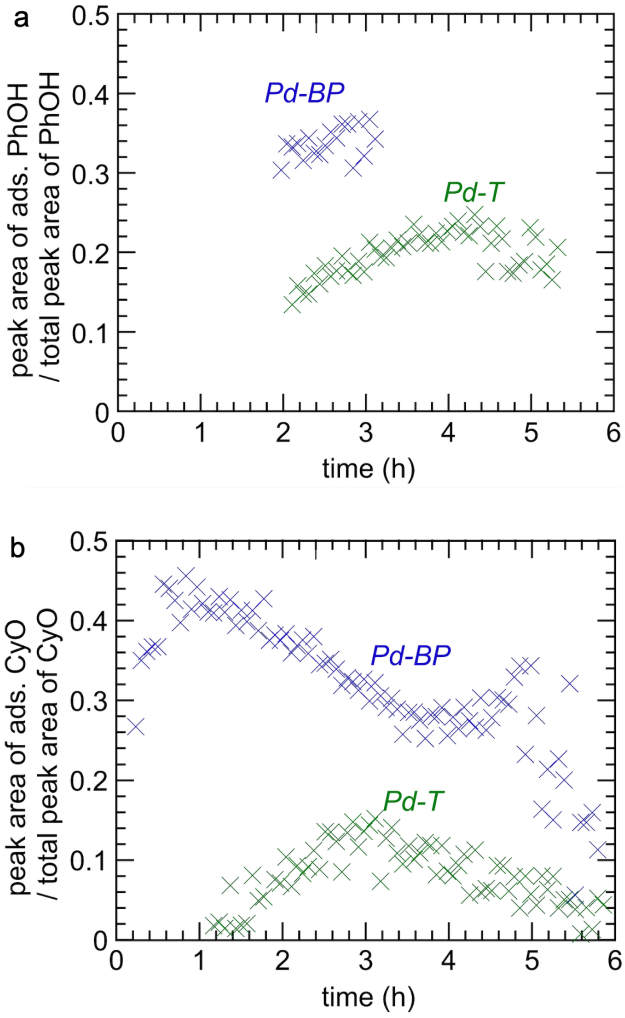

Fig. 4.12. Fractions of adsorbed species on Pd-BP and Pd-T under reaction conditions: (a) phenol, and (b) cyclohexanone, obtained from integrated peak areas in the *operando* ^{13}C MAS NMR spectra.

This result suggests that the adsorption equilibrium of cyclohexanone to the support surfaces changes with varying chemical composition during the reaction. In Fig. 4.5 and 4.11, it was shown that the fraction of adsorbed phenol also depends on the concentration of other species, indicating that the equilibrium constant of phenol to the support can be varied over

the reaction. Thus, these results suggest that simulating kinetic profiles precisely may require time-dependent equilibrium constants for phenol and cyclohexanone to the support surface.

4.4.7 Simulation study on the kinetics

The kinetic profiles reported above were analyzed through nonlinear least squares regression in MATLAB of a system of coupled differential and algebraic equations. The kinetic model assumes competitive Langmuir Hinshelwood adsorption isotherm behavior to Pd sites and is described in detail in Scheme A4.1. From the simulation, two equilibrium constants for the adsorption of phenol/cyclohexanone (K_{PhOH}, K_{CyO}), and their hydrogenation constants (k_{PhOH}, k_{CyO}) are obtained. The adsorption of cyclohexanol to Pd sites (K_{CyOH}) was not considered because its inclusion did not statistically improve the models. In addition, the adsorption of species onto the support is included because the amount of adsorption observed by *operando* NMR is significantly higher than what could be adsorbed on Pd active sites considering the Pd surface area is less than ca. 0.4 % of the total catalyst surface area. The population of species in solution and adsorbed on the catalyst support were assumed to be in equilibrium, and their relative amounts were fixed to the adsorbed/solution ratios which were calculated from the NMR data (Fig. A4.7, Table A4.5). In the Pd-BP model, the cyclohexanone adsorbed/solution ratio changes as a linear function of phenol in the system, as was found in Fig. A4.8.

Global fits to the kinetic profiles of Pd-BP and Pd-T are shown in Fig. 4.13 and the estimated parameters are presented in Table 4.2. On the Pd-BP catalyst, the disappearance of phenol is close to linear, which suggests phenol strongly adsorbs to the Pd active sites. In contrast, the disappearance of cyclohexanone resembles pseudo-first order behavior,

suggesting weaker cyclohexanone adsorption to Pd. This observation is supported by the parameter estimation results, which found K_{PhOH} = 780 ± 120 mmol^{-1} while K_{CyO} = 120 ± 30 mmol^{-1}. The first order rate constants for phenol hydrogenation, k_{PhOH} = 2.2 ± 0.1 min^{-1}, and cyclohexanone hydrogenation, k_{CyO}= 2.5 ± 0.2 min^{-1}, are similar. Thus, the competing rates of phenol and cyclohexanone hydrogenation (and the cyclohexanone selectivity) are more strongly influenced by the adsorption affinity to Pd active sites, than by the surface hydrogenation rates.

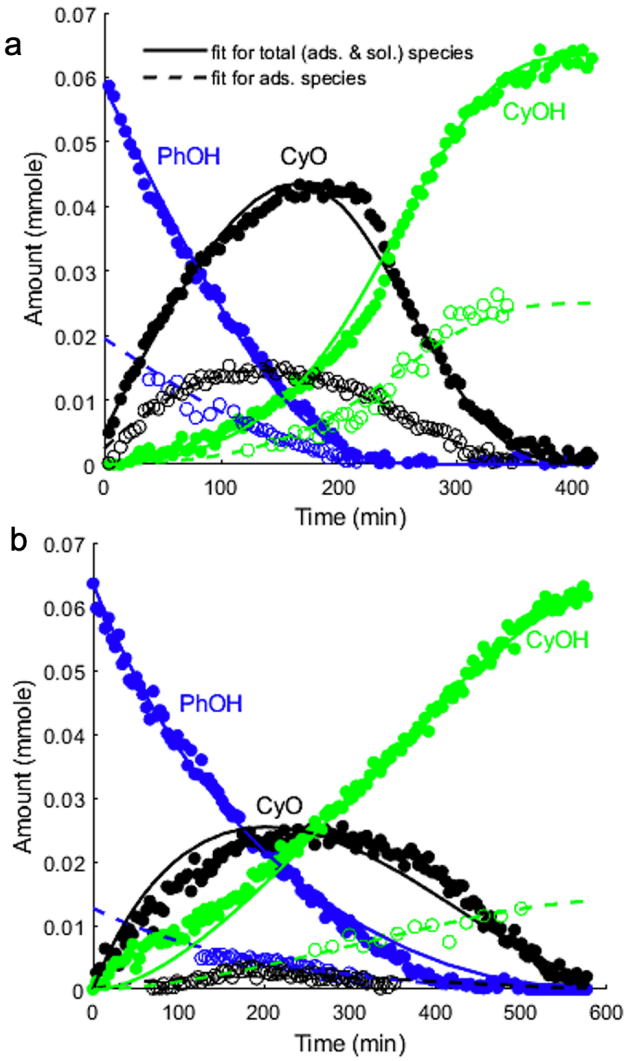

Fig. 4.13. Kinetic profiles and global fits for PhOH hydrogenation solved through nonlinear regression on a) Pd-BP and b) Pd-T.

Table 4.2. Kinetic parameters estimated through nonlinear least-squares regression of Pd-BP and Pd-T kinetic profiles. Values in parenthesis indicate 95% confidence intervals.

Materials	K_{PhOH} ($mmol^{-1}$)	K_{CyO} ($mmol^{-1}$)	K_{PhOH}/K_{CyO}	k_{PhOH} (min^{-1})	k_{CyO} (min^{-1})
Pd-BP	780 ± 120	120 ± 30	6.5	2.2 ± 0.1	2.5 ± 0.2
Pd-T	74 ± 18	99 ± 37	0.7	2.4 ± 0.1	1.5 ± 0.2

When phenol hydrogenation is compared between the Pd-BP and Pd-T catalysts, it is evident the catalyst polarity affects the overall rate and product selectivity. On Pd-T, the phenol hydrogenation rate is significantly slower than on Pd-BP because it takes an additional 3.5 h to reach 100 % conversion of phenol. The rates of phenol hydrogenation are similar (Table 4.2), however, the K_{PhOH} is approximately 10× larger on Pd-BP than Pd-T. Thus, the hydrophobic surface appears to enhance the ability of phenol to adsorb to Pd sites. This difference in the phenol affinity for the Pd sites not only affects the rate, but also the selectivity of the intermediate product. When $K_{PhOH} > K_{CyO}$, as is the case on Pd-BP, phenol will outcompete cyclohexanone for the Pd sites. This results in enhanced cyclohexanone selectivity compared to the conditions where $K_{PhOH} \approx K_{CyO}$, in which cyclohexanone will more efficiently compete with phenol for Pd sites. Indeed, on Pd-BP, where K_{PhOH}/K_{CyO}=6.5, the maximum cyclohexanone yield is ~1.8× greater than on Pd-T where K_{PhOH}/K_{CyO}=0.7.

4.4.8 Comparison between Pd-BP and Pd-T

The higher phenol hydrogenation rate observed from Pd-BP compared to Pd-T is considered due to enhanced phenol-support surface interaction, and subsequent facile

adsorption onto Pd metal surface as confirmed from 10× higher K_{PhOH}. Another difference in the two kinetic profiles (Figs. 4.7) are the maximum cyclohexanone concentration and the shape of the cyclohexanone concentration profile. The cyclohexanone concentration over Pd-T exhibits a broad maximum at 0.20 M; phenol and cyclohexanone hydrogenation occur concurrently. In contrast, the maximum cyclohexanone concentration achieved using Pd-BP was ca. 0.35 M, and cyclohexanone hydrogenation accelerates abruptly when phenol is fully converted. This dramatic decrease in cyclohexanone concentration is due to 6.5 times higher K_{PhOH} than K_{CyO}, which is possibly due to the increased affinity of the Pd-BP support surface for phenol. In addition, too low mobility of adsorbed cyclohexanone on Pd-BP might retard the facile adsorption of adsorbed cyclohexanone onto the Pd surface. The ca. two times higher values of peak line width of adsorbed cyclohexanone (ca. 180 Hz) than adsorbed phenol (ca. 100 Hz) indicates lower mobility of adsorbed cyclohexanone than adsorbed phenol. As previously shown in the cyclohexanone kinetic profile of Pd-BP (Fig. 4.8), the cyclohexanone concentration in the solution-phase rapidly decreases, while the concentration of adsorbed cyclohexanone smoothly decreases, indicating adsorbed cyclohexanone are not rapidly adsorbed onto the Pd metal surface. This result might suggests that intermediate strength of interaction between a reactant and support surface is desired to improve the reactant adsorption onto active sites. Finally, the cooperative adsorption via an enhanced hydrogen bond interaction between adsorbed phenol and cyclohexanone on the Pd-BP compared with Pd-T surface, as confirmed by Fig. 4.5d and Fig. 4.11c, might further stabilize the adsorbed cyclohexanone. This inhibits its adsorption onto the Pd active sites, resulting in the increased cyclohexanone selectivity for the Pd-BP compared to the Pd-T catalyst.

4.5 Conclusion

Operando MAS NMR spectroscopy can provide detailed information on the partitioning of species between the solution and the catalyst during the reaction. The extent of chemical shift and fraction of adsorbed molecules are affected by the surface polarity as well as the chemical composition on the surface (i.e., the relative amounts of phenol, cyclohexanone, and cyclohexanol). A higher amount of adsorbed phenol and phenol hydrogenation rate were observed for Pd-BP than Pd-T catalyst. Kinetic analysis shows that K_{PhOH} of Pd-BP is ca. 10 times higher than that of Pd-T, and ca. 6.5 times higher than K_{CyO} of Pd-BP. These results might suggest that an increased phenol concentration on Pd-BP surface leads to the increased phenol around the Pd active sites, inhibiting cyclohexanone adsorption onto the Pd active sites. The retarded mobility of adsorbed cyclohexanone and stabilized adsorbed cyclohexanone via a hydrogen bond with adsorbed phenol on the Pd-BP surface might further contribute to the relative increase in phenol adsorption on to the Pd surface, resulting in higher cyclohexanone selectivity. By contrast, Pd-T has a lower affinity for phenol, and shows lower cyclohexanone selectivity. Thus, the results suggest that the affinity of the support for the reactant, the mobility of adsorbed reactants, and the interaction between chemical species on the surface might be critical factors in determining activity and selectivity.

The next chapter will describe other factors affecting molecular adsorption onto Pd active sites and support surfaces, such as reaction temperature and solvent type. The outcome will eventually provide insight to identify factors that create ideal reaction conditions for various aromatic hydrogenation reactions.

4.6 References

(1) Tuck, C. O.; Perez, E.; Horvath, I. T.; Sheldon, R. A.; Poliakoff, M. Valorization of Biomass: Deriving More Value from Waste. *Science* **2012**, *337* (6095), 695–699.

(2) Briens, C.; Piskorz, J.; Berruti, F. Biomass Valorization for Fuel and Chemicals Production -- A Review. *J. Chem. React. Eng. 6* (1).

(3) Liao, Y.; Koelewijn, S.-F.; Van den Bossche, G.; Van Aelst, J.; Van den Bosch, S.; Renders, T.; Navare, K.; Nicolaï, T.; Van Aelst, K.; Maesen, M.; Matsushima, H.; Thevelein, J. M.; Van Acker, K.; Lagrain, B.; Verboekend, D.; Sels, B. F. A Sustainable Wood Biorefinery for Low–Carbon Footprint Chemicals Production. *Science* **2020**, *367* (6484), 1385–1390.

(4) Lin, Y.-C.; Huber, G. W. The Critical Role of Heterogeneous Catalysis in Lignocellulosic Biomass Conversion. *Energy Environ. Sci.* **2009**, *2* (1), 68–80.

(5) Sun, Z.; Fridrich, B.; de Santi, A.; Elangovan, S.; Barta, K. Bright Side of Lignin Depolymerization: Toward New Platform Chemicals. *Chem. Rev.* **2018**, *118* (2), 614–678.

(6) Pagán-Torres, Y. J.; Wang, T.; Gallo, J. M. R.; Shanks, B. H.; Dumesic, J. A. Production of 5-Hydroxymethylfurfural from Glucose Using a Combination of Lewis and Brønsted Acid Catalysts in Water in a Biphasic Reactor with an Alkylphenol Solvent. *ACS Catal.* **2012**, *2* (6), 930–934.

(7) Wettstein, S. G.; Alonso, D. M.; Chong, Y.; Dumesic, J. A. Production of Levulinic Acid and Gamma-Valerolactone (GVL) from Cellulose Using GVL as a Solvent in Biphasic Systems. *Energy Environ. Sci.* **2012**, *5* (8), 8199.

(8) Sener, C.; Motagamwala, A. H.; Alonso, D. M.; Dumesic, J. A. Enhanced Furfural Yields from Xylose Dehydration in the γ-Valerolactone/Water Solvent System at Elevated Temperatures. *ChemSusChem* **2018**, *11* (14), 2321–2331.

(9) Chen, X.; Qian, P.; Zhang, T.; Xu, Z.; Fang, C.; Xu, X.; Chen, W.; Wu, P.; Shen, Y.; Li, S.; Wu, J.; Zheng, B.; Zhang, W.; Huo, F. Catalyst Surfaces with Tunable Hydrophilicity and Hydrophobicity: Metal–Organic Frameworks toward Controllable Catalytic Selectivity. *Chem. Commun.* **2018**, *54* (32), 3936–3939.

(10) Hao, P.; Schwartz, D. K.; Medlin, J. W. Effect of Surface Hydrophobicity of Pd/Al_2O_3 on Vanillin Hydrodeoxygenation in a Water/Oil System. *ACS Catal.* **2018**, *8* (12), 11165–11173.

(11) Jin, Z.; Wang, L.; Hu, Q.; Zhang, L.; Xu, S.; Dong, X.; Gao, X.; Ma, R.; Meng, X.; Xiao, F.-S. Hydrophobic Zeolite Containing Titania Particles as Wettability-Selective Catalyst for Formaldehyde Removal. *ACS Catal.* **2018**, *8* (6), 5250–5254.

(12) Liu, F.; Huang, K.; Zheng, A.; Xiao, F.-S.; Dai, S. Hydrophobic Solid Acids and Their Catalytic Applications in Green and Sustainable Chemistry. *ACS Catal.* **2018**, *8* (1), 372–391.

(13) Wang, C.; Liu, Z.; Wang, L.; Dong, X.; Zhang, J.; Wang, G.; Han, S.; Meng, X.; Zheng, A.; Xiao, F.-S. Importance of Zeolite Wettability for Selective Hydrogenation of Furfural over Pd@Zeolite Catalysts. *ACS Catal.* **2018**, *8* (1), 474–481.

(14) Li, Y.; Hu, X.; Liu, X.; Zhang, Y.; Zhao, Q.; Ning, P.; Tian, S. Adsorption Behavior of Phenol by Reversible Surfactant-Modified Montmorillonite: Mechanism, Thermodynamics, and Regeneration. *Chem. Eng. J.* **2018**, *334*, 1214–1221.

(15) Jin, Z.; Wang, L.; Zuidema, E.; Mondal, K.; Zhang, M.; Zhang, J.; Wang, C.; Meng, X.; Yang, H.; Mesters, C.; Xiao, F.-S. Hydrophobic Zeolite Modification for in Situ Peroxide Formation in Methane Oxidation to Methanol. *Science* **2020**, *367* (6474), 193–197.

(16) Zhang, W.; Xu, S.; Han, X.; Bao, X. In Situ solid-State NMR for Heterogeneous Catalysis: A Joint Experimental and Theoretical Approach. *Chem. Soc. Rev.* **2012**, *41* (1), 192–210.

(17) Moore, J. K.; Sakwa-Novak, M. A.; Chaikittisilp, W.; Mehta, A. K.; Conradi, M. S.; Jones, C. W.; Hayes, S. E. Characterization of a Mixture of CO_2 Adsorption Products in Hyperbranched Aminosilica Adsorbents by ^{13}C Solid-State NMR. *Environ. Sci. Technol.* **2015**, *49* (22), 13684–13691.

(18) Jaegers, N. R.; Mueller, K. T.; Wang, Y.; Hu, J. Z. Variable Temperature and Pressure Operando MAS NMR for Catalysis Science and Related Materials. *Acc. Chem. Res.* **2020**, *53* (3), 611–619.

(19) Thursfield, A.; Anderson, M. W. ^{1}H, ^{2}H, and ^{13}C Solid-State NMR Studies of Methanol Adsorbed on a Series of Acidic Microporous Zeotype Materials. *J. Phys. Chem.* **1996**, *100* (16), 6698–6707.

(20) Qi, L.; Alamillo, R.; Elliott, W. A.; Andersen, A.; Hoyt, D. W.; Walter, E. D.; Han, K. S.; Washton, N. M.; Rioux, R. M.; Dumesic, J. A.; Scott, S. L. Operando Solid-State NMR Observation of Solvent-Mediated Adsorption-Reaction of Carbohydrates in Zeolites. *ACS Catal.* **2017**, *7* (5), 3489–3500.

(21) Qi, L.; Chamas, A.; Jones, Z. R.; Walter, E. D.; Hoyt, D. W.; Washton, N. M.; Scott, S. L. Unraveling the Dynamic Network in the Reactions of an Alkyl Aryl Ether Catalyzed by Ni/γ-Al_2O_3 in 2-Propanol. *J. Am. Chem. Soc.* **2019**, *141* (43), 17370–17381.

(22) Walter, E. D.; Qi, L.; Chamas, A.; Mehta, H. S.; Sears, J. A.; Scott, S. L.; Hoyt, D. W. *Operando* MAS NMR Reaction Studies at High Temperatures and Pressures. *J. Phys. Chem. C* **2018**, *122* (15), 8209–8215.

(23) Jiang, G.; Nowakowski, D. J.; Bridgwater, A. V. Effect of the Temperature on the Composition of Lignin Pyrolysis Products. *Energy Fuels* **2010**, *24* (8), 4470–4475.

(24) Fierro, V.; Torné-Fernández, V.; Montané, D.; Celzard, A. Adsorption of Phenol onto Activated Carbons Having Different Textural and Surface Properties. *Micropor. Mesopor. Mat.* **2008**, *111* (1–3), 276–284.

(25) Stavropoulos, G. G.; Samaras, P.; Sakellaropoulos, G. P. Effect of Activated Carbons Modification on Porosity, Surface Structure and Phenol Adsorption. *J. Hazard. Mater.* **2008**, *151* (2–3), 414–421.

(26) Wang, X.; Zhu, S.; Wang, S.; Wang, J.; Fan, W.; Lv, Y. Ni Nanoparticles Entrapped in Nickel Phyllosilicate for Selective Hydrogenation of Guaiacol to 2-Methoxycyclohexanol. *Appl. Catal. A: Gen.* **2018**, *568*, 231–241.

(27) Yang, F.; Libretto, N. J.; Komarneni, M. R.; Zhou, W.; Miller, J. T.; Zhu, X.; Resasco, D. E. Enhancement of *m* -Cresol Hydrodeoxygenation Selectivity on Ni Catalysts by Surface Decoration of MoO_x Species. *ACS Catal.* **2019**, *9* (9), 7791–7800.

(28) Fache, M.; Boutevin, B.; Caillol, S. Vanillin Production from Lignin and Its Use as a Renewable Chemical. *ACS Sustainable Chem. Eng.* **2016**, *4* (1), 35–46.

(29) Lin, C.-J.; Huang, S.-H.; Lai, N.-C.; Yang, C.-M. Efficient Room-Temperature Aqueous-Phase Hydrogenation of Phenol to Cyclohexanone Catalyzed by Pd Nanoparticles Supported on Mesoporous MMT-1 Silica with Unevenly Distributed Functionalities. *ACS Catal.* **2015**, *5* (7), 4121–4129.

(30) Wang, Y.; Yao, J.; Li, H.; Su, D.; Antonietti, M. Highly Selective Hydrogenation of Phenol and Derivatives over a Pd@Carbon Nitride Catalyst in Aqueous Media. *J. Am. Chem. Soc.* **2011**, *133* (8), 2362–2365.

(31) Li, Y.; Xu, X.; Zhang, P.; Gong, Y.; Li, H.; Wang, Y. Highly Selective Pd@mpg-C3N4 Catalyst for Phenol Hydrogenation in Aqueous Phase. *RSC Adv.* **2013**, *3* (27), 10973–10982.

(32) Neri, G.; Visco, A. M.; Donato, A.; Milone, C.; Malentacchi, M.; Gubitosa, G. Hydrogenation of Phenol to Cyclohexanone over Palladium and Alkali-Doped Palladium Catalysts. *Appl. Catal. A: Gen.* **1994**, *110* (1), 49–59.

(33) Li, H.; Liu, J.; Xie, S.; Qiao, M.; Dai, W.; Lu, Y.; Li, H. Vesicle-Assisted Assembly of Mesoporous Ce-Doped Pd Nanospheres with a Hollow Chamber and Enhanced Catalytic Efficiency. *Adv. Funct. Mater.* **2008**, *18* (20), 3235–3241.

(34) Mahata, N.; Vishwanathan, V. Influence of Palladium Precursors on Structural Properties and Phenol Hydrogenation Characteristics of Supported Palladium Catalysts. *J. Catal.* **2000**, *196* (2), 262–270.

(35) Nelson, N. C.; Manzano, J. S.; Sadow, A. D.; Overbury, S. H.; Slowing, I. I. Selective Hydrogenation of Phenol Catalyzed by Palladium on High-Surface-Area Ceria at Room Temperature and Ambient Pressure. *ACS Catal.* **2015**, *5* (4), 2051–2061.

(36) Talukdar, A. K.; Bhattacharyya, K. G.; Sivasanker, S. Hydrogenation of Phenol over Supported Platinum and Palladium Catalysts. *Appl. Catal. A: Gen.* **1993**, *96* (2), 229–239.

(37) Li, G.; Han, J.; Wang, H.; Zhu, X.; Ge, Q. Role of Dissociation of Phenol in Its Selective Hydrogenation on Pt(111) and Pd(111). *ACS Catal.* **2015**, *5* (3), 2009–2016.

(38) Liu, Z.; Hamad, I. A.; Li, Y.; Chen, Y.; Wang, S.; Jentoft, R. E.; Jentoft, F. C. Poisoning and Competitive Adsorption Effects during Phenol Hydrogenation on Platinum in Water-Alcohol Mixtures. *Appl. Catal. A: Gen.* **2019**, *585*, 117199.

(39) Catalan, J.; Perez, P.; Laynez, J.; Blanco, F. G. Analysis of the Solvent Effect on the Photophysics Properties of 6-Propionyl-2-(Dimethylamino)Naphthalene (PRODAN). *J Fluoresc* **1991**, *1* (4), 215–223.

(40) Singappuli-Arachchige, D.; Manzano, J. S.; Sherman, L. M.; Slowing, I. I. Polarity Control at Interfaces: Quantifying Pseudo-Solvent Effects in Nano-Confined Systems. *ChemPhysChem* **2016**, *17* (19), 2982–2986.

(41) Zhao, D.; Feng, J.; Huo, Q.; Melosh, N.; Fredrickson, G. H.; Chmelka, B. F.; Stucky, G. D. Triblock Copolymer Syntheses of Mesoporous Silica with Periodic 50 to 300 Angstrom Pores. *Science* **1998**, *279* (5350), 548–552.

(42) Yang, Y.; Sayari, A. Molecularly Ordered Biphenyl-Bridged Mesoporous Organosilica Prepared under Acidic Conditions. *Chem. Mater.* **2007**, *19* (17), 4117–4119.

(43) Moon, H.; Han, S.; Scott, S. L. Tuning Molecular Adsorption in SBA-15-Type Periodic Mesoporous Organosilicas by Systematic Variation of Their Surface Polarity. *Chem. Sci.* **2020**, *11* (14), 3702–3712.

(44) Canton, P.; Fagherazzi, G.; Battagliarin, M.; Menegazzo, F.; Pinna, F.; Pernicone, N. Pd/CO Average Chemisorption Stoichiometry in Highly Dispersed Supported Pd/γ-Al $_2$ O $_3$ Catalysts. *Langmuir* **2002**, *18* (17), 6530–6535.

(44) Jelinek, L.; sz. Kovats, E. True Surface Areas from Nitrogen Adsorption Experiments. *Langmuir* **1994**, *10* (11), 4225–4231.

(45) Ammann, C.; Meier, P.; Merbach, A. A Simple Multinuclear NMR Thermometer. *J. Magn. Reson.* **1982**, *46* (2), 319–321.

(47) Amorim, C.; Keane, M. A. Palladium Supported on Structured and Nonstructured Carbon: A Consideration of Pd Particle Size and the Nature of Reactive Hydrogen. *J. Colloid Interface Sci.* **2008**, *322* (1), 196–208.

(48) Wojcieszak, R.; Genet, M. J.; Eloy, P.; Ruiz, P.; Gaigneaux, E. M. Determination of the Size of Supported Pd Nanoparticles by X-Ray Photoelectron Spectroscopy. Comparison with X-Ray Diffraction, Transmission Electron Microscopy, and H_2 Chemisorption Methods. *J. Phys. Chem. C* **2010**, *114* (39), 16677–16684.

(49) Singappuli-Arachchige, D.; Kobayashi, T.; Wang, Z.; Burkhow, S. J.; Smith, E. A.; Pruski, M.; Slowing, I. I. Interfacial Control of Catalytic Activity in the Aldol Condensation: Combining the Effects of Hydrophobic Environments and Water. *ACS Catal.* **2019**, *9* (6), 5574–5582.

(50) Jeng, M.-L. H.; Li, Y.-S. Hydrogen Bonding Interactions of Phenol with Cyclic Ketones. *Spectrochimica Acta Part A: Molecular Spectroscopy* **1989**, *45* (5), 525–531.

(51) Castola, V.; Mazzoni, V.; Corticchiato, M.; Bighelli, A.; Casanova, J. Hydrogen Bonding Effect on Carbon-13 NMR Chemical Shifts of Naturally Occurring Phenols. *Can. J. Anal. Sci. Spectrosc.* **1997**, *42*, 90–94.

(52) Hiraga, Y.; Chaki, S.; Niwayama, S. 13C NMR Spectroscopic Studies of the Behaviors of Carbonyl Compounds in Various Solutions. *Tetrahedron Lett.* **2017**, *58* (50), 4677–4681.

(53) Faska, N.; Auhmani, A.; Esseffar, M. Solvent Effects on 13C and 1H NMR Shielding of Cyclic Ketones: An Experimental and Theoretical Study. *J. Mol. Struct-Thermochem* **2007**, *811* (1–3), 203–213.

(54) Kashid, S. M.; Bagchi, S. Experimental Determination of the Electrostatic Nature of Carbonyl Hydrogen-Bonding Interactions Using IR-NMR Correlations. *J. Phys. Chem. Lett.* **2014**, *5* (18), 3211–3215.

4.7 Appendix III

Table A4.1. Comparison of physicochemical properties of hydrophilic (Pd-T) and hydrophobic (Pd-BP) Pd catalysts

	B.E.T. surface area (m^2/g)	Pore volume (cm^3/g)	Pore size (nm)	Surface OH (mmol/g)	Surface OH ($/nm^2$)	Pd content (w%)
Pd-BP	607	1.30	5.3	0.9	1.1	0.95
Pd-T	785	1.28	9.4	1.3	1.0	0.94

Table A4.2. Dispersion and nanoparticle sizes of Pd-BP and Pd-T catalysts

		Pd/CO = 2	
	Dispersion (%)	Hemisphere (nm)	Cubic (nm)
Pd-BP	52.4	2.1	1.8
Pd-T	51.5	2.2	1.8

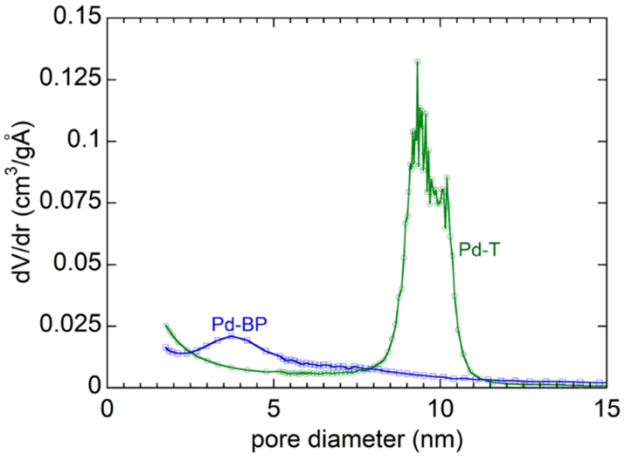

Fig. A4.1. The pore size distribution of Pd-T and Pd-BP. Pd-BP has a wider pore size distribution than Pd-T, since the synthesis of biphenylene-bridged silica support involves the use of 1-butanol as a co-surfactant in order to enable a mesophase formation.

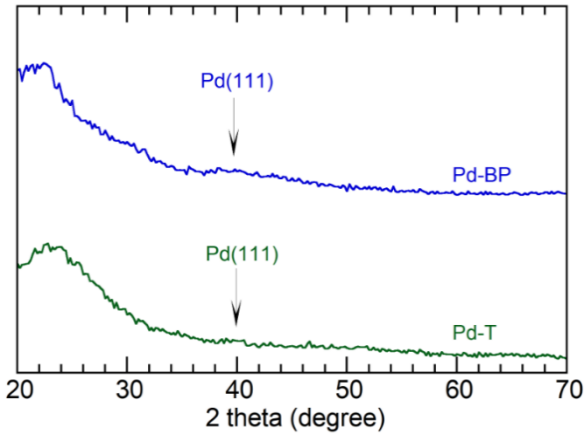

Fig. A4.2. Wide angle XRD pattern of Pd-T and Pd-BP. For these two Pd catalysts, wide-angle XRD data showed negligible intensity for Pd(111) surface, representing that the Pd nanoparticle size is approximately 3 nm.

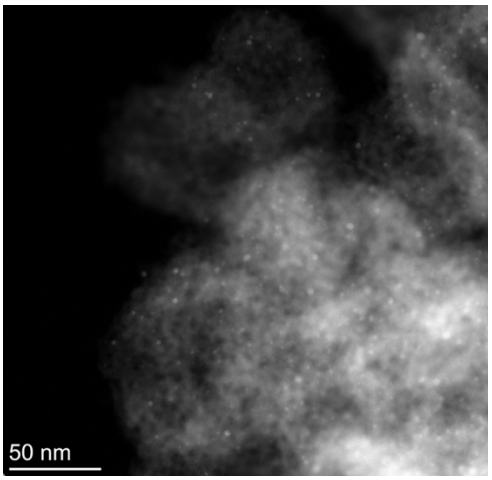

Fig. A4.3. TEM image of Pd-BP catalyst.

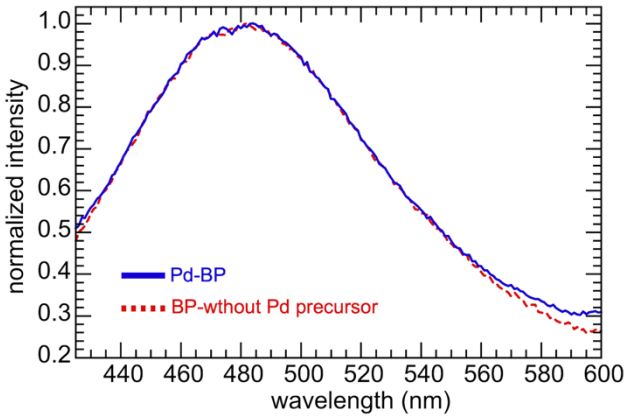

Fig. A4.4. Dotted red line shows fluorescent emission of Prodan adsorbed on BP support that underwent Pd catalyst synthesis steps (calcination at 300 °C for 2 h and reduction at 200 °C under H_2 flow for 2 h) except for the incipient impregnation step. This fluorescent spectrum is similar to that of Prodan-adsorbed Pd-BP.

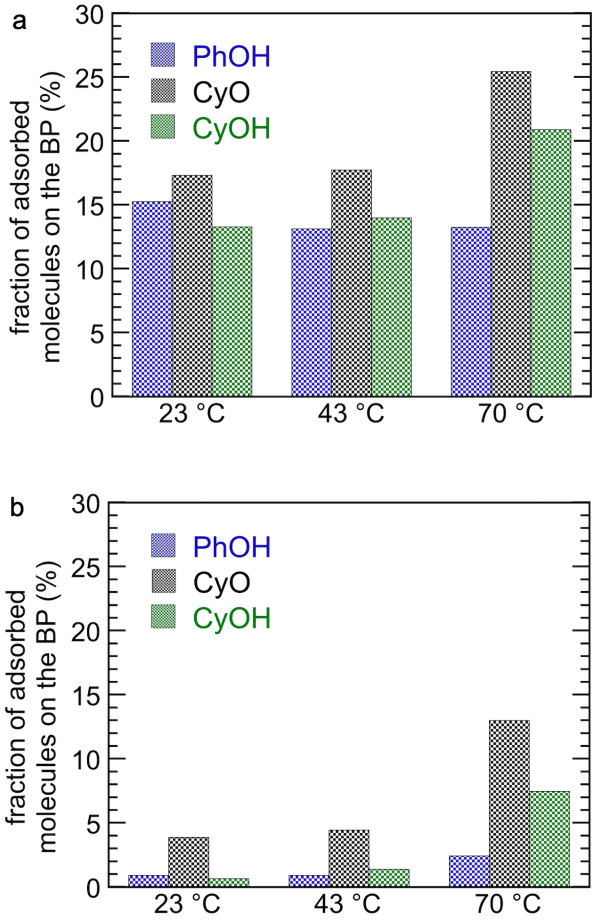

Fig. A4.5. The fraction of adsorbed phenol from the mixture of phenol/cyclohexanone/cyclohexanol aqueous solution onto the (a) BP and (b) T supports (70 mM each, 28.5 mg support materials was combined with 0.9 mL solution).

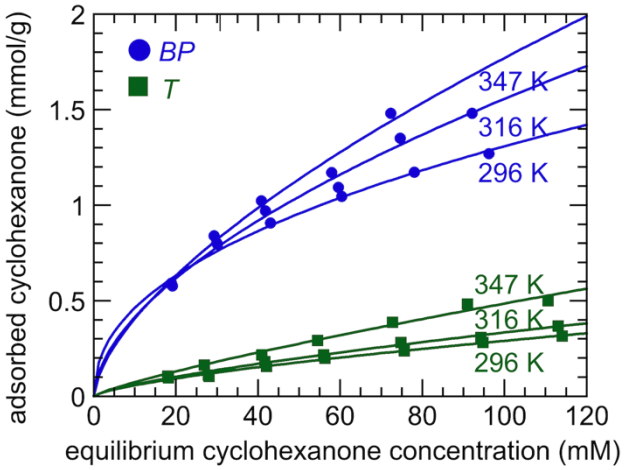

Fig. A4.6. Equilibrium adsorption of cyclohexanone frow water, onto BP and T supports at 296, 316, and 347 K. The isotherms represent non-linear curvefits using Freundlich model.

Table A4.3. Peak line widths (FWHM) for solution-phase and adsorbed phenol in the presence of Pd-BP and Pd-T, obtained by deconvolution of NMR spectra

Time	Pd-BP		Pd-T	
(h)	Adsorbed (Hz)	Solution (Hz)	Adsorbed (Hz)	Solution (Hz)
2.51	100.5	58.6	75.9	56.6
2.71	94.2	58.1	77.9	60.1
2.85	97.2	61.9	71.6	60.5
3.05	99.2	57.1	77.7	58.3
3.25	-	-	76.1	62.4
3.38	-	-	72.0	61.2
3.64	-	-	74.2	58.2

Table A4.4. Peak line widths (FWHM) for solution-phase and adsorbed cyclohexanone in the presence of Pd-BP and Pd-T, obtained by deconvolution of NMR spectra

Time (h)	Pd-BP		Pd-T	
	Adsorbed (Hz)	Solution (Hz)	Adsorbed (Hz)	Solution (Hz)
0.97	168.4	58.6	-	-
1.51	172.2	56.7	-	-
1.97	173.0	57.4	-	-
2.51	187.5	55.1	77.8	59.4
2.98	175.8	55.5	69.8	63.1
3.51	185.6	56.4	72.1	61.6
4.05	172.2	60.7	70.8	60.3
4.52	-	-	76.1	61.5
4.99	-	-	74.2	59.8

Scheme A4.1

The proposed microkinetic model considers reversible competitive adsorption of phenol (PhOH), cyclohexanone (CyO), and cyclohexanol (CyOH) from solution to Pd sites (*) and catalyst support sites (S*) (eq A4.1-6).

$$PhOH + * \rightleftarrows PhOH^* \quad \text{(A4.1)}$$

$$CyO + * \rightleftarrows CyO^* \quad \text{(A4.2)}$$

$$CyOH + * \rightleftarrows CyOH^* \quad \text{(A4.3)}$$

$$PhOH + S^* \rightleftarrows PhOH - S^* \quad \text{(A4.4)}$$

$$CyO + S^* \rightleftarrows CyO - S^* \quad \text{(A4.5)}$$

$$CyOH + S^* \rightleftarrows CyOH - S^* \quad \text{(A4.6)}$$

The model also considers facile migration between the support and Pd sites (eq A4.7-9).

$$PhOH - S^* + * \rightleftarrows PhOH^* + S^* \quad \text{(A4.7)}$$

$$CyO - S^* + * \rightleftarrows CyO^* + S^* \quad \text{(A4.8)}$$

$$CyOH - S^* + * \rightleftarrows CyOH^* + S^* \quad \text{(A.9)}$$

The dissociative adsorption of H_2 onto Pd (eq A4.10) is required to hydrogenate phenol (PhOH) and cyclohexanone (CyO) (eq. A4.11-12), however the rate dependence on H_2 is not considered here because H_2 pressure was in large excess during experiment and is assumed to be constant.

$$H_2 + 2 * \rightleftarrows 2H^* \quad \text{(A4.10)}$$

$$PhOH^* + 4H^* \rightarrow CyO^* \quad \text{(A4.11)}$$

$$CyO^* + 2H^* \rightarrow CyOH^* \quad \text{(A4.12)}$$

Adsorption experiments demonstrate that phenol and cyclohexanone adsorb onto Pd-BP and Pd-T within seconds at room temperature. However, the hydrogenation of phenol and cyclohexanone took several hours to reach completion at 60 °C. Therefore, we assume the reversible adsorption-desorption of each dissolved species to the Pd and support sites (eq A4.1-6,10) are quasi-equilibrated, whereas the hydrogenation steps (eq A4.11-12) are rate determining. Furthermore, the reaction proceeds much faster on Pd-BP than Pd-T, and phenol and cyclohexanone adsorb to the support in larger amounts for Pd-BP than Pd-T. This correlation suggests the possibility that phenol or cyclohexanone adsorbed on the support may transfer to Pd (eq A4.7-9). The facile migration between support and Pd sites is also expected to proceed much faster than the hydrogenation steps and can therefore be assumed as quasi-equilibrated.

These assumptions allow us to describe each reversible adsorption-desorption step with an algebraic equation and equilibrium constant. For species i (i = PhOH, CyO, CyOH), the adsorption to Pd from the solution is described by eq A4.13. Here, $N_{i,solution}$ is the moles of species i in solution, θ_i is the surface fraction of species i on the Pd sites, and θ_* is the surface fraction of open Pd sites.

$$K_{i1} = \frac{\theta_i}{N_{i,solution}\theta_*} \tag{A4.13}$$

Equilibrated adsorption-desorption of each species between the support and Pd is described by eq A4.14, where $N_{support}$ is the moles of open support sites and $N_{i,support}$ is the moles of species i adsorbed on the support.

$$K_{i2} = \frac{\theta_i N_{support}}{N_{i,support}\theta_*} \tag{A4.14}$$

The equilibrated adsorption-desorption between the species in solution and on the support is described by eq A4.15.

$$K_{i3} = \frac{N_{i,support}}{N_{support} N_{i,solution}} \quad \text{(A4.15)}$$

The total number of support adsorption sites on Pd-BP and Pd-T is unknown and difficult to measure. For simplicity, we assume the moles of open support sites ($N_{support}$) is much larger than the moles of each species adsorbed on the support ($N_{i,support}$). This assumption is likely a source of error, however it provides a convenient simplification of eqs A4.14-15.

$$K'_{i2} = \frac{K_{i2}}{N_{support}} = \frac{\theta_i}{N_{i,support}\theta_*} \quad \text{(A4.16)}$$

$$K'_{i3} = K_{i3} N_{support} = \frac{N_{i,support}}{N_{i,solution}} \quad \text{(A4.17)}$$

The deconvoluted operando NMR data provides direct measurements of $N_{i,support}$ and $N_{i,solution}$. Therefore, K'_{i3} is directly known (Fig A4.7) and can be specified at each timestep in the model. On Pd-T, K'_{i3} is small, and an average value is specified in the model (Table A4.5). On Pd-BP, the signal to noise ratio of $K'_{PhOH,3}$ and $K'_{CyOH,3}$ is small, and no clear trend is observed. Therefore, an average value of K'_{i3} is specified for both phenol and cyclohexanol (Table A4.5). In contrast, $K'_{CyO,3}$ shows a linear decrease in time until it reaches a constant value. Upon further inspection, the decrease in $K'_{CyO,3}$ correlates with the decrease in phenol in the system (Fig. A4.8). Upon complete phenol conversion, $K'_{CyO,3}$ remains constant. A linear regression of $K'_{CyO,3}$ vs. the fraction of phenol in the system gives the following equation, where N_i is the total moles (sum of species i in solution and ads. on the support) of species i.

$$K'_{CyO,3} = 0.62 \frac{N_{PhOH}}{N_{PhOH} + N_{CyO} + N_{CyOH}} + 0.4 \quad \text{(A4.18)}$$

Eq A4.18 is included in the model and calculates $K'_{CyO,3}$ at each timestep. We hypothesize that $K'_{CyO,3}$ is a linear combination of two adsorption constants: 1) cyclohexanone adsorption to Pd-BP and 2) synergistic adsorption of a cyclohexanone-phenol hydrogen bonded complex.

A more informative chemical description of this hypothesized reaction is under further investigation in future models.

Solving eq A4.13, 16, 17 for the fraction of species in on Pd (θ_i) results in the following system of equations:

$$\theta_i = K_{i1} N_{i,solution} \theta_* \tag{A4.19}$$

$$\theta_i = K'_{i2} K'_{i3} N_{i,solution} \theta_* \tag{A4.20}$$

Clearly, $K_{i,1}$ must equal $K'_{i2}K'_{i3}$ for eqs A4.19-20 to be simultaneously true. This requirement is a direct consequence of assuming the adsorption-desorption of species between the solution, support, and Pd phases are all quasi-equilibrated. To minimize the error associated with deconvoluting the operando NMR data into separate adsorbed and solution populations, it is convenient to write the surface fractions on Pd (θ_i) in terms of the total moles of each species in the system ($N_{i,total}$). Therefore, θ_i is defined as follows:

$$\theta_i = \frac{K_{i1}}{1+K'_{i3}} N_{i,total} \theta_* \tag{A4.21}$$

If we assume a constant total number of Pd sites, a site balance can be solved for the open Pd active sites (eq A4.22).

$$\theta_* = \frac{1}{1+\sum_i \frac{K_{i1}}{1+K'_{i3}} N_{i,total}} \tag{A4.22}$$

After its formation, cyclohexanol does not further react, and it does not appear to strongly adsorb to Pd (which would greatly slow down the cyclohexanone hydrogenation rate as the cyclohexanone conversion increases). Consequently, we assume $K_{CyOH,1}$ is small and eq A4.22 simplifies to eq A4.23. This assumption is further supported by unsuccessful attempts to improve the fit by including $K_{CyOH,1}$.

$$\theta_* = \frac{1}{1+\frac{K_{PhOH,1}}{1+K'_{PhOH,3}}N_{PhOH,total}+\frac{K_{CyO,1}}{1+K'_{CyO,3}}N_{CyO,total}} \tag{A4.23}$$

As previously mentioned, the surface hydrogenation of phenol and cyclohexanone are assumed to be rate-determining steps. Thus, the overall rates of each species are described by eq A4.24-26. Here, n_{Pd} is the total moles of Pd surface sites.

$$\frac{dN_{PhOH,total}}{dt} = -n_{Pd}k_{PhOH}\theta_{PhOH} = -n_{Pd}k_{PhOH}\frac{K_{PhOH,1}}{1+K'_{PhOH,3}}N_{PhOH,total}\theta_*$$

$$= \frac{-n_{Pd}k_{PhOH}\frac{K_{PhOH,1}}{1+K'_{PhOH,3}}N_{PhOH,total}}{1+\frac{K_{PhOH,1}}{1+K'_{PhOH,3}}N_{PhOH,total}+\frac{K_{CyO,1}}{1+K'_{CyO,3}}N_{CyO,total}} \tag{A4.24}$$

$$\frac{dN_{CyO,total}}{dt} = n_{Pd}k_{PhOH}\theta_{PhOH} - n_{Pd}k_{CyO}\theta_{CyO}$$

$$= n_{Pd}k_{PhOH}K_{PhOH}N_{PhOH,total}\theta_* - n_{Pd}k_{CyO}\frac{K_{CyO,1}}{1+K'_{CyO,3}}N_{CyO,total}\theta_*$$

$$= \frac{n_{Pd}(k_{PhOH}\frac{K_{PhOH,1}}{1+K'_{PhOH,3}}N_{PhOH,total}-k_{CyO}\frac{K_{CyO,1}}{1+K'_{CyO,3}}N_{CyO,total})}{1+\frac{K_{PhOH,1}}{1+K'_{PhOH,3}}N_{PhOH,total}+\frac{K_{CyO,1}}{1+K'_{CyO,3}}N_{CyO,total}} \tag{A4.25}$$

$$\frac{dN_{CyOH,T}}{dt} = n_{Pd}k_{CyO}\theta_{CyO} = n_{Pd}k_{CyO}\frac{K_{CyO,1}}{1+K'_{CyO,3}}N_{CyO,T}\theta_*$$

$$= \frac{n_{Pd}k_{CyO}\frac{K_{CyO,1}}{1+K'_{CyO,3}}N_{CyO,total}}{1+\frac{K_{PhOH,1}}{1+K'_{PhOH,3}}N_{PhOH,total}+\frac{K_{CyO,1}}{1+K'_{CyO,3}}N_{CyO,total}} \tag{A4.26}$$

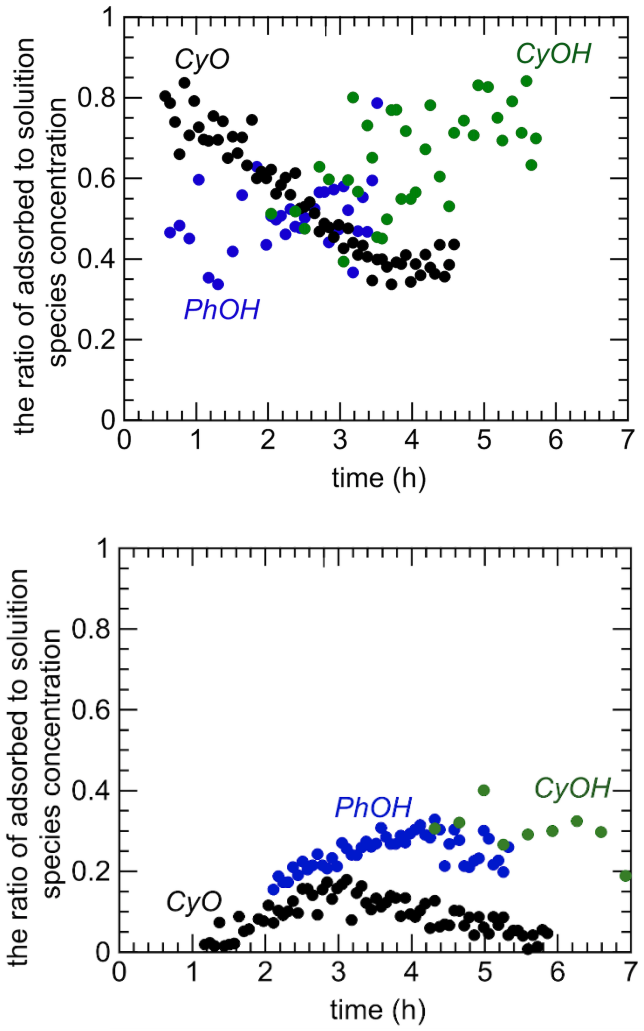

Fig. A4.7. (a) The ratio of adsorbed- to solution-phases species during the reaction over the Pd-BP catalyst. (b) The ratio of adsorbed- to solution-phases species during the reaction over the Pd-T catalyst.

Table A4.5. Ratios of adsorbed vs. solution phase species from Fig. A4.7. Values in parenthesis represent standard deviations.

Parameter	Pd-BP	Pd-T
$K_{PhOH\_support}$	0.50 (0.08)	0.25 (0.04)
$K_{CyO\_support}$	$0.62 \times PhOH_{frac} + 0.4$	0.09 (0.05)
$K_{CyOH\_support}$	0.65 (0.12)	0.29 (0.05)

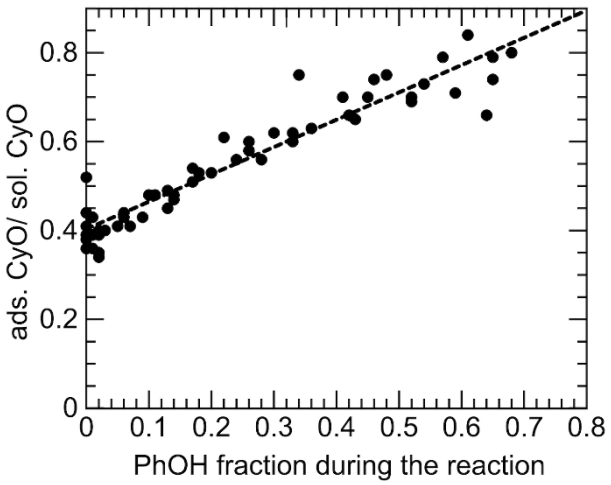

Fig. A4.8. The ratio of adsorbed- to solution-phase cyclohexanone as a function of the fraction of phenol during the reaction.

Chapter 5. Synergy between solvent and surface polarity effects on Pd-catalyzed phenol hydrogenation

5.1 Abstract

The extent of reactant/intermediate adsorption is a critical factor that influences the activity/selectivity in heterogeneous catalysis. In this study, the combined effects of solvent and surface polarity on phenol adsorption were investigated in phenol hydrogenation catalyzed by silica-supported Pd nanoparticles. Correlation of adsorption with solvatochromic parameters indicates that, regardless of surface type (hydrophobic or hydrophilic), solvents with polarities very different from that of phenol (e.g., water, cyclohexane) adsorb much more phenol at room temperature, whereas solvents with polarities similar to phenol result in negligible adsorption, presumably due to differences in the degree of phenol solvation. Kinetic profiles for phenol hydrogenation indicate that promoting phenol adsorption is correlated with a higher phenol hydrogenation rate. For the same solvent, a more hydrophobic organosilica-based catalyst shows higher affinity for phenol than a more hydrophilic inorganic silica-based catalyst, and consequently both increased activity and selectivity to cyclohexanone. Although, the effect of surface polarity effect on hydrogenation activity is less significant than the solvent effect, the more hydrophobic catalyst can increase the phenol hydrogenation activity by a factor of 1.6 – 2 and the cyclohexanone selectivity by 10 – 20 % in water and cyclohexane.

5.2 Introduction

Catalysts that are active and selective toward biomass conversion are highly sought after. Reoptimizing catalysts that were originally designed for gas phase hydrocarbon conversion for liquid phase operation with organic oxygenates is a major undertaking. One strategy to enhance activity/selectivity in liquid-phase heterogeneous catalytic reactions is to modulate surface interactions by the choice of solvent.[1–4] For example, the rate of acetophenone hydrogenation catalyzed by Ni/SiO_2 is lower in polar aprotic solvents (THF, acetonitrile, γ-butyrolactone) than in non-polar solvents (cyclohexane, toluene, benzene). The difference was attributed to stronger acetophenone interactions with the polar aprotic solvents, which reduce acetophenone adsorption on the catalyst surface.[2] In the same reaction catalyzed by Rh/Al_2O_3, decreasing hydrogen-bond acceptor (HBA) ability of the solvent is correlated with increasing hydrogenation rates, since hydroxyl groups on the Al_2O_3 support interact with the solvent, and further limit acetophenone adsorption.[1]

A second approach to further enhance catalytic activity/selectivity is to modulate the polarity of the catalyst in order to control the extent of reactant adsorption and/or product desorption.[5–7] For example, a hydrophobic zeolite with a lower Al content shows increased activity in sorbitol dehydration and selectivity to isosorbide compared with a zeolite with a higher Al content because water molecules formed during the dehydration are rapidly rejected.[6,7] Thus, the choice of appropriate solvent type as well as surface polarity to maximize reactant adsorption and/or product desorption can contribute to optimizing activity and selectivity in liquid phase heterogeneous catalysis.

The present study was undertaken to identify the independent roles of solvent and surface polarity for a model reaction over hydrophilic/hydrophobic Pd catalysts, as well as any synergies between them. Phenol hydrogenation in the liquid phase was conducted under

mild conditions (< 373 K), but selective hydrogenation to cyclohexanone with high phenol conversion is challenging. An alternative process to produce cyclohexanone/cyclohexanol is cyclohexane oxidation, but it requires harsher reaction conditions (425 K, 2 MPa).[8] Many liquid-phase phenol hydrogenation studies have been conducted in water. For example, the conversion of phenol to cyclohexanone catalyzed by Pd nanoparticles supported on mesoporous carbon nitride exceeded 99%, while ethanol and THF solvents gave 95% and 30% conversion, respectively.[9] However, solvent effect studies in phenol hydrogenation catalyzed by Pd remain rare;[10,11] most focus instead on the effect of the catalyst support and additives such as alkali metals, on the cyclohexanone selectivity.

In order to bridge this knowledge gap, phenol adsorption onto two different Pd catalysts (supported on hydrophobic and hydrophilic silica supports) was quantified in seven different solvents, ranging from very polar to very non-polar. The hydrogenation activities and cyclohexanone selectivities of the Pd catalysts were assessed by *operando* magic angle spinning nuclear magnetic resonance (NMR) and correlated with the extent of phenol interaction with the catalyst support.

5.3 Materials and methods

5.3.1 Chemicals

All commercial materials were used as received. Tetraethylorthosilicate (T, 98%), 4,4′-bis(triethoxysilyl)-1,1′-biphenyl (BP, 95%), Pluronic P123, phenol (99%), cyclohexane (≥99%), methanol (99.8%), tetrahydrofuran (≥99%), *p*-dioxane (≥99%), palladium(II) acetate, n-decane (≥99%), and acetonitrile (≥99.9%) were purchased from Sigma Aldrich. Phenol (1-

^{13}C, 99%) was obtained from Cambridge Isotope Laboratories, Inc. H_2 (5 % in N_2) was purchased from Airgas, Inc.

5.3.2 Catalyst preparation and characterization

The Pd-BP and Pd-T catalysts were prepared as indicated in section 4.3.2, and characterized as indicated in section 4.3.3. Pd loading for two catalysts were 0.95 and 0.94 w%. Both catalysts showed similar Pd dispersion, ca. 52 % assuming a chemisorption stoichiometry Pd:CO = 2. B.E.T. surface areas were 607 m^2/g for the hydrophobic Pd-BP, and 785 m^2/g for the hydrophilic Pd-T. The λ_{max} of Prodan fluorescence were 483 nm for Pd-BP and 523 nm for Pd-T, confirming that the organosilica surface is much less polar than the silica surface.

5.3.3 Adsorption tests

The amounts of adsorbed phenol were measured by mixing Pd-BP (20 mg) with a phenol solution (1.5 mL, 50 mM) in H_2O, methanol, acetonitrile, tetrahydrofuran, *p*-dioxane, *n*-decane, and cyclohexane). The slurry was agitated in a IKA Vortex 4 digital mixer at 3000 rpm for 10 min, then centrifuged at 3000 rpm for 5 min to separate the solid. The decanted supernatant was analyzed by solution-state ^1H NMR (Varian Unity, 500 MHz). A shim map was created for each solvent, using solvent peaks as the standard, without the need for another internal standard to calculate adsorption amounts.

5.3.4 *Operando* MAS NMR experiments

Magic-angle-spinning (MAS) NMR experiments were performed as indicated in section 4.3.4. All the reactions were conducted at 90 °C.

5.4 Results and discussion

5.4.1 Solvent dependence of phenol adsorption on mesoporous silicas

Stronger interaction between a reactant and catalyst leads to an increase in surface concentration of the reactant, which can result in more efficient catalytic conversion. When the reaction involves a liquid phase, the property of the solvent is also important, since solvent–reactant and solvent–surface interactions are also affected by reactant adsorption. We assessed phenol–catalyst interactions in a variety of solvents by measuring the amount of phenol adsorbed onto the surface of a mesoporous silica catalyst. A phenol solution (1.5 mL, 50 mM) was mixed with the catalyst (20 mg) at room temperature, and the phenol concentration remaining in the solution phase was measured. The amount of adsorbed phenol was obtained by difference.

Table. 5.1 shows the results for various solvents and two catalysts: more hydrophobic Pd-BP (organosilica, with biphenylene linkers in the framework), and more hydrophilic Pd-T. From an aqueous solution, ca. 0.9 phenol molecules/nm^2 was adsorbed onto Pd-BP. In contrast, phenol solutions in non-polar *n*-decane or cyclohexane resulted in much more (2-3×) adsorbed phenol (ca. 2.5 and 2.1 phenol molecules/nm^2, respectively). Interestingly, solvents of intermediate polarity (methanol, THF, and acetonitrile) led to much smaller amounts of adsorbed phenol (0.03-0.1 molecules/nm^2).

Phenol adsorption from water onto more polar Pd-T is much smaller: ca. 0.1 molecules/nm^2, Table. 5.1. Solvents with intermediate polarity also resulted in very little

adsorption. In contrast, adsorption from either of the non-polar solvents (n-decane or cyclohexane) resulted in similar adsorbed amounts on either Pd-T or Pd-BP (ca. 2 phenol molecules/nm^2). Considering only these adsorbed amounts, reactions of phenol are expected to be fastest in non-polar solvents, slower in water, and slowest of all in intermediate polarity solvents. Reactivity for the two catalysts may be similar for each solvent except water, where adsorption is much higher on Pd-BP.

Table 5.1. Phenol amounts adsorbed from a 50 mM solution in various solvents (1.5 mL) onto either Pd-BP or Pd-T (20 mg), at room temperature. The adsorbed amounts are normalized by the surface areas of the catalysts as shown in Table A4.1.

Materials	Phenol adsorbed (molecules/nm^2)						
	water	methanol	acetonitrile	THF	*p*-dioxane	n-decane	cyclohexane
Pd-BP	0.88	0.11	0.04	0.04	0.16	2.49	2.11
Pd-T	0.08	-	0.03	0.06	0.14	2.16	2.00

To interpret these results in terms of solvation, the solvatochromic parameters[12] for each solvent were considered (Table 5.1). Phenol is expected to be more readily solvated by solvents with relative polarities similar to that of phenol (0.701). In addition, solvents which are hydrogen-bond acceptors (HBAs) are expected to interact with phenol via hydrogen bonding with the phenolic hydroxyl group.[13] Although water is a good HBA, its high polarizability index (π^*) and relative polarity limit phenol-water interactions. Thus, limited interaction between phenol and water results in appreciable phenol adsorption onto the Pd-BP surface. Less phenol is adsorbed onto hydrophilic Pd-T from water due to the polar nature of

the surface, which results in weaker phenol-surface interactions and stronger water-surface interactions.

Table 5.2. Solvatochromic parameters[12] for various solvents and phenol

Solvent	H-bond acceptor ability (β)	Polarizability index (π*) [a]	Relative polarity [b]
water	0.47	1.09	1.000
methanol	0.66	0.60	0.762
phenol	N/A	N/A	0.701
acetonitrile	0.40	0.66	0.460
tetrahydrofuran	0.55	0.55	0.207
p-dioxane	0.37	0.49	0.164
n-hexane	0.00	-0.11	0.009
cyclohexane	0.00	0.00	0.006

[a] π* scale is derived from solvent effects on the π → π* electronic transitions of a selection of seven positively solvatochromic nitroaromatics.[12] [b] Relative polarity is obtained by measuring the shift in the absorption spectrum of Reichardt's dye.[12]

Methanol is the strongest HBA in the group, and has a lower π* value than water. The relative polarity of methanol, 0.762, is very similar to that of phenol. Thus, strong phenol solvation in methanol results in negligible phenol adsorption regardless of surface polarity. Acetonitrile and THF are moderate HBAs and have intermediate polarities. These solvents

are also effective at solvating phenol, resulting in negligible adsorption on either catalyst. Less polar *p*-dioxane solvates phenol less, and gave slightly more phenol adsorption than from acetonitrile or THF.

Extrapolating the solvatochromic parameters of *n*-hexane to *n*-decane, and noting the similar parameters of cyclohexane, the solvation of phenol by all of these non-polar solvents is very limited. Since these solvents also interact weakly with the silica surfaces, it is not surprising that their use results in the highest adsorption of phenol.

5.4.2 Kinetics of phenol hydrogenation in cyclohexane

Phenol hydrogenation catalyzed by Pd-BP was studied in cyclohexane at 90 °C using *operando* NMR to observe changes in chemical species. A typical array is shown in Fig. 5.1. Peaks at ca. 155, 202-210, and 68 ppm correspond to phenol-1-^{13}C and its hydrogenated analogs cyclohexanone and cyclohexanol, respectively. The concentration of cyclohexanone increases rapidly as phenol disappears in the early stages of the experiment. After the phenol is consumed, cyclohexanol appears due to cyclohexanone hydrogenation. The peak at 25 ppm due to cyclohexane does not change in intensity during the reaction.

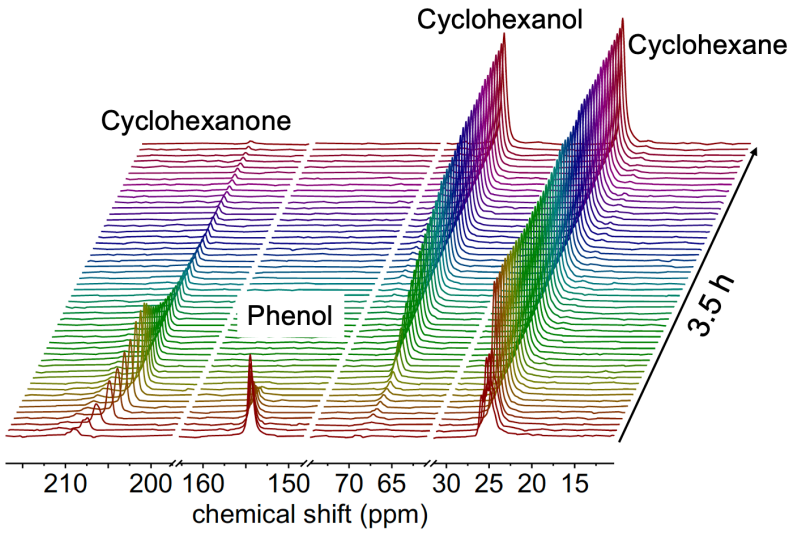

Fig. 5.1. Time-resolved *operando* NMR spectra, showing phenol hydrogenation catalyzed by Pd-BP in cyclohexane (catalyst 3.8 mg, solvent 0.12 mL, phenol-1-^{13}C 6 mg, H_2 50 bar (pressure at 23 °C), 90 °C).

Fig. 5.2 shows magnified peaks for the three species involved in the reaction. As the phenol concentration decreases, its chemical shift increases from ca. 154.5 to 155.7 ppm. This change is caused by hydrogen-bonding between phenol and cyclohexanone, which results in deshielding of the phenol-1-^{13}C signal.[13,14] The cyclohexanone chemical shift decreases dramatically as the phenol concentration decreases. The ^{13}C chemical shift of the carbonyl carbon is strongly correlated with the polarity of its environment: an upfield shift represents a less polar environment.[15–17] Thus, the upfield shift of the cyclohexanone-1-^{13}C signal as phenol is consumed arises from the loss of its hydrogen-bonding interaction with phenol. The chemical shift increased slightly during cyclohexanone hydrogenation, due to the augmented cyclohexanone-cyclohexanol association. The signal for cyclohexanol did not change appreciably during the reaction.

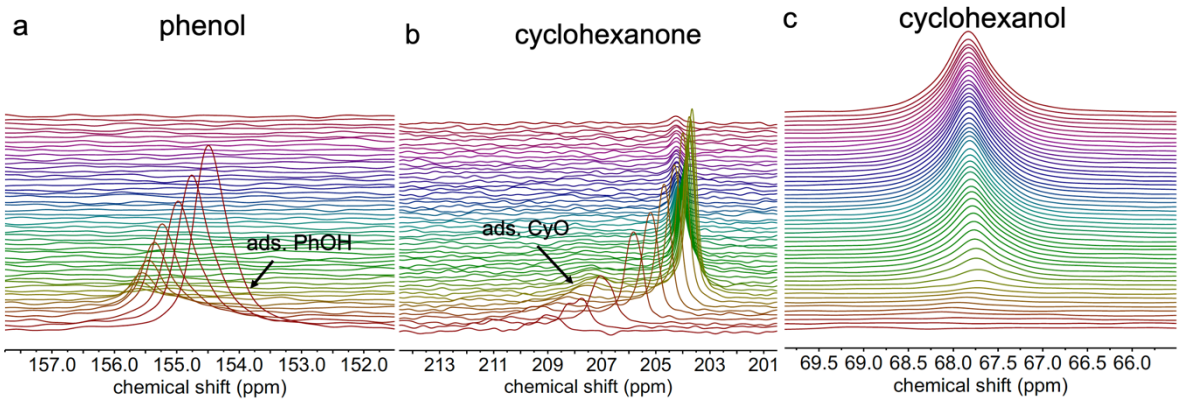

Fig. 5.2. *Operando* NMR spectra showing magnified regions for: (a) phenol-1-^{13}C, (b) cyclohexanone-1-^{13}C, and (c) cyclohexanol-1-^{13}C.

The NMR peak shape of phenol was unsymmetrical, and deconvolution shows that an additional peak with a larger peak width (FWHM) is at a slightly lower chemical shift (Fig. A5.1). Deconvolution reveals that the peak width (FWHM) of the shoulder is 64 % larger than that of the peak representing phenol in solution (Table A5.1). A larger peak width indicates reduced mobility, and is associated with adsorption. The chemical shifts of both solution and adsorbed phenol shift downfield due to increasing extent of phenol-cyclohexanone hydrogen bonding interaction.[13,14] For cyclohexanone, the adsorbed material gives rise to a resolved peak downfield of the solution-phase peak (Fig. 5.2b), indicating that the surroundings of the adsorbed cyclohexanone are more polar than the solution-phase consisting of hydrophobic cyclohexane solvent molecules. During the reaction, the chemical shifts of both solution and adsorbed cyclohexanone shift upfield, since increasing cyclohexanone concentration in the solution and adsorbed phase makes the surroundings of cyclohexanone less polar. Due to the low signal-to-noise ratio, the peak width of the adsorbed cyclohexanone signal was not quantified. No clear signal was observed for adsorbed cyclohexanol (Fig. 5.2c), presumably because its chemical shift is very similar to that of solution-phase cyclohexanol.

Kinetic profiles were obtained by integrating NMR peaks representing each species in both the solution-phase and adsorbed. Fig. 5.3a shows that 0.53 M phenol was fully converted in ca. 40 min. The reaction appears to be close to zeroth-order, suggesting that the active surface is fully covered by phenol. The cyclohexanone concentration reached a maximum concentration of ca. 0.48 M, corresponding to 90 mol% selectivity, at 40 min. At this time, the cyclohexanol concentration was ca. 40 mM. After phenol was converted, the cyclohexanone concentration abruptly decreased. The sharp change indicates that cyclohexanone adsorption onto the Pd active sites is effectively inhibited by phenol. The cyclohexanone concentration decreased in approximately first-order fashion over the next 3 h. This behavior suggests that the active surface is not saturated with cyclohexanone. Cyclohexanol is formed quantitatively as the final product.

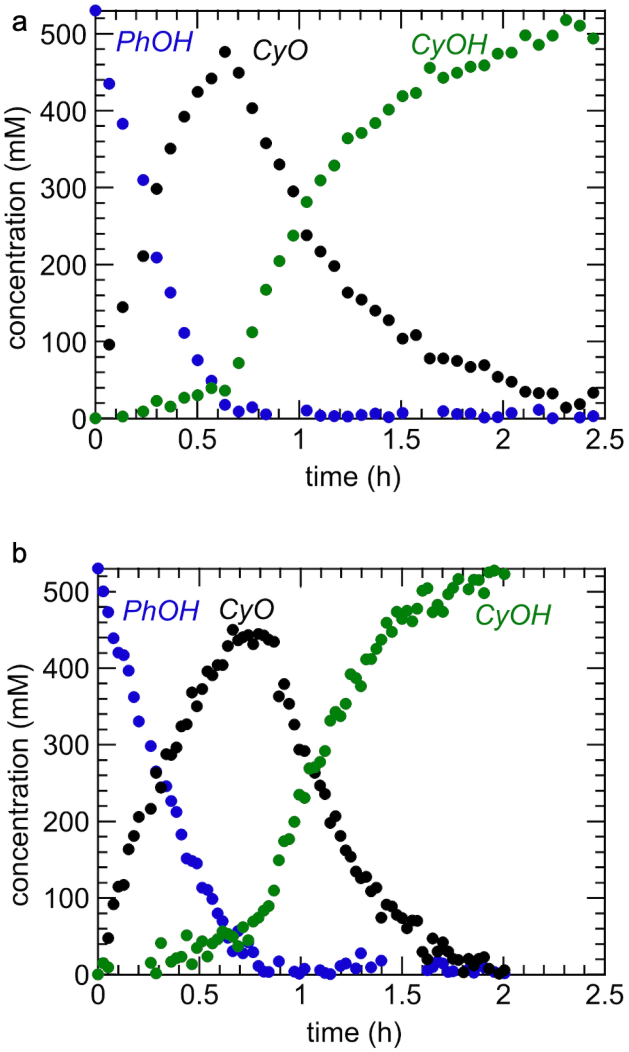

Fig. 5.3. Kinetic profiles recorded during phenol hydrogenation in (a) cyclohexane (b) water catalyzed by Pd-BP obtained by integrating *operando* NMR peaks representing solution-phase and adsorbed phases. Reaction conditions: 0.53 M phenol-1-^{13}C (in 0.12 mL solvent), 3.8 mg catalyst, 50 bar H_2 at 23 °C. Reaction temperature 90 °C.

5.4.3 Kinetics of phenol hydrogenation in water

The kinetics of phenol hydrogenation was also studied in water. Like cyclohexane, this solvent results in an appreciable amount of phenol being adsorbed onto Pd-BP (Table. 5.1). *Operando* NMR spectra were collected under the same reaction conditions. The phenol

concentration decreases quickly at the beginning of the reaction, yielding cyclohexanone (Fig. 5.4). When the phenol peak has almost disappeared, the peak for cyclohexanol grows due to cyclohexanone hydrogenation.

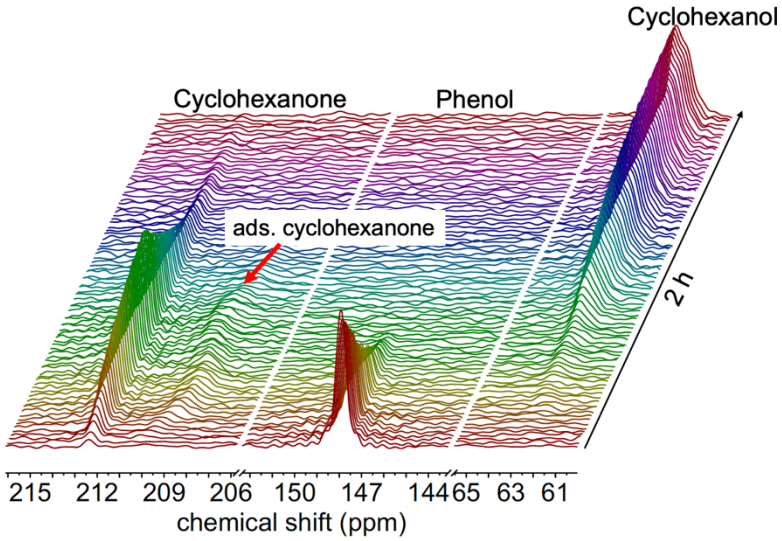

Fig. 5.4. Time-resolved *operando* NMR spectra, showing phenol hydrogenation catalyzed by Pd-BP in water (catalyst 3.8 mg, solvent 0.12 mL, phenol-1-^{13}C 6 mg, H_2 50 bar at 23 °C, 90 °C).

In contrast to the behavior in cyclohexane, the chemical shift of phenol in the solution-phase changes little under reaction conditions when water is the solvent. This may be because phenol solvated by water molecules does not form hydrogen bonds to cyclohexanone. The presence of adsorbed phenol was not clear possibly due to only small difference in chemical shifts between adsorbed and solution-phase phenol peaks. makes the peak, thus deconvolution was not successful. Resolved peaks are again visible for cyclohexanone in solution (ca. 212 ppm) and on the surface (ca. 209 ppm). However, the chemical shift of adsorbed cyclohexanone is lower than in the more polar water phase (compared to the higher chemical

shift of adsorbed molecules on the same surface, relative to the less polar cyclohexane phase). Thus the surface polarity of Pd-BP is intermediate between those of water and cyclohexane, as expected. The chemical shift of adsorbed cyclohexanone changes in a complex way over the course of the reaction, caused by varying extents of hydrogen-bonding and dipole-dipole interactions as the surface chemical composition changes.[15–17] This phenomenon was observed even more clearly when the same reaction was conducted at 60 °C (Chapter 4), since association by hydrogen-bonding is enhanced at the lower temperature.[18]

The kinetic profiles obtained by integrating the NMR regions representing both solution and adsorbed chemical species are shown in Fig. 5.3b. There is surprisingly little effect of solvent on the kinetics, despite the very different solvating properties of water and cyclohexane. The time required to convert all phenol is ca. 50 min, and the reaction is close to zeroth-order. Both are similar to the observations made in cyclohexane as solvent. The maximum cyclohexanone concentration, ca. 0.44 M, is slightly lower (ca. 8%) than that observed in cyclohexane (Fig. 5.3a). Conversion of cyclohexanone to cyclohexanol again accelerates abruptly when phenol is fully converted, and proceeds in an exponential decay.

5.4.4 Kinetics of phenol hydrogenation in intermediate-polarity solvents

Next, we studied the kinetics of phenol hydrogenation catalyzed by Pd-BP in the solvents which cause little adsorption of phenol, including methanol, acetonitrile, THF, and *p*-dioxane. Fig. A5.2 shows the *operando* NMR spectra recorded using methanol as solvent under the same reaction conditions. The rate of phenol hydrogenation decreased slowly over the course of 3 h, Fig. 5.5. The phenol peak is symmetrical, indicating negligible phenol adsorption consistent with the adsorption test (Table 5.1). Thus, a low local concentration of

phenol on the catalyst may be responsible for the much lower initial activity, compared to the reactions in cyclohexane or water.

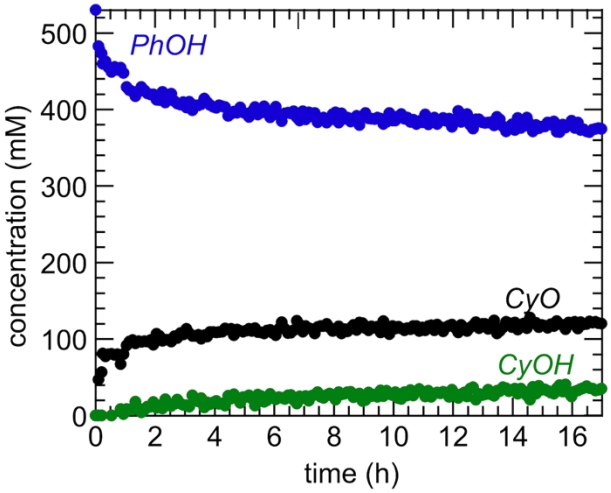

Fig. 5.5. Kinetic profiles for phenol hydrogenation catalyzed by Pd-BP in methanol, obtained by integrating the *operando* NMR peaks. Reaction conditions: 0.53 M phenol-1-^{13}C (in 0.12 mL methanol), 3.8 mg Pd-BP, 50 bar H_2 at 23 °C. Reaction temperature 90 °C.

Curiously, the reaction slowed to an almost imperceptible rate at ca. 30 % conversion, and little change was observed over the next 14 h. Thus the catalyst is deactivated. A previous study of phenol hydrogenation catalyzed by Pt reported that the catalyst is poisoned by strongly adsorbed CO formed by methanol reforming.[19] It is possible that a similar poisoning of Pd inhibits phenol adsorption.

In acetonitrile or THF, even less phenol was hydrogenated (4-5% after ca. 100 min) under the same reaction conditions (Fig. 5.6a,b). No signals for adsorbed phenol were observed by NMR (Figs. A5.3 and A5.4), consistent with the adsorption measurements (Table. 5.1). Thus, the high extent of phenol solvation results in the negligible phenol

conversion. In addition, competition between phenol and the coordinating solvent for the catalyst surface could be a cause of the very slow reactions. Furthermore, acetonitrile can poison the Pd active sites via its Pd-catalyzed conversion to strongly coordinating amines.[20]

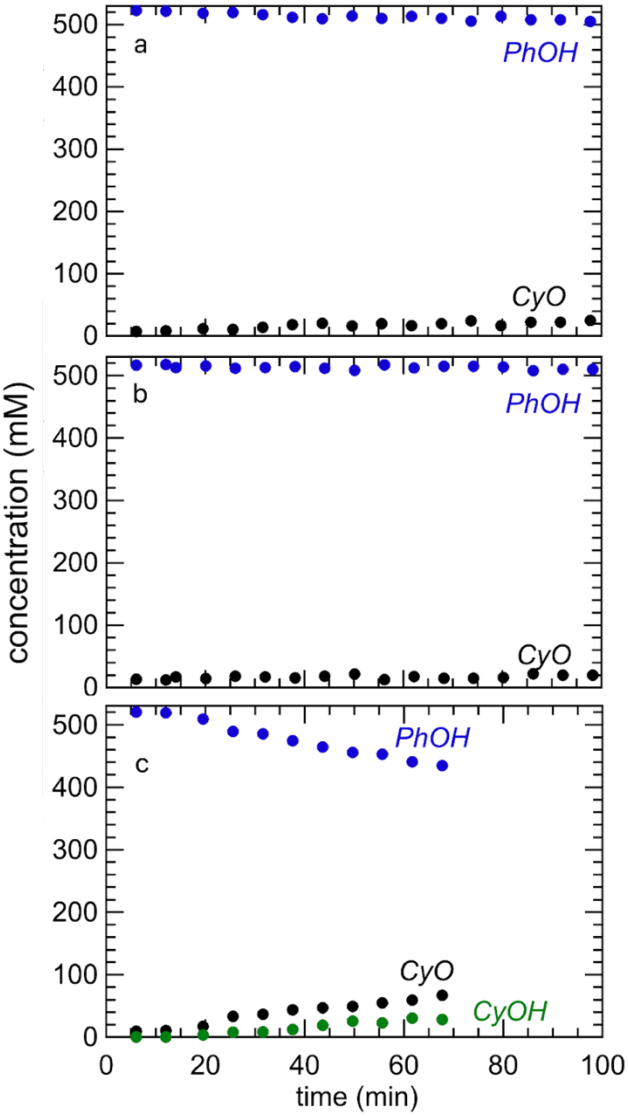

Fig. 5.6. Kinetic profiles for phenol hydrogenation catalyzed by Pd-BP, obtained by integrating the *operando* NMR peaks, in (a) acetonitrile, (b) THF, and (c) *p*-dioxane. Reaction conditions: 0.53 M phenol-1-^{13}C (in 0.12 mL solvent), 3.8 mg Pd-BP, 50 bar H_2 at 23 °C. Reaction temperature 90 °C.

The behavior of phenol in *p*-dioxane was also tested (Fig. A5.5). The kinetic profiles shows ca. 17 % phenol conversion after 1 h (Fig. 5.6c). This is an order of magnitude higher than the conversion obtained in THF and acetonitrile under similar conditions. The lower polarity of *p*-dioxane leads to slightly increased phenol adsorption, Table. 5.1 Curiously, the reaction also shows evidence for acceleration after an induction period, however, the low overall reactivity did not merit further investigation. The results show a correlation between phenol affinity for Pd-BP and the rate of phenol hydrogenation.

5.4.5 The effect of surface polarity on phenol and cyclohexanone hydrogenation rates

Phenol hydrogenation in cyclohexane was conducted using the hydrophilic Pd-T catalyst under the same reaction conditions, monitored by *operando* NMR (Fig. A5.6). As in the reaction catalyzed by hydrophobic Pd-BP, the main phenol peak shifts downfield by ca. 1.5 ppm, while the main cyclohexanone peak shifts upfield by ca. 5 ppm as the reaction proceeds (Fig. 5.7a,b). At the beginning of the reaction, the cyclohexanol peak shifts upfield by ca. 1 ppm, then downfield by ca. 0.3 ppm after phenol was fully converted (Fig. 5.7c).

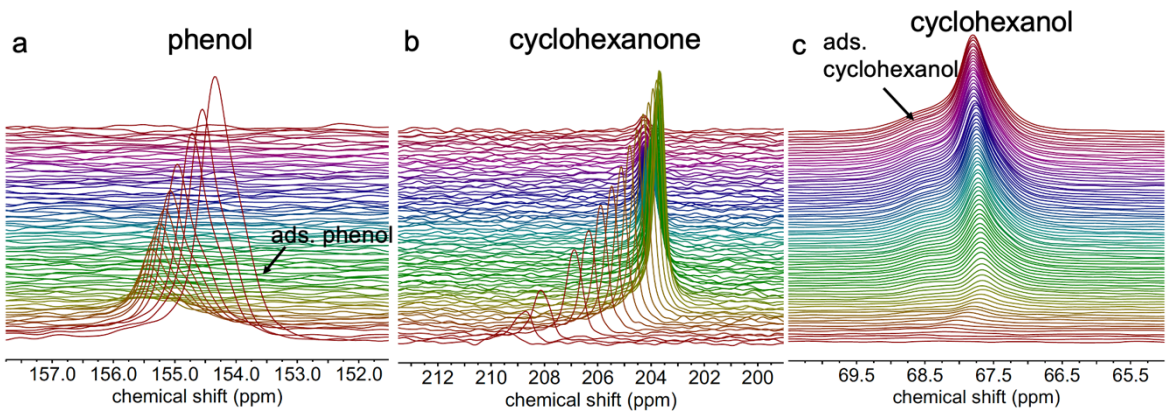

Fig. 5.7. *Operando* ^{13}C NMR spectra showing magnified regions for: (a) phenol-1-^{13}C, (b) cyclohexanone-1-^{13}C, and (c) cyclohexanol-1-^{13}C. Reaction conditions: Pd-T 3.8 mg, cyclohexane 0.12 mL, phenol-1-^{13}C 6 mg, H_2 50 bar, 90 °C.

The NMR peak shape of phenol was unsymmetrical, and deconvolution shows an additional peak with a larger peak width (Fig. A5.7). The peak width (FWHM) for adsorbed phenol, ca. 71 Hz (Table A5.1), is ca. 12% higher than solution phase peak, indicating slightly reduced mobility for adsorbed phenol. Its peak also shifts downfield as the reaction proceeds (Fig. 5.7a), indicating that the ratio of adsorbed phenol to adsorbed cyclohexanone decreases. The intensity of adsorbed cyclohexanone peak was too low, but magnified peak region showed that the adsorbed cyclohexanone peak appears at a higher chemical shift compared to the peak position of solution-phase cyclohexanone (Fig. A5.8). These observations are quite similar to those reported above for the Pd-BP catalyst. However, there is a major difference in the appearance of the cyclohexanol region. A clear peak for adsorbed cyclohexanol appears at higher chemical shift than the solution-phase peak, and the peak intensity gradually increased as the reaction proceeds due to the cyclohexanone-cyclohexanol interaction (Fig. 5.7c).

Kinetic profiles for phenol hydrogenation catalyzed by Pd-T in cyclohexane are shown in Fig. 5.8a. All phenol is converted after ca. 1 h, suggesting a slightly lower activity than Pd-

BP. The maximum cyclohexanone concentration for Pd-T is ca. 0.44 M (80 mol% selectivity) with 0.07 M cyclohexanol (20 mol% selectivity). This is ca. 10 mol% lower than found for Pd-BP. Subsequent hydrogenation of cyclohexanone is much slower over Pd-T.

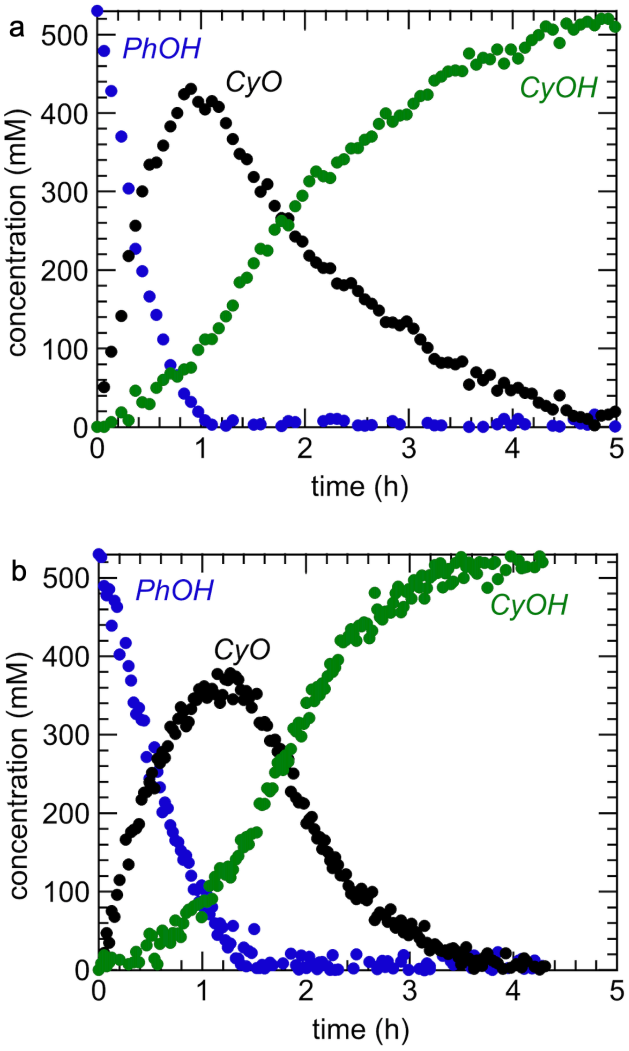

Fig. 5.8. Kinetic profiles recorded during phenol hydrogenation in (a) cyclohexane (b) water catalyzed by Pd-T obtained by integrating *operando* NMR peaks representing solution-phase and adsorbed phases. Reaction conditions: 0.53 M phenol-1-^{13}C (in 0.12 mL solvent), 3.8 mg catalyst, 50 bar H_2 at 23 °C. Reaction temperature 90 °C.

Adsorbed phenol is much less mobile on the Pd-BP surface than on Pd-T (FWHM 103 vs. 71 Hz, respectively, Table A5.1), indicating a stronger interaction between phenol and Pd-BP. This may be a result of π-π interactions with the biphenylene linkers. Under reaction conditions, the fractions of phenol adsorbed on Pd-BP and Pd-T are (27 ± 3) % and (22 ± 3) %, respectively, also suggesting stronger interaction with Pd-BP. Thus, the increased cyclohexanone selectivity for the Pd-BP catalyst might be attributed to its increased phenol affinity, which prevents cyclohexanone from adsorbing onto the Pd active sites.

^{13}C NMR spectra recorded at the maximum cyclohexanone concentrations show that the chemical shifts for adsorbed cyclohexanone are different, and the peak area is larger for Pd-BP than Pd-T (ca. 21 and 12%, respectively, Fig. A5.8). Thus, the higher affinity of cyclohexanone for the Pd-BP surface is correlated with its increased rate of hydrogenation.

The effect of surface polarity was also studied by conducting the reaction catalyzed by Pd-T in water (Fig. A5.9). Due to the weaker interactions between the organics and Pd-T, compared to Pd-BP, peaks for adsorbed phenol and cyclohexanone are not clearly discernable. The kinetic profiles show a decreased rate of phenol conversion and lower cyclohexanone selectivity (Fig. 5.8b), compared with Pd-BP. The maximum cyclohexanone concentration, ca. 0.35 M, is lower (by 0.09 M). The lower cyclohexanone selectivity may be caused by relatively facile cyclohexanone adsorption onto the Pd active sites, due to the weaker interaction between phenol and the Pd-T surface. Thus, similar to the results in cyclohexane, the stronger interaction of phenol with Pd-BP than with Pd-T accelerates phenol conversion and inhibits the cyclohexanone adsorption, resulting in higher cyclohexanone selectivity.

5.5 Conclusion

This study shows how selecting the right combination of solvent and surface polarity improves activity/selectivity in the phenol hydrogenation reaction. In phenol hydrogenation, selectivity may be determined by the extent of cyclohexanone adsorption onto the Pd active sites, prior to cyclohexanone hydrogenation. Thus, increased cyclohexanone selectivity at full phenol conversion is achieved with a more hydrophobic catalyst, since adsorbed phenol effectively inhibits cyclohexanone adsorption onto the active sites of Pd-BP. Solvents with extreme polarities (including lack of polarity) such as cyclohexane and water confer much superior activity over solvents with intermediate polarity, such as methanol, acetonitrile, THF, and *p*-dioxane. The much higher activity observed in cyclohexane and water is attributed to their lower affinity for phenol, leading to increased adsorption. In contrast, phenol is better solvated by methanol and polar aprotic solvents, leading to negligible adsorption and much lower local phenol concentrations near the active sites. The low activity in these solvents is complicated by the apparent poisoning of the catalyst surface, which inhibits adsorption on the Pd sites specifically. The real cause merits further investigation.

This research suggests that solvent choice to promote phenol adsorption is critical, modulating molecular adsorption due to support hydrophobicity. The findings should be generalized to other types of reactions. An important future research direction is how lignin can be more effectively depolymerized by the choice of solvent and surface to promote its adsorption and unfolding.

5.6 References

(1) Yoshida, H.; Onodera, Y.; Fujita, S.; Kawamori, H.; Arai, M. Solvent Effects in Heterogeneous Selective Hydrogenation of Acetophenone: Differences between Rh/C and

Rh/Al_2O_3 Catalysts and the Superiority of Water as a Functional Solvent. *Green Chem.* **2015**, *17* (3), 1877–1883.

(2) Bertero, N. M.; Trasarti, A. F.; Apesteguía, C. R.; Marchi, A. J. Solvent Effect in the Liquid-Phase Hydrogenation of Acetophenone over Ni/SiO2: A Comprehensive Study of the Phenomenon. *Appl. Catal., A* **2011**, *394* (1–2), 228–238.

(3) McManus, I.; Daly, H.; Thompson, J. M.; Connor, E.; Hardacre, C.; Wilkinson, S. K.; Sedaie Bonab, N.; ten Dam, J.; Simmons, M. J. H.; Stitt, E. H.; D'Agostino, C.; McGregor, J.; Gladden, L. F.; Delgado, J. J. Effect of Solvent on the Hydrogenation of 4-Phenyl-2-Butanone over Pt Based Catalysts. *J. Catal.* **2015**, *330*, 344–353.

(4) Wan, H.; Vitter, A.; Chaudhari, R. V.; Subramaniam, B. Kinetic Investigations of Unusual Solvent Effects during Ru/C Catalyzed Hydrogenation of Model Oxygenates. *J. Catal.* **2014**, *309*, 174–184.

(5) Karimi, B.; Mirzaei, H. M.; Behzadnia, H.; Vali, H. Novel Ordered Mesoporous Carbon Based Sulfonic Acid as an Efficient Catalyst in the Selective Dehydration of Fructose into 5-HMF: The Role of Solvent and Surface Chemistry. *ACS Appl. Mater. Interfaces* **2015**, *7* (34), 19050–19059.

(6) Cubo, A.; Iglesias, J.; Morales, G.; Melero, J. A.; Moreno, J.; Sánchez-Vázquez, R. Dehydration of Sorbitol to Isosorbide in Melted Phase with Propyl-Sulfonic Functionalized SBA-15: Influence of Catalyst Hydrophobization. *Appl. Catal., A* **2017**, *531*, 151–160.

(7) Kobayashi, H.; Yokoyama, H.; Feng, B.; Fukuoka, A. Dehydration of Sorbitol to Isosorbide over H-Beta Zeolites with High Si/Al Ratios. *Green Chem.* **2015**, *17* (5), 2732–2735.

(8) Mai, J.; Fang, Y.; Liu, J.; Zhang, J.; Cai, X.; Zheng, Y. Simple Synthesis of WO3-Au Composite and Their Improved Photothermal Synergistic Catalytic Performance for Cyclohexane Oxidation. *Mol.* **2019**, *473*, 110389.

(9) Wang, Y.; Yao, J.; Li, H.; Su, D.; Antonietti, M. Highly Selective Hydrogenation of Phenol and Derivatives over a Pd@Carbon Nitride Catalyst in Aqueous Media. *J. Am. Chem. Soc.* **2011**, *133* (8), 2362–2365.

(10) Xia, H.; Tan, H.; Cui, H.; Song, F.; Zhang, Y.; Zhao, R.; Chen, Z.-N.; Yi, W.; Li, Z. Tunable Selectivity of Phenol Hydrogenation to Cyclohexane or Cyclohexanol by a Solvent-Driven Effect over a Bifunctional Pd/NaY Catalyst. *Catal. Sci. Technol.* **2021**, *11* (5), 1881–1887.

(11) Li, X.; Cheng, L.; Wang, X. Selective Phenol Hydrogenation under Mild Condition over Pd Catalysts Supported on Al2O3 and SiO2. *Res. Chem. Intermed.* **2019**, *45* (3), 1249–1262.

(12) Reichardt, C.; Welton, T. *Solvents and Solvent Effects in Organic Chemistry*, 4th edn.; Wiley-VCH: Weinheim, 2011.

(13) Castola, V.; Mazzoni, V.; Corticchiato, M.; Bighelli, A.; Casanova, J. Hydrogen Bonding Effect on Carbon-13 NMR Chemical Shifts of Naturally Occurring Phenols. *Can. J. Anal. Sci. Spectrosc.* **1997**, *42*, 90–94.

(14) Jeng, M.-L. H.; Li, Y.-S. Hydrogen Bonding Interactions of Phenol with Cyclic Ketones. *Spectrochim. Acta A Mol. Biomol. Spectrosc*. **1989**, *45* (5), 525–531.

(15) Hiraga, Y.; Chaki, S.; Niwayama, S. 13C NMR Spectroscopic Studies of the Behaviors of Carbonyl Compounds in Various Solutions. *Tetrahedron Lett.* **2017**, *58* (50), 4677–4681.

(16) Faska, N.; Auhmani, A.; Esseffar, M. Solvent Effects on 13C and 1H NMR Shielding of Cyclic Ketones: An Experimental and Theoretical Study. *J. Mol. Struct-Thermochem* **2007**, *811* (1–3), 203–213.

(17) Kashid, S. M.; Bagchi, S. Experimental Determination of the Electrostatic Nature of Carbonyl Hydrogen-Bonding Interactions Using IR-NMR Correlations. *J. Phys. Chem. Lett.* **2014**, *5* (18), 3211–3215.

(18) Nakashima, T. T.; Traficante, D. D.; Maciel, G. E. Carbon-13 Chemical Shifts on the Carbonyl Carbon. VII. Phenol-Acetone System. *J. Phys. Chem.* **1974**, *78* (2), 124–129.

(19) Liu, Z.; Hamad, I. A.; Li, Y.; Chen, Y.; Wang, S.; Jentoft, R. E.; Jentoft, F. C. Poisoning and Competitive Adsorption Effects during Phenol Hydrogenation on Platinum in Water-Alcohol Mixtures. *Appl. Catal., A* **2019**, *585*, 117199.

(20) Adamczyk, A. J. First-Principles Analysis of Acetonitrile Reaction Pathways to Primary, Secondary, and Tertiary Amines on Pd(111). *Surf. Sci.* **2019**, *682*, 84–98.

5.7 Appendix IV

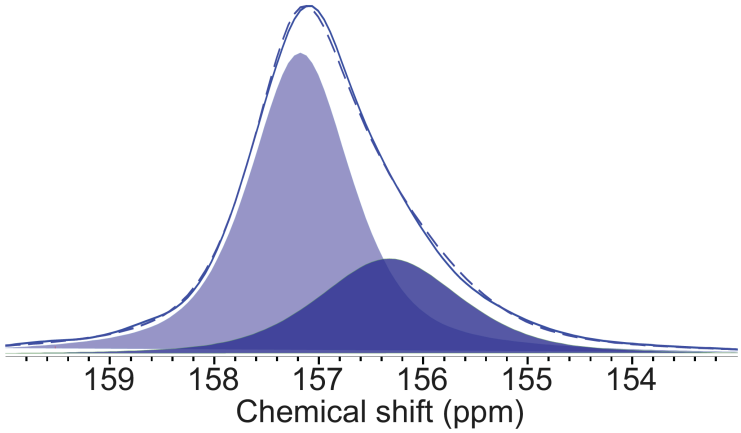

Fig. A5.1. Deconvolution of phenol peak obtained during the phenol hydrogenation over Pd-BP in cyclohexane.

Table A5.1. Peak line widths (FWHM) for solution-phase and adsorbed phenol in the presence of Pd-BP and Pd-T, obtained by deconvolution of NMR spectra

Time (min)	Pd-BP		Pd-T	
	Adsorbed (Hz)	Solution (Hz)	Adsorbed (Hz)	Solution (Hz)
4	107.1	67.6	74.4	69.9
8	105.0	68.4	75.5	67.5
14	90.6	65.1	67.5	63.7
18	93.2	58.8	67.1	62.2
22	106.9	59.8	71.3	63.5
26	115.3	57.5	69.6	60.5
30	-	-	71.7	57.0
34	-	-	69.7	63.0

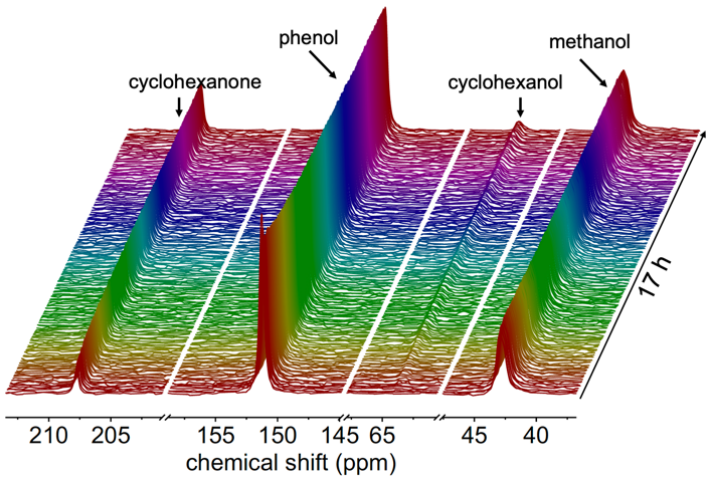

Fig. A5.2. *Operando* MAS ^{13}C NMR array obtained during phenol hydrogenation over the Pd-BP catalysts at 90 °C in methanol.

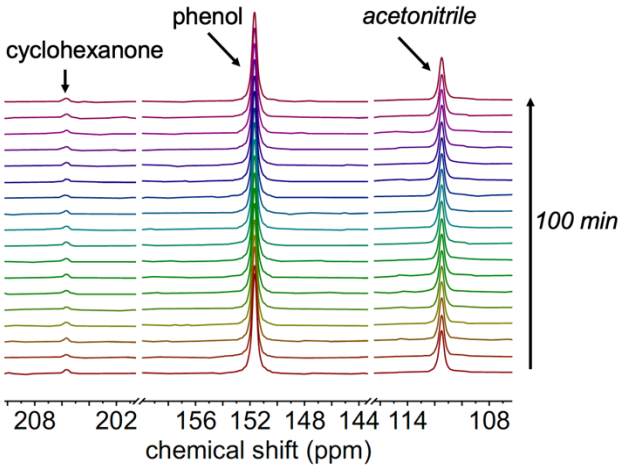

Fig. A5.3. *Operando* MAS ^{13}C NMR array obtained during phenol hydrogenation over the Pd-BP catalysts at 90 °C in acetonitrile recorded for 100 min.

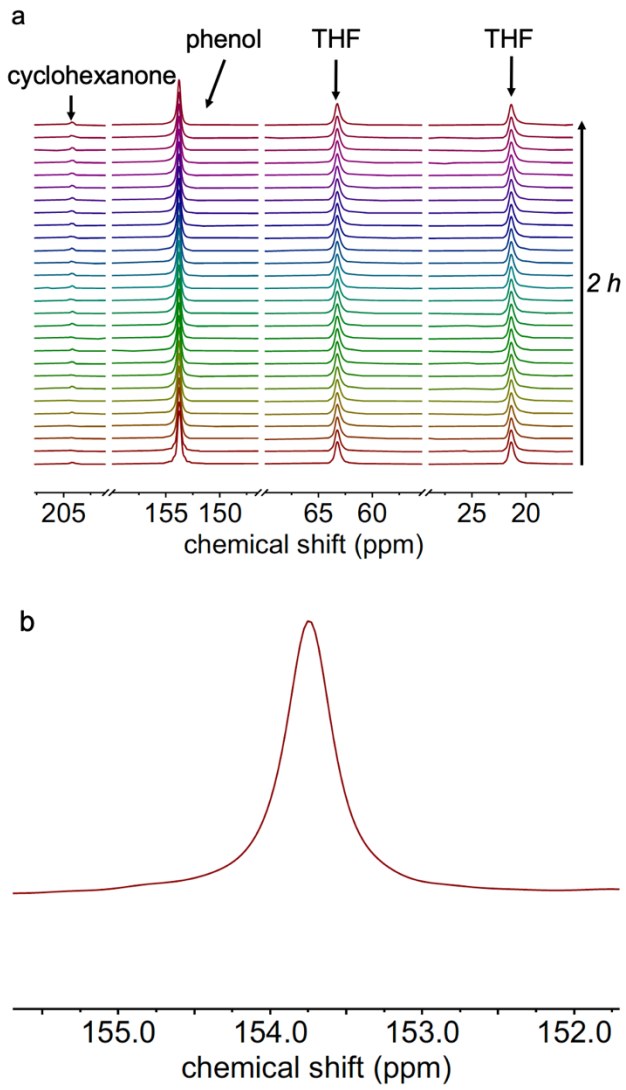

Fig. A5.4. (a) *Operando* MAS ^{13}C NMR array obtained during phenol hydrogenation over the Pd-BP catalysts at 90 °C in THF recorded for 2 h. (b) NMR spectrum representing phenol peak when THF and Pd-BP were used as a solvent and catalyst at 90 °C.

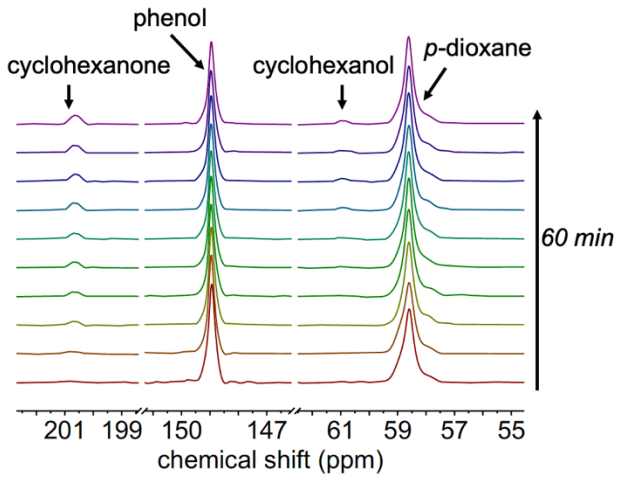

Fig. A5.5. *Operando* MAS ^{13}C NMR array obtained during phenol hydrogenation over the Pd-BP catalysts at 90 °C in *p*-dioxane recorded for 70 min.

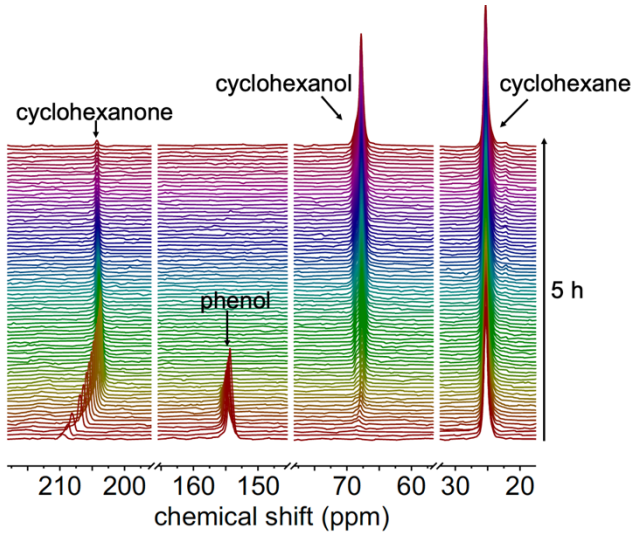

Fig. A5.6. (a) *Operando* MAS ^{13}C NMR array obtained during phenol hydrogenation over the Pd-T catalysts at 90 °C in cyclohexanane recorded for 5 h.

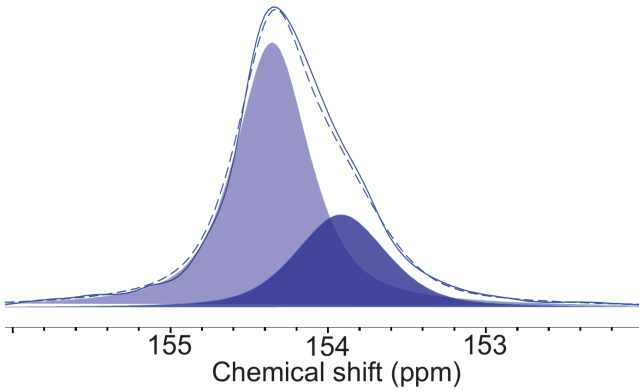

Fig. A5.7. Deconvolution of phenol peak obtained during the phenol hydrogenation over Pd-T in cyclohexane.

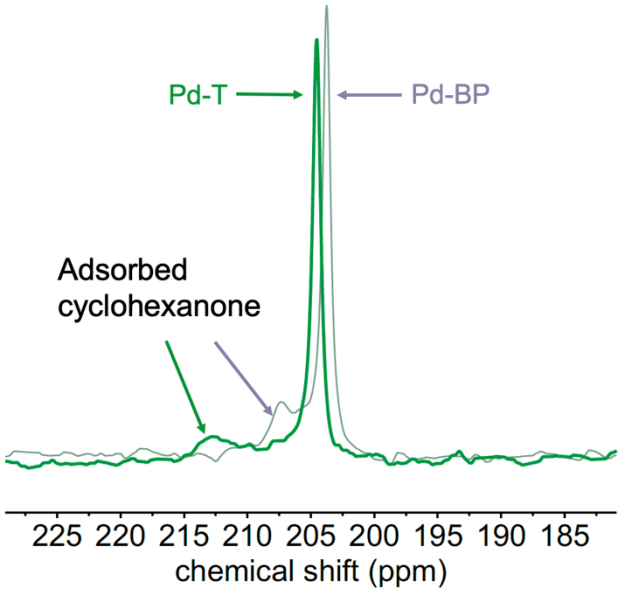

Fig. A5.8. Comparison of ^{13}C NMR spectra in the cyclohexanone region, recorded when the cyclohexanone concentration was a maximum during phenol hydrogenation catalyzed by Pd-BP or Pd-T.

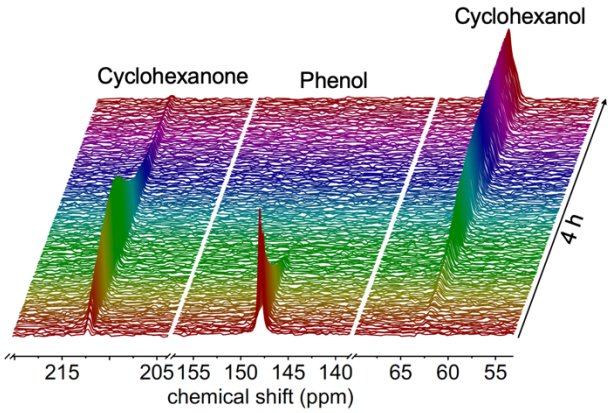

Fig. A5.9. (a) *Operando* MAS ^{13}C NMR array obtained during phenol hydrogenation over the Pd-T catalysts at 90 °C in water recorded for 4 h.

Chapter 6. Conclusion

In order to investigate the effect of surface and solvent polarity on molecular adsorption and heterogeneous catalysis, mesoporous organosilicas with a wide range of surface polarities were synthesized via a co-condensation method using organosilica precursors. Fluorescence of Prodan dye adsorbed on the mesoporous materials demonstrated that the most hydrophilic material has a polarity comparable to methanol, while the most hydrophobic surface was similar in polarity to DMSO. The varying surface polarity of each mesoporous organosilica was further explored via the mobility of tethered 4-carboxy TEMPO radicals. Molecular adsorption on each organosilica from various solvents including water, DMSO, and benzene suggests that the extent of adsorption can be precisely tuned by varying surface as well as solvent polarity.

The measurement of translational surface water diffusivity for these organosilicas showed a decreasing trend with increasing surface hydrophobicity. By contrast, increasing surface water diffusivity was observed for more hydrophobic surface consisting of siloxane groups. The results suggest that the relative importance of thermodynamic terms governing interfacial hydration can change depending on the surface chemical composition. In particular, decreased surface water dynamics on the organosilica surface originate from the decreased entropy of surface water molecules that form a more ordered structure. These low-entropy spots could provide a way to enhance the extent of molecular adsorption in heterogeneous catalysis.

Phenol hydrogenation over Pd catalysts in water showed increased activity and higher selectivity to the intermediate, cyclohexanone, for the more hydrophobic catalyst. ^{13}C MAS

NMR spectra recorded in *operando* mode indicate enhanced phenol-catalyst surface interactions for the hydrophobic catalyst, resulting in increased local phenol concentration around Pd active sites. In addition, the hydrogen bonding interaction between phenol and cyclohexanone further promotes the cooperative adsorption of phenol, which might lead to the increased cyclohexanone selectivity. Successful simulation of the kinetic profiles requires consideration of the interaction of each species with the Pd, as well as with the support.

The type of solvent used in phenol hydrogenation is also an important factor in determining the activity of the Pd catalyst. Using water and cyclohaxane resulted in significantly higher conversion compared with other organic solvents such as acetonitrile, THF, and *p*-dioxane. The main cause for the lower activity in the latter group of solvents is the higher degree of phenol solvation, which hinders the adsorption of phenol onto the catalyst surface.

In terms of improving selectivity for the intermediate in A→B→C reactions, it is necessary to design the surface hydrophobicity and chemistry by considering the hydrophobicity of the reactant as well as the intermediate. Activity and selectivity are governed by kinetic parameters, i.e., rate and adsorption constants. Thus, studying the effect of experimental parameters influencing kinetics, such as temperature, catalyst concentration, and H_2 pressure, will be helpful in identifying strategies to control activity and selectivity in hydrogenation.

In this research, phenol was used as a reactant to assess the surface and solvent polarity effect in heterogeneous catalysis. To direct the research toward a more practical applications, lignin oligomers, organosolv lignin, or lignin itself should be studied as reactants in future research. Since lignin is typically water-insoluble solvents or co-solvents that promote both

dissolution and adsorption onto the catalyst surface are needed. In addition, the effect of catalyst surface hydrophobicity and aromaticity on the unfolding of lignin polymer will be important in assessing the effectiveness of surface chemistry modifications.